STRUCTURAL, PHYSICAL, ELECTRONIC PROPERTIES STUDIES ON KAGOME LATTICE SYSTEMS

Thesis submitted for the degree of

DOCTOR OF PHILOSOPHY (SCIENCE)
in
PHYSICS (EXPERIMENTAL)

by

Achintya Low
DEPARTMENT OF PHYSICS
UNIVERSITY OF CALCUTTA
2024

Dedicated to my beloved Mother

ACKNOWLEDGMENTS

I am honored to have had the opportunity to join and successfully complete my integrated Ph.D. journey at the S. N. Bose National Centre for Basic Sciences. The outstanding education and research facilities have significantly enhanced my academic and personal experience. Throughout my academic journey, I've had the privilege of learning from numerous individuals who have instilled in me the importance of education and fueled my enthusiasm for research. At this point, I express my sincere gratitude to all of them.

It brings me immense pleasure to extend my sincere respect and profound gratitude to Dr. Thirupathaiah Setti, my Ph.D. supervisor in the Department of Condensed Matter and Materials Physics, S. N. Bose National Centre for Basic Sciences, Kolkata-700106. His wisdom, vision, expertise, and unwavering guidance have been indispensable throughout the planning and development stages of this research endeavor. I am profoundly grateful for his enthusiastic involvement and persistent encouragement, which have been pivotal in the completion of this work. I am also deeply appreciative of his meticulous efforts in meticulously reviewing and enhancing the manuscripts, without which this endeavor would not have been possible. I am also indebted to him for his unwavering support during my personal triumphs.

I am deeply grateful to the S. N. Bose National Centre for Basic Sciences for enhancing my research environment. The exceptional research facilities, tranquil surroundings, and comfortable accommodations have nurtured my academic endeavors. Special thanks go to the Technical Research Centre (TRC) for their invaluable support, as this research extensively utilized the Instrument facilities at the TRC of S. N. Bose National Centre for Basic Sciences, established under the TRC project of the Department of Science and Technology (DST), Government of India. Additionally, I extend my heartfelt appreciation to S. N. Bose National Centre for Basic Sciences for providing the fellowship that sustained my research journey.

I would like to express my sincere appreciation to the entire Quantum-Materials group. My heartfelt gratitude goes out to Indrani Kar, Susmita Changdar, Sayan Routh, Shubham Purwar, Susanta Ghosh, and Soumya Ghorai, whose friendship and collaborative efforts have been fundamental to my research journey. I am particularly grateful to my junior, Susanta Ghosh. I am also indebted to the postdoctoral scholars in our group, Dr. Tushar Kanti Bhowmik, Dr. Reena Goyal, Dr. Pankaj Maheshwari, Dr. Tusita Sau and Dr. Ayana

Mukhopadhyay, whose invaluable insights have guided me through numerous research challenges.

My sincere thanks to my M.Sc. supervisor Prof. Subhrangshu Sekhar Manna and all the teachers.

I express my gratitude to the esteemed members of the examination committee for generously dedicating their time and effort to evaluate my thesis.

I would like to express my thanks to my I.Ph.D. friends, Ankur Srivastav, Anuj Kumar Dhiman, Sayan Routh, Megha Dave, Anwesha Chakrabarty, Neeraj Kumar, Raghveender. I am delighted to have Ankur as a friend for his continual encouragement and support.

Special thanks are extended to the technical staff, including Mr. Rishikesh Nandi, Mr. Shakti Nath Das, Mrs. Urmi Chakrabarty, Mr. Joy Bandopadhyay, Mr. Sourabh Sinha, and Mr. Debarghya Ghosh, for their unwavering technical support during the measurements conducted at S.N. Bose National Centre for Basic Sciences, Kolkata.

Words alone cannot adequately express my gratitude towards my mother Chandrani Low. I feel the luckiest person in the universe to be her son. Her love, unwavering support, and belief in me have shaped me into the person I am today. I am also grateful to my father Akshoy Kumar Low for his wisdom and encouragement. I am indebted to my uncle, Tapan Kumar Das, for his constant support, love, and faith in me.

I am thankful to my school teacher, Gurudas Mukherjee, for his encouragement throughout this wonderful journey.

Finally, my special thanks to my beautiful wife Sayani Pal. Her love and constant support make me stronger everyday.

(Achintya Low)

ABSTRACT

The discovery of quantum topology in condensed matter systems created new paths in the fundamental sciences and potential technological applications. In this regard, the Kagome systems have attracted much research interest due to their ability to host several exotic quantum phases such as Weyl and Dirac fermions, flat bands, Skyrmion lattice, anomalous and topological Hall effects, and frustrated magnetism. The Kagome lattice has a unique structure with hexagons and triangles, leading to geometrical frustration. This Ph.D. thesis aims to design, synthesize, and characterize various Kagome lattice systems in their single crystalline phase. Importantly, this thesis discusses various exotic quantum phases of the fascinating Kagome systems.

We have grown high-quality single crystals of various Kagome systems and studied their structural properties systematically to know the phase purity of the as-grown single crystals. Having established the crystal structure, we studied the physical properties like the electrical and magneto-transport properties, magnetic properties, and electronic band structure. For instance, Mn_3Sn, a non-collinear antiferromagnet hosting Weyl fermions, shows a large intrinsic out-of-plane anomalous Hall effect (AHE). In this study, for the first time, in addition to the out-of-plane AHE, we also uncover a large in-plane topological Hall effect (THE) in Mn3Sn at room temperature, which is gradually suppressed by Fe doping at the Mn site of $Mn_{3-x}Fe_xSn$. With the doping of Fe atoms, we see a significant change in the magnetic and electrical transport properties of pristine Mn_3Sn. The easy magnetization axis shifts from the crystallographic ab-plane to the c-axis with Fe doping. The Fe doping generates huge coercivity in the low-temperature region, converting the AFM system into a low-temperature ferromagnet. Further, the observation of significant THE at a low temperature induced by Fe doping suggests the presence of a Skyrmion lattice. Upon completely replacing the Mn with Fe, i.e., Fe_3Sn is an in-plane ferromagnet with very high magneto-crystalline anisotropy (1.02×10^6 J/m^3). Unlike in Mn_3Sn, in which AHE is of the intrinsic type, the anomalous Hall signal in Fe3Sn has intrinsic and extrinsic Hall contributions. The intrinsic Hall contribution arises from the k-space Berry curvature. The extrinsic Hall contribution comes from the skew-scattering, which decays quadratically with increasing temperature due to electron-phonon scatterings. We have also studied the rare-earth-based Kagome magnet $HoMn_6Ge_6$. Temperature-dependent electrical resistivity demonstrates various magnetic-transition-driven anomalies. A crossover from negative to positive magnetoresistance (MR) is observed. While the linear nonsaturating positive MR exists in the low-temperature region are mainly driven by the linear Dirac-like band dispersions as predicted by the first-principles calculations, the negative MR observed in the high-temperature region is due to the spin-flop type magnetic transition. Consistent with anisotropic Fermi surface topology as observed from the density functional theory calculations, we find anisotropic magnetoresistance at low temperatures. A significant anomalous Hall effect has been noticed at high temperatures in addition to a switching of the dominant charge carrier from electron to hole at around 220K.

রূপরেখা

ঘনীভূত পদার্থ সিস্টেমে, কোয়ান্টাম টপোলজির আবিষ্কার মৌলিক বিজ্ঞান এবং সম্ভাব্য প্রযুক্তিগত অ্যাপ্লিকেশনগুলিতে নতুন পথ তৈরি করেছে। এই বিষয়ে, কাগোম গঠনগুলি বেশ কিছু রোমাঁচকর কোয়ান্টাম পর্যায় যেমন ওয়েইল এবং ডিরাক ফার্মিয়ন, ফ্ল্যাট ব্যান্ড, স্কাইরমিয়ন জালি, অস্বাভাবিক এবং টপোলজিকাল হল ইফেক্ট এবং হতাশ চুম্বকত্ব অঙ্গীকার করার ক্ষমতার কারণে গবেষণার আগ্রহকে আকর্ষণ করেছে। কাগোম জালিতে ষড়ভুজ এবং ত্রিভুজ সহ একটি অনন্য কাঠামো রয়েছে, যা জ্যামিতিক হতাশার দিকে পরিচালিত করে। এই পিএইচ.ডি. থিসিসের লক্ষ্য তাদের একক স্ফটিক পর্যায়ে বিভিন্ন কাগোম জালি সিস্টেমের নকশা, সংশ্লেষণ এবং বৈশিষ্ট্য পর্যবেক্ষণ এবং আলোচনা করা। গুরুত্বপূর্ণভাবে, এই থিসিসটি কাগোম সিস্টেমের বিভিন্ন রোমাঁচকর কোয়ান্টাম পর্যায়গুলি নিয়ে আলোচনা করে।

আমরা বিভিন্ন কাগোম সিস্টেমের উচ্চ-মানের একক ক্রিস্টাল তৈরি করেছি এবং তাদের গঠনগত বৈশিষ্ট্যগুলিকে পদ্ধতিগতভাবে অধ্যয়ন করেছি যাতে বেড়ে ওঠা একক ক্রিস্টালগুলির গঠন বিশুদ্ধতা জানা যায়। ক্রিস্টাল কাঠামো প্রতিষ্ঠা করার পরে, আমরা বৈদ্যুতিক এবং চুম্বক-পরিবহন বৈশিষ্ট্য, চৌম্বকীয় বৈশিষ্ট্য এবং ইলেকট্রনিক ব্যান্ড কাঠামোর মতো ভৌত বৈশিষ্ট্যগুলি অধ্যয়ন করেছি। উদাহরণস্বরূপ, Mn_3Sn, একটি নন-কোলিনিয়ার অ্যান্টিফেরোম্যাগনেট সহ ওয়েইল ফার্মিয়ন, একটি বৃহৎ অভ্যন্তরীণ আউট-অফ-প্লেন অ্যানোমালাস হল প্রভাব(Anomalous Hall Effect) দেখায়। এই গবেষণায়, প্রথমবারের মতো, প্লেনের বাইরের AHE ছাড়াও, আমরা ঘরের তাপমাত্রায় Mn_3Sn-এ একটি বৃহৎ ইন-প্লেন টপোলজিকাল হল ইফেক্ট (Topological Hall Effect) উন্মোচন করেছি, যা ধীরে ধীরে Mn -এ Fe ডোপিং দ্বারা দমন করা হয়। $Mn_{3-x}Fe_xSn$ এর সাইট। Fe পরমাণুর ডোপিংয়ের সাথে, আমরা আদি Mn_3Sn এর চৌম্বকীয় এবং বৈদ্যুতিক পরিবহন বৈশিষ্ট্যে একটি উল্লেখযোগ্য পরিবর্তন দেখতে পাই। সহজ চৌম্বকীয়করণ অক্ষ-কে ডোপিং দ্বারা ক্রিস্টালোগ্রাফিক ab- তল থেকে c- অক্ষে স্থানান্তরিত হয়। Fe ডোপিং নিম্ন-তাপমাত্রা অঞ্চলে বিশাল প্রভাব তৈরি করে,অ্যান্টিফেরোম্যাগনেট সিস্টেমকে একটি নিম্ন-তাপমাত্রার ফেরোম্যাগনেটে রূপান্তরিত করে। আরও, লৌহ ডোপিং দ্বারা প্ররোচিত নিম্ন তাপমাত্রায় উল্লেখযোগ্য THE এর পর্যবেক্ষণ একটি স্কাইরমিয়ন জালির উপস্থিতি নির্দেশ করে। Mn কে সম্পূর্ণভাবে Fe দিয়ে প্রতিস্থাপন করার পর, অর্থাৎ, Fe_3Sn হল একটি অভ্যন্তরীণ ফেরোম্যাগনেট যার খুব উচ্চ চুম্বক-ক্রিস্টালাইন অ্যানিসোট্রপি (1.02×10^6 J/m^3) । Mn_3Sn এর বিপরীতে, যেখানে AHE অভ্যন্তরীণ প্রকারের, Fe_3Sn- এ অস্বাভাবিক হল সংকেতের অন্তর্নিহিত এবং বহির্মুখী হল অবদান রয়েছে। অন্তর্নিহিত হল অবদান কে-স্পেস বেরি বক্রতা থেকে উদ্ভূত হয়। বহির্মুখী হলের অবদান স্কু-স্ক্যাটারিং থেকে আসে, যা ইলেকট্রন-ফোনন বিচ্ছুরণের কারণে ক্রমবর্ধমান তাপমাত্রার সাথে দ্বিঘাতভাবে ক্ষয়প্রাপ্ত হয়। আমরা বিরল-পৃথিবী-ভিত্তিক কাগোম চুম্বক $HoMn_6Ge_6$ ও অধ্যয়ন করেছি। তাপমাত্রা-নির্ভর বৈদ্যুতিক প্রতিরোধ ক্ষমতা বিভিন্ন চৌম্বক-পরিবর্তন-চালিত অস্বাভাবিকতা প্রদর্শন করে। নেতিবাচক থেকে পজিটিভ ম্যাগনেটোরেসিস্ট্যান্স পর্যন্ত একটি সমন্বয় পরিলক্ষিত হয়। যদিও নিম্ন-তাপমাত্রা অঞ্চলে রৈখিক অসংপৃক্ত পজিটিভ ম্যাগনেটোরেসি-

স্ট্যান্স বিদ্যমান থাকে, প্রধানত রৈখিক ডিরাক-সদৃশ ব্যান্ড বিচ্ছুরণ দ্বারা চালিত হয় যেমন ঘনত্ব ফাংশনাল গণনার দ্বারা পূর্বাভাস দেওয়া হয়, উচ্চ-তাপমাত্রা অঞ্চলে পরিলক্ষিত নেতিবাচক ম্যাগনেটোরেসিস্ট্যান্স স্পিন-ফ্লপ চৌম্বকীয় রূপান্তর কারণে হয়। অ্যানিসোট্রপিক ফার্মি সারফেস টপোলজির সাথে সামঞ্জস্যপূর্ণ, যেমন ঘনত্ব কার্যকরী তত্ত্ব গণনা থেকে পর্যবেক্ষণ করা হয়েছে, আমরা কম তাপমাত্রায় অ্যানিসোট্রপিক চুম্বক প্রতিরোধক খুঁজে পাই। প্রায় 220 K এ ইলেক্ট্রন থেকে গর্তে প্রভাবশালী চার্জ সংবাহক পরিবর্তনের পাশাপাশি উচ্চ তাপমাত্রায় একটি উল্লেখযোগ্য অস্বাভাবিক হল প্রভাব লক্ষ্য করা গেছে।

Contents

Chapter 1

Introduction

Symmetry, a natural phenomenon governing the fundamental principles of physics explained by the phenomenological Ginzburg-Landau theory [1, 2]. Until the 1980s, this theory successfully elucidated various phases transitions in condensed matter by studying the local ordering parameters. Phase transitions were defined through the minimization of Landau free energy under external changes like temperature, pressure, and magnetic field. However, the discovery of integer quantum Hall effect (IQHE) in 1980 [3] and fractional quantum Hall effect (FQHE) in 1982 [4] first illuminated the experimental realizations of the quantum phases without breaking any local symmetry. In Quantum Hall Effect (QHE) experiment, a 2D electron gas system exhibit quantized plateaus in Hall conductance and protected conducting edge states called as topological phases. These topological phases are based on the breaking time-reversal symmetry (TRS), long-range order, or global symmetry of matter [2]. The global symmetry of matter is constructed through the introduction of quantum superposition or long-range entanglement of interacting particles [1, 2]. The evolution of various topological phases, such as 2D topological insulator (2005) [5], 3D topological insulator (2007) [6, 7], Dirac semimetal (2014) [8, 9], and Weyl semimetal (2015) [10, 11], showcased the versatility of this research interests. These phases could originate either extrinsically through the disorder-mediated scattering or intrinsically via the spin-dependent band structure of matter.

Distinct topological invariants manifest different topological phases. Quantum Hall or Chern insulator phases defined by the Thouless-Kohmoto-Nightingale-Njis (TKNN) number or Chern number [12, 13]. In contrast, topological insulator and semimetal phases are represented by the topological invariant Z_2 index, calculated from the Berry curvature in the momentum space [12, 13].

Topological quantum computation, in which the data encoding has to be error-free, requires an appropriate topological material. So far, many systems have been proposed theoretically and experimentally for the topological quantum computation [14]. To understand the effectiveness and applicability of these systems for quantum computation, we need to understand their topological properties of these compounds microscopically. Among several proposed topological systems, we think, kagome lattice systems are promising considerations due to their unique electronic and magnetic structure [15]. Therefore, this thesis aims is to grow single crystals of various kagome systems and study their structural, electronic, magnetic, and transport properties.

The first chapter of this thesis discusses the concept of topological invariance from abstract mathematical perspective and its connection to condensed matter systems via Berry phase. Then, we discuss the role of spin-orbit coupling in the topological phases. Next, I move towards a brief discussion about different types of Hall effect and their connection to the topological properties, such as quantum Hall effect, quantum spin Hall effect, anomalous Hall effect, and topological Hall effect. Next, I discuss the role of symmetries in topological systems and the properties of topological semimetals. Finally, I end this chapter by discussing the properties of Kagome lattice systems.

In the second chapter, I delve into the experimental techniques. I begin by discussing the different methods employed for single crystal growth. Subsequently, I focus on crystal characterization methods, including X-ray diffraction (XRD) and energy dispersive X-ray analysis (EDXS). The magnetic properties of the single crystals were analyzed using a vibrating sample magnetometer (VSM). Additionally, electrical and magneto-transport studies were conducted using the physical property measurement system (PPMS) from Quantum Design, specifically the [DynaCool model] with magnetic field strength of upto 9 Tesla.

From chapters three to six, I present the results on different Kagome samples that I have grown during my Ph.D. tenures. In the chapter three, I present the work done on $\mathrm{Mn_3Sn}$. I observe a significant in-plane pure topological Hall effect which was diminished by doping with Fe atoms. In chapter the four, I worked on the effect of Fe atoms doping in $\mathrm{Mn}_{3-x}\mathrm{Fe}_x\mathrm{Sn}$ at the Mn site, as this system shows strong correlation between the electronic and magnetic structures, allowing us to tune the magnetism and its topological properties. Chapter five talks about the growth of $\mathrm{Fe_3Sn}$ single crystal as there are a few reports on the single crystals of this system. $\mathrm{Fe_3Sn}$ shows a giant anomalous Nernst effect due a the non-trivial Berry phase in the k-space. Here, we have studied its magnetic and Hall properties in detail. In the chapter six, I present the single crystal growth of $\mathrm{HoMn_6Ge_6}$. Although $\mathrm{HoMn_6Sn_6}$ and $\mathrm{HoMn_6Ge_6}$ shares similar structure, not many studies available in $\mathrm{HoMn_6Ge_6}$ discussing its topological properties. Here, we studied its structural, magnetic, magneto-transport, and electronic band structure. Finally, chapter seven leads to the conclusions of this thesis.

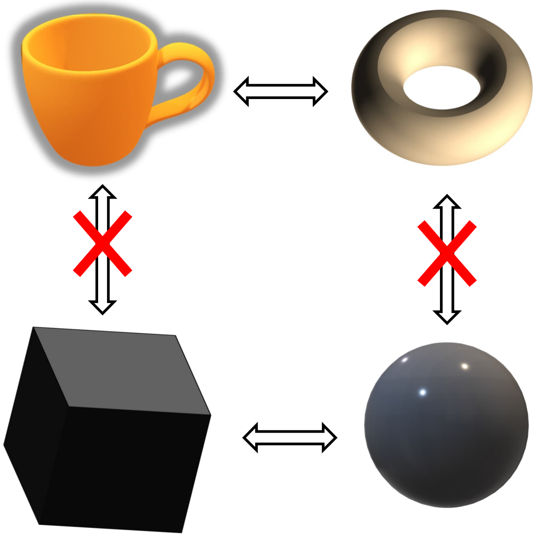

Figure 1.1: Concept of topological invariance: A coffee mug can be transformed to a doughnut and a sphere can be transformed to a cube. But a doughnut can not be transformed to a sphere. Therefore from topology both doughnut & coffee mug and cube & sphere are the same.

1.1 Topological Invariance

The term 'Topology' is derived from the realm of abstract mathematics. By introducing topology, a mathematical geometry can be unaltered continuously from one shape to another without breaking it [16]. This concept can be easily visualized by the following example. If we consider a coffee cup made of stretchable material, by applying external force, we can shape it into a doughnut, as shown in Fig.1.1. In short to a topologist, a coffee mug and a doughnut are indistinguishable. In mathematical term, this equivalence or one-to-one correspondence in topological space is called homeomorphism. In simple mathematical definition, if A and B are two topological spaces and they are homeomorphic then there is a continuous map $f : A \to B$ and $g : B \to A$ such that $f \circ g : A \to A$ and $g \circ f : B \to B$. The maps f and g are homeomorphisms, and we can write $f^{-1} \equiv g$ and $g^{-1} \equiv f$. Topological invariant properties are always preserved under homeomorphism. In the example shown in Fig.1.1, the hole in the coffee mug and the doughnut is topologically invariant.

1.2 Berry Curvature

In 1983, 'Berry' realized that if a quantum mechanical system is transported in a closed path (C) in a parameter space [17], it would acquire a phase which depends on the geometry of the path called 'Berry phase'. We can understand the concept of Berry phase using a simple

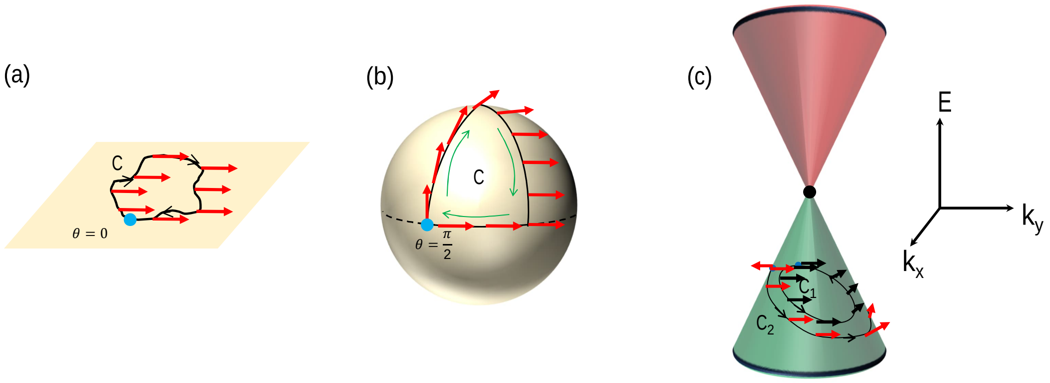

Figure 1.2: visualization of Berry curvature. (a) parallel transport in a 2D sheet where the geometrical phase for the closed loop is 0 while in (b) a sphere the geometrical phase is $\frac{\pi}{2}$ for the closed loop 'C'. (c) Visualization of Berry phase in momentum space. The images are reproduced from [19]

geometrical parallel transport mechanism [18]. For example, consider a tangent vector of a surface in real space is to be transported in a closed path 'C' such that the tangent vector does not rotate around the normal to the surface at any point. As seen in Fig.1.2(a), the tangent vector is to be transported in a 2D Euclidean surface along the path 'C'. We can see that there is no change in the angle between the initial and final tangent vector. On the other hand, if we take a spherical surface and transport a tangent vector, as shown in the Fig.1.2(b), there will be $\frac{\pi}{2}$ phase difference between initial and final tangent vector when transported in the closed path 'C'.

Consider a Hamiltonian $\hat{\mathcal{H}}(\mathbf{R})$ acting on a quantum system where $\mathbf{R}(\vec{R}_1, \vec{R}_2, \vec{R}_3...., \vec{R}_n)$ is a collection of vectors in a parameter space. For each $\mathbf{R}$, there are n eigenstates $|n(\mathbf{R})\rangle$ and corresponding eigenvalues $E_n(\mathbf{R})$ as discussed in [20, 21]

$$\hat{\mathcal{H}}(\mathbf{R})|\psi_n(\mathbf{R})\rangle = E_n(\mathbf{R})|\psi_n(\mathbf{R})\rangle \tag{1.2.1}$$

We introduce an adiabatic closed path $\mathcal{C} \equiv \{\mathbf{R}(t) \mid t = 0 \rightarrow T\}$ in the parameter space. According to adiabatic theorem, the initial eigenstate is not changed over time if the rate of the variation of external parameter is very slow. We can write the state at time 't' as

$$|\Psi(t)\rangle = e^{-\frac{i}{\hbar}\int_0^t dt' E_n(\mathbf{R}(t'))}\,|\Phi_n(t)\rangle \tag{1.2.2}$$

where $|\Phi_n(t)\rangle$ (at $t = 0$) is an auxiliary wavefunction whose dynamical phase is zero. We can write

$$
\begin{aligned}
\langle\Psi(t)|\hat{\mathcal{H}}(t)|\Psi(t)\rangle &= \langle\Psi(t)|i\hbar\frac{\partial}{\partial t}|\Psi(t)\rangle \\
&= \langle\Phi_n(t)|e^{\frac{i}{\hbar}\int_0^t dt' E_n(\mathbf{R}(t'))}(i\hbar\frac{\partial}{\partial t})e^{-\frac{i}{\hbar}\int_0^t dt' E_n(\mathbf{R}(t'))}|\Phi_n(t)\rangle \\
&= E_n + i\left\langle\Phi_n(t)\middle|\dot{\Phi}_n(t)\right\rangle
\end{aligned}
\tag{1.2.3}
$$

As E_n is an eigenstate of $|\Psi(t)\rangle$ the equation takes the form

$$
i\left\langle\Phi_n(t)\middle|\dot{\Phi}_n(t)\right\rangle = 0 \tag{1.2.4}
$$

If we represent $|\Phi_n(t)\rangle$ in-terms of fixed eigenstate $|n(\mathbf{R}(t))\rangle$ we can write

$$
|\Phi_n(t)\rangle = e^{i\alpha_n(t)}\,|n(\mathbf{R}(t))\rangle \tag{1.2.5}
$$

By putting this relation in equation 1.2.4, we get

$$
\dot{\alpha}_n(t) = i\,\langle n(\mathbf{R}(t))|\dot{n}(\mathbf{R}(t))\rangle \tag{1.2.6}
$$

For the closed loop $\mathcal{C}$ the Berry phase is defined as follows

$$
\begin{aligned}
\dot{\alpha}_n(C) &= i\oint_{\mathcal{C}}\langle n(\mathbf{R}(t))|\,\partial_{\mathbf{R}}\,|n(\mathbf{R}(t))\rangle\,.d\mathbf{R} \\
&= i\oint_{\mathcal{C}}\mathbf{A}(\mathbf{R}).d\mathbf{R}
\end{aligned}
\tag{1.2.7}
$$

Here $\mathbf{A}(\mathbf{R})$ is called the Berry connection. Following Stokes theorem, we can rewrite the Eqn. 1.2.7 as

$$
\dot{\alpha}_n(C) = i\int_{\mathcal{S}}(\boldsymbol{\nabla}_{\mathbf{R}}\times\mathbf{A}(\mathbf{R}))d\mathbf{S} = i\int_{\mathcal{S}}\boldsymbol{\Omega}(\mathbf{R})d\mathbf{S} \tag{1.2.8}
$$

Here, $\boldsymbol{\Omega}(\mathbf{R}) = \boldsymbol{\nabla}_{\mathbf{R}}\times\mathbf{A}(\mathbf{R})$ is called the Berry phase.

In condensed matter, there are mainly two parameter spaces, which physicists use (i) Berry phase in the crystal momentum space (**k**) and (ii) Berry phase in the real space (**r**). If we compare this Berry concept with classical electromagnetism, Berry curvature represents a pseudo magnetic field, and the Berry phase is the magnetic flux. Berry phase in momentum space is mainly generated by nontrivial band topology in the electronic band structure, while in real space, it is mainly generated by nontrivial magnetic structure. Interestingly, the total Berry phase acquired in a closed loop in the Brillouin Zone (BZ) is a multiple of 2π

$$
\int_{\mathcal{BZ}}\boldsymbol{\Omega}(\mathbf{k})d^2\mathbf{k} = 2\pi C \tag{1.2.9}
$$

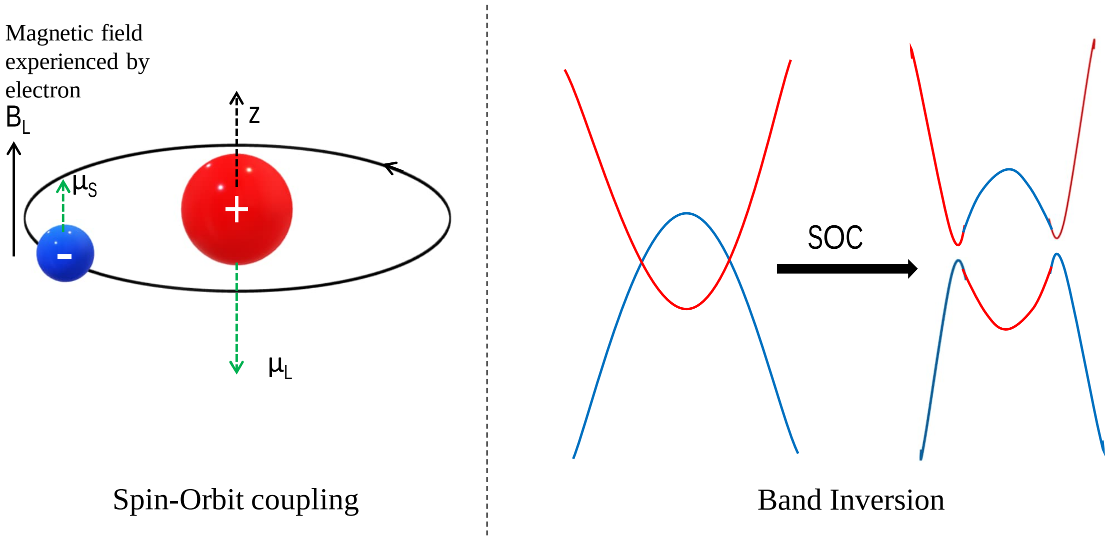

Figure 1.3: (Left) The atomic spin-orbit coupling effect on the orbital electron. (Right) Band inversion phenomenon induced by SOC in solid systems.

Here, the C is topological invariant known as Chern number. The Chern number is critical to determine whether a material is topological or not.

1.3 Spin-Orbit Coupling

In an atom, electron orbit around the nucleus with very high velocity, producing orbital angular momentum [22]. As the electron has its intrinsic spin, it interacts with the relativistic magnetic field, leading spin-orbit coupling or LS coupling. Solid state systems have an array of atoms and charge carriers, experiencing the spin-orbit interaction. Thus the Hamiltonian including the SOC is given by [23]

$$H_{SOC} = -\frac{\nabla V}{2m_0^2c^2}\mathbf{L}.\mathbf{S} = -\frac{\nabla V}{4m_0^2c^2}\sigma.\mathbf{p} \tag{1.3.1}$$

Where m_0 is the mass of a electron, c is speed of light in vacuum, $\mathbf{L}$ and $\mathbf{S}$ are the orbital and spin angular momenta, and V is the coulomb potential. In condensed matter systems, we can replace $\mathbf{S}$ by Pauli's spin matrices σ and $\mathbf{L}$ by momentum vector $\mathbf{p}$.

SOC plays a vital role in topological systems by introducing band splitting and band inversion [24]. For example, in topological insulators, the presence of strong SOC can swap the highest occupied valence band with with the lowest unoccupied conduction band , which eventually causes band inversion, as shown in Fig.1.3. In case of nodal line semi-metal, presence of SOC opens up a gap which eventually gives rise to very high Berry curvature [25].

1.4 Hall Effect

The Hall effect is a phenomenon observed when a current-carrying conductor or semiconductor is subjected to a perpendicular magnetic field. Discovered by Edwin Hall in 1879, the Hall effect resulted in the generation of a transverse voltage known as the Hall voltage [26]. This voltage is perpendicular to both current and the applied magnetic field directions. This transverse Hall voltage can be described as

$$V_H = R_H \frac{IB}{t} \tag{1.4.1}$$

Where R_H is Hall coefficient is inversely proportional to charge carrier concentration n such that $R_H = \frac{1}{ne}$. I and B are the applied current and external magnetic field strength. t is the thickness of the sample. In general, current density ($\mathbf{j}$) can be expressed in terms of resistivity tensor ($\boldsymbol{\rho}$) and electric field ($\mathbf{E} = E_x\hat{x} + E_y\hat{y}$) as,

$$\mathbf{E} = \boldsymbol{\rho}.\mathbf{j} \implies \begin{pmatrix} E_x \\ E_y \end{pmatrix} = \begin{pmatrix} \rho_{xx} & \rho_{xy} \\ \rho_{yx} & \rho_{yy} \end{pmatrix} \begin{pmatrix} j_x \\ j_y \end{pmatrix} \tag{1.4.2}$$

In terms of the conductivity tensor ($\boldsymbol{\sigma}$) we can rewrite $\mathbf{j}$ as

$$\mathbf{j} = \boldsymbol{\sigma}.\mathbf{E} \implies \begin{pmatrix} j_x \\ j_y \end{pmatrix} = \begin{pmatrix} \sigma_{xx} & \sigma_{xy} \\ \sigma_{yx} & \sigma_{yy} \end{pmatrix} \begin{pmatrix} E_x \\ E_y \end{pmatrix} \tag{1.4.3}$$

which implies $\boldsymbol{\sigma} = \boldsymbol{\rho}^{-1}$ and using the relations $\rho_{xx} = \rho_{yy}$ and $\rho_{xy} = -\rho_{yx}$ we can express the conductivity in terms of the resistivity as

$$\sigma_{xx} = \frac{\rho_{xx}}{\rho_{xx}^2 + \rho_{xy}^2} \tag{1.4.4}$$

and

$$\sigma_{xy} = \frac{-\rho_{xy}}{\rho_{xx}^2 + \rho_{xy}^2} \tag{1.4.5}$$

Later, the Hall effect branched into different types such as quantum Hall effect (QHE), quantum spin Hall effect (QSHE), anomalous Hall effect (AHE) and topological Hall effect (THE).

1.4.1 Quantum Hall Effect

In normal Hall effect, we considered the electrons as classical particles but their motion is confined in a 2D-plane. On the other hand, in the quantum picuture, the electrons motion in a 2D-plane is treated quantum mechanically using the Schródinge equation. Thus we can choose the vector potential $\mathbf{A}(\mathbf{r})$ for yhe magnetic field applied along $\hat{z}$ direction $\mathbf{A}(\mathbf{r}) =$

$xB\hat{y}$ i.e. 'Landau gauge' such that $\nabla_{\mathbf{r}} \times \mathbf{A}(\mathbf{r}) = B\hat{z}$. Now the Hamiltonian can be written as [20,21]

$$\mathcal{H} = \frac{1}{2m}\left(\mathbf{p} + \frac{e}{c}\mathbf{A}(\mathbf{r})\right)^2 = \frac{1}{2m}\left[p_x^2 + \left(p_y + \frac{eBx}{c}\right)^2\right] \tag{1.4.6}$$

Following the Born-von Karman boundary condition along y direction, we can write the solutions of this Hamiltonian as

$$\psi(x,y) = \frac{1}{\sqrt{L}}e^{ik_y y}\phi_{k_y}(x), \quad k_y = \frac{2\pi n}{L}, \quad n : \text{integer}$$

Now the Schródinger's equation becomes

$$\frac{1}{2m}\left[p_x^2 + \left(\hbar k_y + \frac{exB}{c}\right)^2\right]\phi_{k_y}(x) = \epsilon_{k_y}\phi_{k_y}(x) \tag{1.4.7}$$

From a close observation of the above equation, we can find that it mimics a harmonic oscillator in the x-direction. Thus, We can rewrite the Hamiltonian as

$$\mathcal{H} = \frac{1}{2m}p_x^2 + \frac{m\omega_B^2}{2}\left(x + kl_B^2\right)^2 \tag{1.4.8}$$

Here, $\omega_B = eB/m$ is cyclotron frequency of electron orbiting on the plane perpendicular to magnetic field $B\hat{z}$ the and $l_B = \sqrt{\frac{\hbar c}{eB}}$ is the magnetic length. The energy eigenvalues are given by

$$\epsilon_n = \left(n + \frac{1}{2}\right)\hbar\omega_B \tag{1.4.9}$$

The number of available states in a Landau system is calculated to be $N_L = \frac{BA}{\phi_0}$, where A is the area of the sample perpendicular to the magnetic field B and ϕ_0 is the magnetic flux quantum $\phi_0 = \frac{hc}{e}$. In case of Hall effect we must include the electric field $\mathbf{E} = E_0\hat{x}$ and thus the modified Hamiltonian can be rewritten for the potential energy $[V(x) = -exE_0]$

$$\mathcal{H} = \frac{1}{2m}\left[p_x^2 + \left(p_y + \frac{eBx}{c}\right)^2\right] + exE_0 \tag{1.4.10}$$

and the corresponding energy eigenvalues are given by

$$\epsilon_{n,k_y} = \left(n + \frac{1}{2}\right)\hbar\omega_B - eE\left(k_y l_B^2 + \frac{eE}{m\omega_B^2}\right) + \frac{mE^2}{2B^2} \tag{1.4.11}$$

Now the energy levels depends linearly on k_y which means there is a finite drift velocity along y direction with $v_y = \frac{1}{\hbar}\frac{\partial\epsilon_{n,k_y}}{\partial k_y} = -\frac{E}{B}$. Which is the cause of quantized Hall effect in

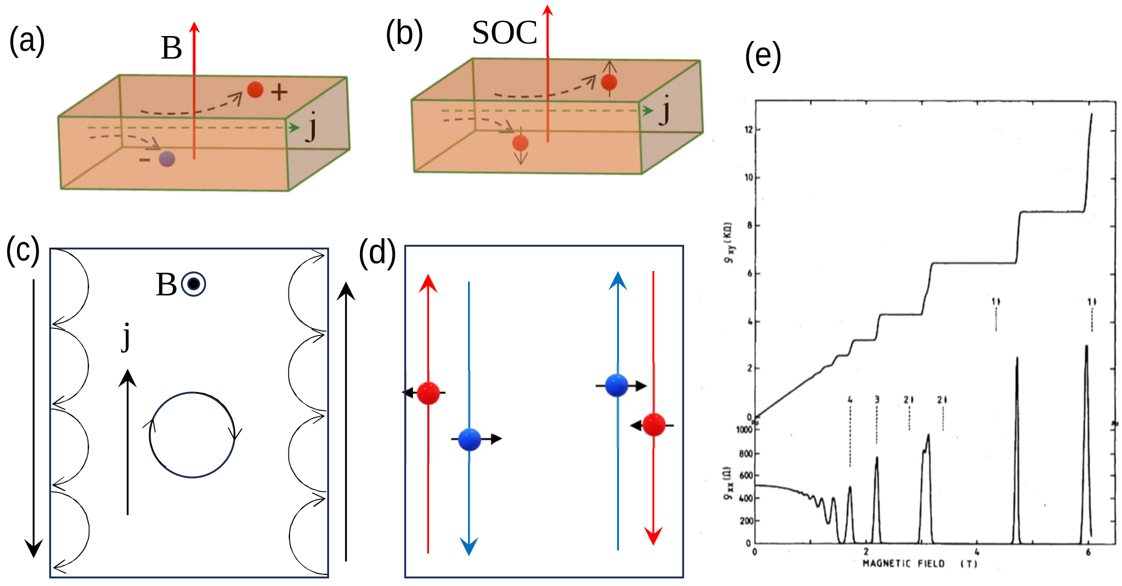

Figure 1.4: Schematic presentation of (a) normal Hall effect (b) Spin Hall effect (SHE). Quantum version of normal Hall effect or (c) integer quantum Hall effect (IQHE) and quantum version of SHE or (d) quantum spin Hall effect (QSHE). (e) Experimental observation of QHE taken from Ref [3]

y direction.

Though the system behaves as a band insulator, in presence of external magnetic field due to quantization of Hall effect, one can see conducting edge states as demonstrated in Fig.1.4(c). Further, the potential energy term $V(x)$ can be expanded as $V(x) = V(X) + (x - X)\frac{\partial V}{\partial x}$ (ignoring the higher order terms). Here we will also get drift velocity along y direction $v_y = \frac{1}{eB}\frac{\partial V}{\partial x}$. Interestingly, the edge modes are chiral and opposite i.e. $v_y < 0$ for $x > 0$ and $v_y > 0$ for $x < 0$ which explains the opposite current flow at the edges [27].

1.4.2 Quantum Spin Hall Effect

In spin Hall effect measurements, the strong spin-orbit coupling (SOC) pushes the spin-up and spin-down electrons to opposite edges of a 2D material without even applying the external magnetic field. Though the net charge current is zero in this case, there is a finite transverse spin current. Quantum spin Hall effect (QSHE) is the quantized version of the spin Hall effect. In QHE the time reversal symmetry (TRS) is broken due to the presence of magnetic field but in QSHE the TRS is preserved. This QSHE is first observed in the semiconducting HgTe quantum well, sandwiched between two CdTe layers [28, 29].

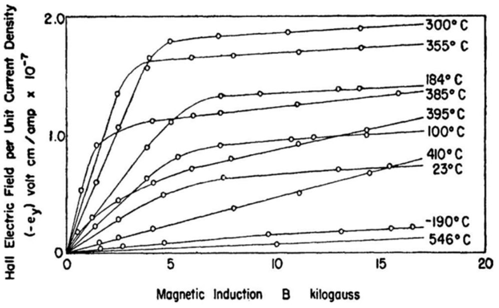

Figure 1.5: Anomalous Hall resistivity plotted as a function of applied field in a ferromagnet Ni, taken from Ref [31]

1.4.3 Anomalous Hall effect

Soon after the discovery of Hall effect in a semiconductor in 1881, Edwin Hall observed an anomalous Hall signal while replacing the semiconductor by ferromagnetic iron [30]. Thus, named as the anomalous Hall effect (AHE). In a ferromagnet, initially the Hall resistivity increases steeply, reassembly the magnetization M(H), saturating the Hall resistivity increases linearly with applied field due to normal Hall contribution. So, the total Hall resistivity can be written as,

$$\rho_H = \mu_0 R_0 H + \mu_0 R_S M \tag{1.4.12}$$

where the first term represents normal Hall effect and the second term represents the anomalous Hall effect. R_0 is the normal Hall coefficient, R_S is the anomalous Hall coefficient, and M is the magnetization. The AHE data from ferromagnet Ni, taken from Smit [31], is shown in Fig.1.5 Recently, AHE has been observed in antiferromagnetic systrms as well [32, 33]. While in antiferromagnet systems the AHE originates intrinsically, in ferromagnetic systems, there are also extrinsic origins [34]. So far, there exists three widely known microscopic theories explaining the AHE in condensed matter systems [34]

(i) Intrinsic anomalous Hall effect: In 1954, Karplus and Luttinger introduced this concept when they considered the inclusion of spin-orbit coupling which gives a finite contribution from the inter-band scattering which only depends on the electronic structure of the material [35]. Until 2002 this concept was not seriously considered by the scientific community, the AHE in topological systems compelled to vote on this theory. As per the KL theory, for the given states of $|n, \mathbf{k}\rangle$ (for n-th band with momentum k) and eigenvalues $\epsilon_n(\mathbf{k})$ of a Bloch Hamiltonian $\mathcal{H}$, one can calculate the intrinsic Hall conductivity σ_{ij}^{int} using the

Kubo formula [34],

$$\sigma_{ij}^{int} = e^2\hbar \sum_{n\neq n'} \int \frac{d\mathbf{k}}{(2\pi)^d}[f(\epsilon_n(\mathbf{k})) - f(\epsilon_{n'}(\mathbf{k}))] \times \mathrm{Im}\frac{\langle n,\mathbf{k}|v_i(\mathbf{k})|n',\mathbf{k}\rangle \ \langle n',\mathbf{k}|v_j(\mathbf{k})|n,\mathbf{k}\rangle}{[\epsilon_n(\mathbf{k}) - \epsilon_{n'}(\mathbf{k})]^2} \tag{1.4.13}$$

Here, the velocity operator can be expressed as $v_i(\mathbf{k}) = \frac{1}{\hbar}\boldsymbol{\nabla}_k\mathcal{H}(\mathbf{k})$. The Berry connection can be written as $\mathbf{A}_n(\mathbf{k}) = i\,\langle n,\mathbf{k}|\boldsymbol{\nabla}_k|n',\mathbf{k}\rangle$ which gives the Berry curvature

$$\boldsymbol{\Omega}_n(\mathbf{k}) = \boldsymbol{\nabla}_k \times \mathbf{A}_n(\mathbf{k}) \tag{1.4.14}$$

By solving the Boltzman's semi-classical transport equation, one can get the equation of motion as

$$\frac{d\langle\mathbf{r}\rangle}{dt} = \frac{1}{\hbar}\frac{\partial\mathbf{E}}{\partial\mathbf{k}} - \frac{e}{\hbar}\mathbf{E}\times\boldsymbol{\Omega}_n(\mathbf{k}) \tag{1.4.15}$$

The first term is the drift velocity of the electron in presence of external electric field and second term suggests electron motion transverse to the applied electric field to produce the anomalous Hall conductivity. As the intrinsic Hall conductivity (IHC) is calculated by integrating over the entire Brillouin Zone (BZ), IHC would be temperature independent if there is no change in the electronic band structure. Further, the anomalous Hall resistivity (ρ_{ij}^{int}) quadratically dependence with on the longitudinal resistivity (ρ_{ii}) such that $\rho_{ij}^{int} \propto \rho_{ii}^2$.

(ii)Extrinsic Anomalous Hall effect

(a) Skew-scattering mechanism: In 1955, Smit first proposed that the main reason for the anomalous Hall effect is from the asymmetric (skew) scattering of electrons with the impurities in the presence of strong spin-orbit interaction [36,37]. The Fermi's golden rule describe the probability of transition from a initial state n to final state n' as $W_{n\rightarrow n'} = \frac{2\pi}{\hbar}|\,\langle n|\Delta H|n'\rangle\,|^2\delta(E_n - E_{n'})$ where ΔH is the perturbation inducing the transition. In the presence of SOC and magnetization the scattering probability of $n \rightarrow n'$ and $n' \rightarrow n$ transitions is not same. The transition probability takes the form

$$W_{kk'}^{A} = -\tau^{-1}\mathbf{k}\times\mathbf{k'}.M_S \tag{1.4.16}$$

If the transport life time (τ) is high, the skew scattering contribution dominates the total Hall effect and the anomalous Hall resistivity is linearly proportional to the longitudinal resistivity $\rho_{ij}^{skew} \propto \rho_{ii}$ [34].

(iii) Side-jump mechanism: In 1964, Berger introduced the side-jump mechanism to explain the anomalous Hall effect [38]. In semiclassical approach when a gaussian wave packet scatters from a spherical impurity, the wave packet with incident wave vector **k** displace transverse to its initial direction. This phenomenon is called side-jump. In this case anomalous Hall resistivity is quadratically proportional to longitudinal resistivity $\rho_{ij}^{side} \propto \rho_{ii}^2$. Interestingly, unlike in the skew-scattering mechanism, in the side jump case the Hall conductivity is independent of the longitudinal conductivity [38]. Thus, the extrinsic side Hall conductivity is $\sigma_{ij}^{side} = \frac{e^2}{\hbar}(\frac{\epsilon_{SOC}}{E_F})$ where ϵ_{SOC} is the spin-orbit coupling energy and E_F is Fermi energy.

1.4.4 Topological Hall effect

However, recently a different component of the Hall effect, which is distinguishable from the AHE, has been discovered in many non-coplanar magnetic systems. This special type of Hall effect now widely popular as the topological Hall effect (THE) is mainly found in the system with non-coplanar chiral spin structure. While the AHE in non-collinear systems is originating from finite k-space Berry curvature, the THE comes due to finite real space Berry curvature in the system. This topological Hall effect is mainly found in the skyrmion crystals [39, 40], canted antiferromagnets [41, 42], and spin glass systems [43]. The total Hall resistivity can be expressed as,

$$\begin{aligned} \rho_{xy}(H) &= \rho_{xy}^N(H) + \rho_{xy}^A(H) + \rho_{xy}^T(H) \\ &= \mu_0 R_0 H + \mu_0 R_S M + \rho_{xy}^T(H) \end{aligned} \tag{1.4.17}$$

Now, as this THE is coming from non-coplanar chiral spin structure, the value of topological Hall resistivity (ρ_{xy}^T) can be negligible in the presence of strong magnetic field, as all spins try to align in the direction of applied field. So, in high magnetic fields region $\rho_{xy}^T \to 0$ and we can rewrite the Eqn. 1.4.17 as,

$$\frac{\rho_{xy}^T}{\mu_0 H} = R_0 + R_S \frac{M}{H} \tag{1.4.18}$$

By fitting the Hall resistivity data with Eqn. 1.4.18 in the high field region, we estimate the normal and anomalous Hall coefficient (R_0 and R_S). By inserting R_0 and R_S values in the main Eqn. 1.4.17, we can extract topological Hall resistivity contribution from the total Hall resistivity.

In special cases the non-coplanar magnetic structures can become topologically non-trivial spin textures in presence of certain magnetic interactions inside the system. Such examples are skyrmion, anti-skrymion, and biskyrmion [40, 45–49]. The quantity which distinguishes among this non-trivial spin structures is called the topological charge or wind-

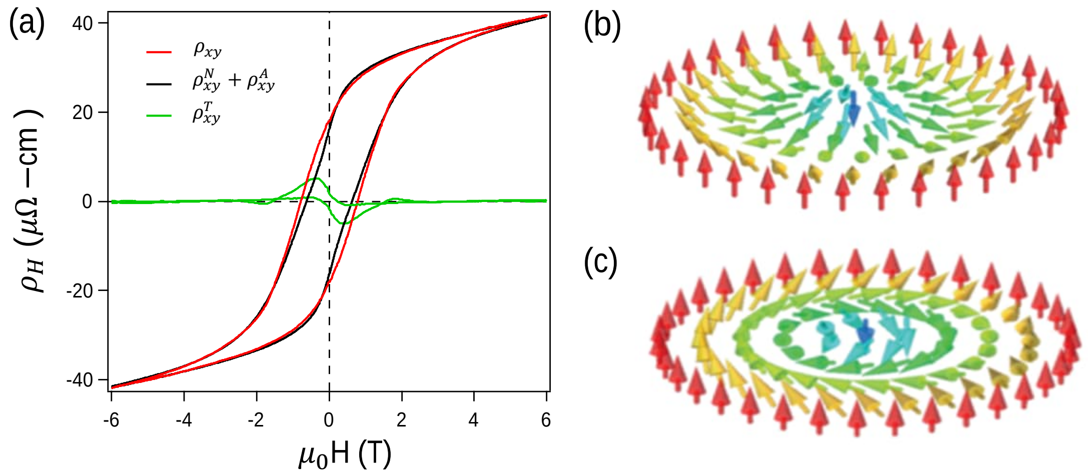

Figure 1.6: (a)Different types of Hall contributions to the to the total Hall resistivity. Here, ρ_{xy}: total Hall resistivity; ρ^N_{xy}: normal Hall resistivity; ρ^A_{xy}: anomalous Hall resistivity; ρ^T_{xy}: topological Hall resistivity. (b) Néel and (c) Bloch type skyrmions, images are taken from Ref [44]

ing number Q [49].

Skyrmion: Skyrmions are a special kind of non-coplanar arrangement of spin-strucutres, where the winding number $Q = \frac{1}{4\pi}\int \mathbf{m}.(\partial_x\mathbf{m} \times \partial_y\mathbf{m})dxdy$ would be either $+1$ or -1. A skrymion would form in a magnetic system if there exists atleast two competitive interactions in the system. In general, Hamiltonian of a magnetic system can be expressed (including several magnetic interactions) as

$$\mathcal{H} = -\sum_{<i,j>} J_{ij}S_i.S_j - h_z\sum_j S^z_j + \mathcal{H}_{DM} + \mathcal{H}_{single-ion} + \mathcal{H}_{dipole} + \mathcal{H}_{RKKY} \qquad (1.4.19)$$

The first term corresponds to Heisenberg interaction, second term is due to Zeeman splitting, third term is for Dzyaloshinskii–Moriya interaction, fourth term corresponds to single-ion anisotropy, fifth term refers to dipole-dipole interaction, and sixth term is due to Ruderman-Kittel-Kasuya-Yosida (RKKY) interaction. In a non-centrosymmetric system the Dzyaloshinskii–Moriya term $\mathcal{H}_{DM} = \sum_{i,j}\mathbf{D}_{ij}.(\mathbf{S}_i \times \mathbf{S}_j)$ would play a critical role. In a non-centrosymmetric system the inversion symmetry is broken resulting finite $\mathbf{D}_{ij}$ term. Several non centrosymmetric systems fall into this category such as MnSi and FeGe [50, 51]. In rare-earth based triangular magnets, the Ruderman-Kittel-Kasuya-Yosida (RKKY) interaction (in which the localized spins are coupled though the conduction electrons) along with magnetic frustration, can stabilize skyrmions as seen in Gd_2PdSi_3 [48] and $Gd_3Ru_4Al_{12}$ [52]. In case of centrosymmetric magnets, like Fe_3Sn_2 [53], the competition between single ion anisotropy and the dipole-dipole interaction is the main source of the skrmion formation. As the charge carriers move through a skyrmion, they experience real space Berry curvature which is nothing but a pseudo magnetic field. The strength of topological Hall resistivity depends on this pseudo magnetic field expressed by

$$\rho_{xy}^{T} = PR_0B_{eff} \tag{1.4.20}$$

where P is the polarization factor, $P = \mu_{spon}/\mu_{sat}$, R_0 is the normal Hall coefficient, and B_{eff} is the effective pseudo magnetic field [54–56]. This effective pseudo magnetic field depends on the skymion density as

$$B_{eff} = \phi_0 n_{sk} \tag{1.4.21}$$

Here, ϕ_0 is flux quanta and n_{sk} is skyrmion density [54–56]. Thus, the skyrmion density in a system can be indirectly estimated using the topological Hall resistivity data.

1.5 Symmetries

As discussed earlier, a system will be topologically invariant if it is protected by atleast one of the two symmetries. They are (i) time reversal symmetry (TRS) and (ii) Point group symmetry.

1.5.1 Point group symmetry

After imposing the Point-group symmetry if lattice is unchanged, we say that the system is invariant under point-group operation [57]. Point-group symmetries are unitary operators. There are several point-group symmetries such as inversion, reflection, rotation, and rotoreflection. Among them the inversion symmetry plays an important role in developing topological state in a condensed matter system. Under inversion symmetry, a left-handed system would become right-handed. It is an unitary operation such that $k \to -k$ and $\hat{P}^2 = 1$. If $\hat{P}$ is inversion operator acting on the position $\hat{x}$, then the expectation value would become

$$\langle\phi|\hat{P}^{-1}\hat{x}\hat{P}|\phi\rangle = -\langle\phi|\hat{x}|\phi\rangle \tag{1.5.1}$$

So, $\hat{x}$ is odd under inversion. In inversion invariant system the energy eigenvalues can be written as

$$E_{n,s}(-k) = E_{n,s}(k) \tag{1.5.2}$$

and for Berry curvature,

$$\Omega(-k) = \Omega(k) \tag{1.5.3}$$

1.5.2 Time reversal symmetry

Time reversal symmetry is an antiunitary operator. If it acts on position $\hat{x}$ is would be unchanged. If it acts on the momentum $\hat{p}$ and spin $\hat{s}$, their signs will be reversed in such way that

$$TR : \; \hat{x} \rightarrow \hat{x}, \; \hat{p} \rightarrow -\hat{p}, \; \hat{s} \rightarrow -\hat{s} \tag{1.5.4}$$

In a spin-$1/2$ system, TRS acts as,

$$\hat{T}^{-1}\sigma_i \hat{T} = -\sigma_i \;\; (i = x, y, z) \tag{1.5.5}$$

Where σ_i are Pauli's spin matrices. If a system in invariant under the time reversal symmetry, the Hamiltonian of the system would be unchanged. Then,

$$E_{n,-s}(-k) = E_{n,s}(k) \tag{1.5.6}$$

and for the Berry curvature, there would be a sign change

$$\Omega(-k) = -\Omega(k) \tag{1.5.7}$$

1.6 Topological Semimetals

In 1928, Dirac introduced his famous relativistic equation for the fermions by incorporating both the single particle quantum mechanics and the special theory of relativity [58,59]. The wave equation of spin 1/2 electron in the relativistic limit (Dirac equation) can be written in the covariant form as

$$(i\hbar\gamma^{\mu}\partial_{\mu} - mc)\psi = 0 \tag{1.6.1}$$

Here $\mu = 0, 1, 2, 3....$ is the dimensionality of the space, c is the speed of light in vacuum, and m is the rest mass of the fermion. Dirac proposed this equation for free fermions, in the vacuum, in the high energy limit where the energy of the particles is linearly dependent with its momentum according to Einstein's equation $E^2 = (pc)^2 + (m_0c^2)^2$. In condensed matter systems, there are several other interactions are present. Thus, the electrons inside the systems are not independent but collectively they are quasiparticle excitations which follow Dirac wave equation, called as Dirac fermions (massive, $m \neq 0$) in the condensed matter systems. The systems hosting the Dirac fermions are called Dirac semimetals.

Soon after Dirac proposed his revolutionary wave equation, in 1929, Hermann Weyl

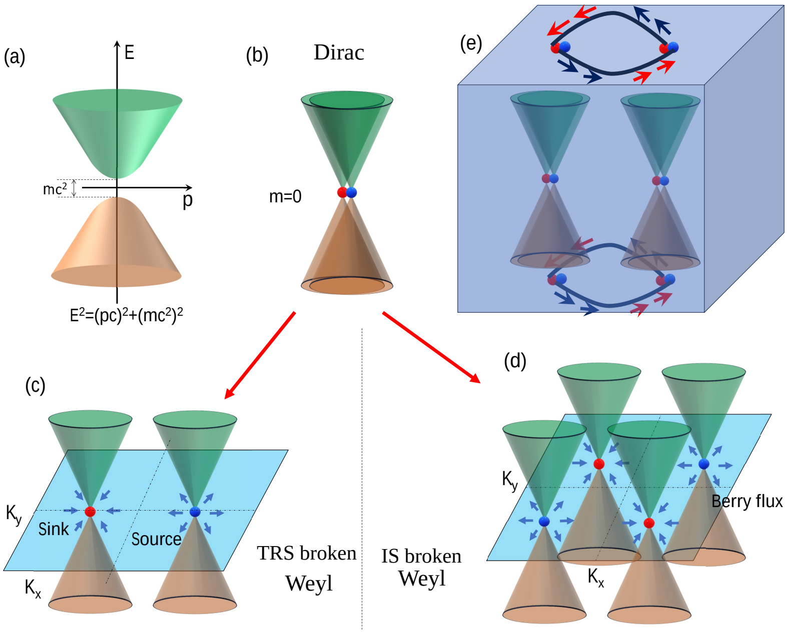

Figure 1.7: (a) Band diagram of free Dirac particle with mass m (b) Energy band diagram of a massless Dirac fermion which form a Dirac point at the band touching point. Dirac point splits into minimum. (c) Two Weyl points due to time reversal symmetry (TRS) broken. (d) Four Weyl points due to inversion symmetry (IS) broken. (e) Surface states of a Dirac semimetal. Images are reproduced from [19]

derived the equation [60, 61] for the massless fermions, which is

$$i\hbar\partial_t\psi_\pm = \pm c\mathbf{p}.\sigma\psi_\pm \tag{1.6.2}$$

Where $\psi_\pm$ represents the wave vector with chirality $'+'$ or $'-'$ corresponding Hamiltonian $\mathcal{H}_\pm = \pm c\mathbf{p}.\sigma$. Here σ is Pauli's spin matrices. Until recently, the concept of massless fermions only existed in high energy physics. But in these recent days several condensed matter systems showed the presence of massless fermions called the Weyl fermions. The systems hosting the Weyl fermions are called the Weyl semimetals. There should be atleast two Weyl points in a Weyl semimetal with chirality $'+'$ and $'-'$ with corresponding energy eigenvalues $E = \pm pc$. At $p = 0$, a doubly degenerate Weyl node forms. In a Weyl semimetal, the Weyl nodes with $'+'$ and $'-'$ chiralities are separated by crystal momentum $\mathbf{k}$. Now, if two Weyl points with opposite chirality merge at a single $\mathbf{k}$ point in the momentum space, a Dirac node with four-fold degeneracy will be generated making it a massless Dirac fermion. [62, 63] In other words, if we break the degeneracy of a Dirac point, we can get at least two Weyl points.

Figure 1.7(b) represents a Dirac cone formed by linear band crossings. This Dirac point is protected by both inversion (IS) and time reversal (TRS) symmetries. By breaking one

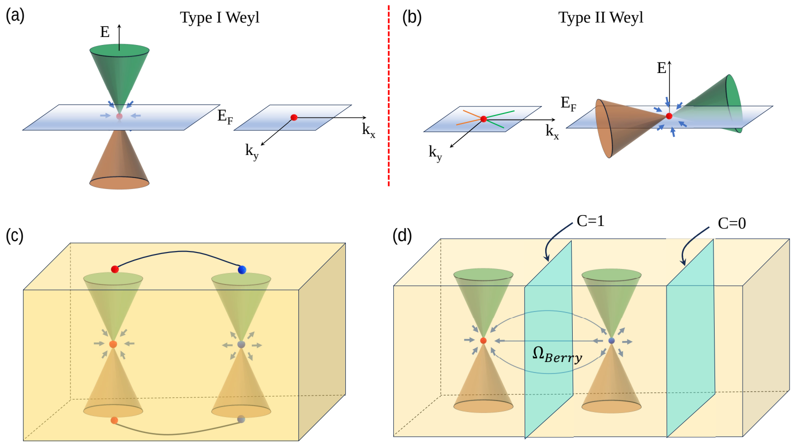

Figure 1.8: (a) Type I and (b) Type II Weyl semimetal and their energy contours in k$_x$-k$_y$ space. (c) Fermi arcs connecting the Weyl points in the surface. (d) finite Berry curvature introduced by the Weyl pair and topological Chern number associated with the different planes inside the momentum space. Images are reproduced from [19]

of these two symmetries, the Dirac point splits into two Weyl points. If TRS is broken there will be minimum two Weyl points, protected by inversion symmetry, while the IS is broken system generates four minimum Weyl points that are protected by the time reversal symmetry [see Fig. 1.7 (c) and (d)]. Maintaining time-reversal symmetry (TRS) makes sure that Weyl nodes in both positive and negative momentum (k and -k) exhibit same chirality and to counterbalance these Weyl nodes with the same chirality, a pair with opposite chirality emerges. In TRS broken Weyl semimetal, two Weyl nodes with opposite chirality arise at an equivalent energy level due to the inversion symmetry protection [64].

The first Dirac fermion is observed in graphene [65], a 2D Dirac semimetal. Realization of 3D Dirac semimetal (DSM) is challenging as the mass term m in the electronic Hamiltonian will open up a gap in the presence of SOC, hence extra symmetries are required to protect the Dirac point. There are mainly two ways to get a 3D DSM. One is band inversion mechanism, where the Dirac nodes emerge as a result of lattice symmetries (often rotational symmetry) inducing accidental band crossings into an inverted band structure of a topological insulator and another one is symmetry enforced Dirac node [64]. The main characteristic of a Dirac semimetal is the presence of two Fermi arcs linking a pair of Dirac points on the surface [see Fig.1.7(e)]. Dirac semimetals exhibit remarkable electrical transport properties such as ultra-high mobility and significant magneto-resistance.

Depending on the orientation of the Weyl cone in the energy-momentum space, a Weyl semi-metal can be of two types (in general) (i) Type-I Weyl semimetal which gives point-like Fermi surface and (ii) Type-II semimetal where the Weyl cone is tilted in E-k space and

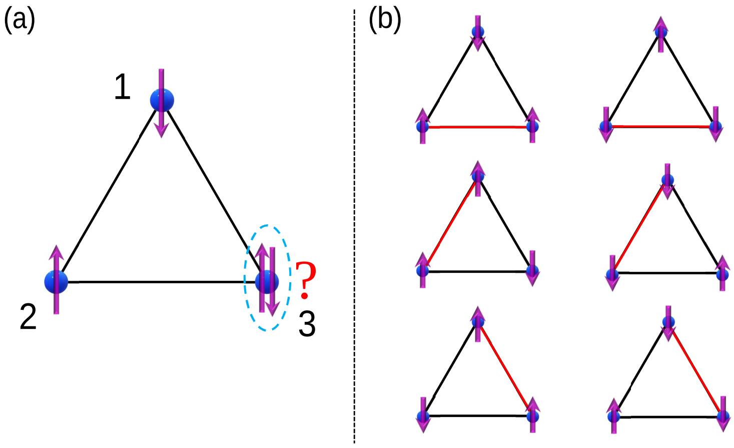

Figure 1.9: (a) Geometric frustration in triangular Ising antiferromagnet. (b) Possibility of different ground states in triangular Ising antiferromagnet

because of the tilt, both the hole and electron bands present around the Weyl points. The constant energy contour reveals the Weyl point as a point where both the bands touch each other [see Fig.1.8 (a) and (b)]. A unique characteristic of Weyl fermions is the presence of magnetic monopoles. The topology of the Weyl point on the Fermi surface is connected to the Berry curvature, acting as an effective magnetic field in the momentum space. Weyl nodes on the Fermi surface serve as magnetic monopoles, acting as both a source and sink for the Berry curvature. The magnetic charge of a Weyl node, known as chirality, can be calculated by integrating over the Fermi surface enclosing the node [see Fig.1.8(d)]. Weyl points on the Fermi surface also create Fermi arcs, connecting the surface projections of two Weyl nodes in Weyl semimetals as shown in Fig.1.8(c). These Fermi arcs are guaranteed to exist due to the magnetic monopole nature of Weyl fermions. Further, topologically protected Fermi arcs on opposite surfaces are connect the bulk Weyl points [64].

1.7 Kagome lattice systems

The crystal and/or lattice structure plays a vital role in predicting exotic physical properties in a system. As mentioned earlier, the topological state in a matter is protected by symmetries which is inbuilt in the crystal structure. For example, symmetry enforced degeneracy plays a crucial role in protecting the Dirac crossings in a 3D material [64]. Apart form the band structure topology, some other quantum phenomena are also being influenced by the lattice structure. One of such examples is the geometrical frustration, leading to the quantum spin liquid state. Kagome lattice systems are becoming very popular these days due to their their unique structure which has the potential to host several interesting physical properties.

1.7.1 Frustration

In general, frustration appears in a system if there exists several competitive interactions such that there is no definite ground state. A simplest example would be a triangular Ising antiferromagnet as shown in Fig.1.9(a). As one can see that the spin configuration of the third site always be in frustrated state i.e., no definite spin ordering with respect to the other two neighbouring spins. In this case there are six different spin states are possible, as shown in Fig.1.9(b) which prevents ordering. The ground state would be a superposition of all the six states which makes the spins entangled to each other. Now, along with long range entanglement of the spins, this new state originates features like the fractional spin excitations leading to quantum spin liquid state [66–68]. Kagome lattice consisting hexagons with corner sharing triangles has inbuilt geometrical frustration, provides a stage for the quantum spin liquid state. $KCu_6AlBiO_4(SO_4)_5Cl$ [69] and $YCu_3(OH)_6Br_2[Br_x(OH)_{1-x}]$ [70] are some examples of the kagome lattice systesms.

1.7.2 Electronic properties

The electron tight-binding Hamiltonian $\mathcal{H} = -t\sum_{<ij>,\sigma}(c^{\dagger}_{i,\sigma}c_{j,\sigma} + h.c.)$ for a kagome lattice, with nearest-neighbor hopping denoted by -t and h.c. denotes the Hermitian conjugate where $c_{i,\sigma}$ and $c^{\dagger}_{i,\sigma}$ are the spin-electron annihilation and creation operators, displays a peculiar feature in its electronic band structure [15, 71] as shown in Fig.1.10(d). A perfect flat band appears at an energy of $E_3 = 2t$ which spreads across the whole Brillouin zone [Fig.1.10(g)]. This flat band emerges from subdimensional eigen-wavefunctions where hoppings cancel out exactly due to the lattice geometry as shown in Fig.1.10(b). Also Dirac cones would emerge at the corners of the hexagonal BZ [Fig.1.10(e)]. In addition two van Hove singularities also appear at the boundary of the BZ [Fig.1.10(f)]. The spin-orbit coupling causes a gap to appear at the Dirac point within the band structure. Introducing an out-of-plane magnetization $H_{M_z} = -M_z\sum_{i,s_z=\pm\frac{1}{2}} s_z c^{\dagger}_{i,s_z} c_{i,s_z}$ to the kagome lattice, where M_z represents the z-direction Zeeman field, effectively removes the spin $s = \pm 1/2$ degeneracy. Consequently, the topological gap transforms into a Chern gap, resulting in the emergence of chiral edge states on the kagome lattice. This Chern gap can be tuned by the strength of SOC and direction of magnetization. The Chern gap gives rise to quantum anomalous Hall effect [15, 72],. On the other hand, the flat bands could potentially give fractional charge excitations producing fractional quantum Hall effect.

So far, several Kagome systems have been explored and demonstrated their interesting properties [32, 73–76]. For example, $Co_3Sn_2S_2$ has trigonal crystal structure with Co atoms forming the Kagome lattice. It shows giant intrinsic anomalous Hall effect originated from

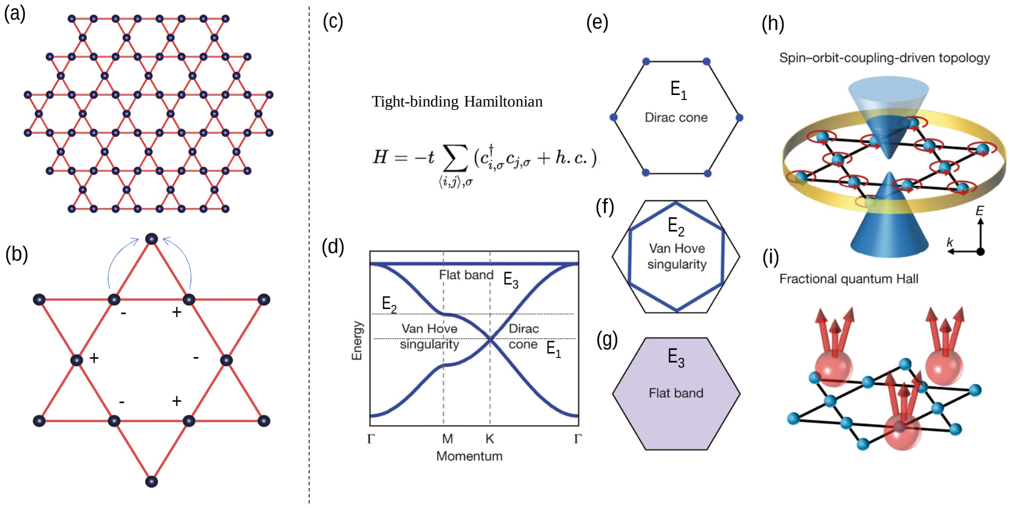

Figure 1.10: (a) a Kagome lattice. (b) Electron confinement within a kagome lattice featuring nearest-neighbor hopping, where the plus and minus signs denote the phase of the flat band eigenstate at adjacent sublattices. (c) Tight-binding Hamiltonian and (d) electron band structure obtained using this Hamiltonian. (e) Dirac cones (f) van Hove singularities (g) Flat band in the hexagonal Brillouin zone. (h) Chern gap open up due to spin-orbit coupling (i) fractional charge excitation due to the persence of flat band. (d)-(i) are taken from Ref [15].

the k-space Berry curvature due to the broken time reversal symmetry [77]. It also shows the Weyl fermions producing chiral anomaly in this system [73, 77]. Mn_3X (x = Sn, Ge) are well known antiferromagnets. Previously, the anomalous Hall effect was only observed in ferromagnets. In 2015, Nakatsuji et. al. [32] first time showed the presence of anomalous Hall effect in Mn_3Sn, though being an antiferromagnet. The intrinsic anomalous Hall effect of Mn_3X systems is due to the non trivial Berry curvature associated with the time reversal symmetry broken type-II Weyl point present in these systems, making them topological magnetic Weyl semimetal [33, 78–80]. On the other hand, FeSn and CoSn are known to show flat bands in their electronic band structure [74, 81, 82]. AV_3Sb_5 (A = alkaline metals) compounds exhibit superconductivity [75, 83] along with charge density wave (CDW). These are promising candidates for the topological superconductivity which can host Majorana fermions [84]. Recently, rare-earth based Kagome systems RMn_6Sn_6 [76] are gaining a lot of research interests posses a clean Mn-based Kagome network. Also, $TbMn_6Sn_6$ is discovered to show quantum limit Chern magnet [72].

Chapter 2

Experimental Details

There are two ways to look into exotic topological properties in condensed matter systems. One is theoretical approach in which solving model Hamiltonian of a system (analytically or numerically) reveals its topological properties. Another one is experimental approach, in which a researcher work on real systems by synthesizing materials and studying its various topological properties. This thesis is based on experimental approach. Here, we have briefly discussed about the experimental methods used and their working principles.

2.1 Single Crystal Growth

A single crystal is a substance where the atoms are arranged in a consistent and unbroken pattern throughout the material. Unlike polycrystals, single crystals have no grain boundaries or structural interruptions within the substance which is very important to understand the material's true nature and to determine its potential applications.

There are variety of techniques to grow single crystals. A single crystal can be grown by the (i) liquid to solid, (ii) vapour to solid, and (iii) solid to solid phase transitions. For example, Bridgman, Czochralski, and flux methods are based on liquid to solid phase transition. Whereas, chemical vapour transport (CVT), chemical valour deposition (CVD) transform the substance from a vapour phase to a solid phase. The example of solid to solid phase transition hapens during the solid-state reaction, in which the initial components that are used to grow crystals are in solid form and the crystals would be grown by diffusion. In this thesis, I have mainly used flux growth method and solid state single crystal growth (SSSG) method. To grow $Mn_{3-x}Fe_xSn$ and $HoMn_6Ge_6$ single crystals I have used flux growth method and to grow Fe_3Sn single crystal I have used SSSG method. The details of these methods are discussed in the below sections.

2.1.1 Flux growth method

Before going into the details of flux growth method, one needs to understand the basic things like binary phase diagram, supersaturation condition, nucleation, and finally the crystallization process.

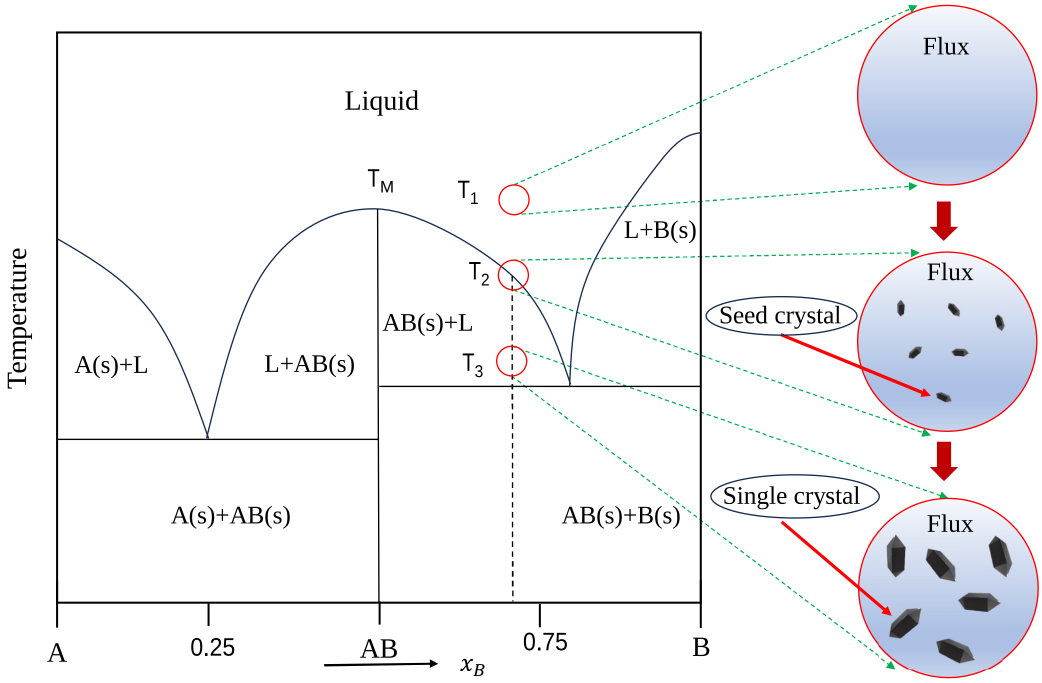

Figure 2.1: Binary phase diagram of component A and B. Image is reproduced from [85]

Binary phase diagram: Phase diagrams represent the relationships among different phases within a pressure-temperature-composition (p-T-x) space dictated by thermodynamic principles. Phase diagram can be classified, based on the number of components present in the systems, such as single, binary, and three component phase digram. In two component binary phase diagram pressure would be fixed while the different phases will be shown in temperature (T) and composition (x) space. For example, Fig.2.1 depicts a binary phase diagram of two components A and B. AB is a compound that is formed by the elements A and B. There are many zones and zone boundaries. A(s)+AB(s) zone suggests that in this region both A and AB are present but in solid form and the zone A(s)+AB(s) and AB(s)+B(s) are separated by the zone boundary AB line. Whereas AB(s)+L zone has solid AB compound and a liquid phase.

Crystal nucleation and growth: As one can see from Fig.2.1, if we consider the vertical dashed line in the phase digram, we can see the three temperature regions T_1, T_2, and T_3 with different characteristics. In the temperature region T_1, the system will be in liquid form dissolved in the flux (molten). Further reducing the temperature to T_2, the molten would be in the supersaturated liquid state. A slight decrease in the temperature starts the crystal nucleation process with micron sized crystals, these crystals are called the seed crystals. As the temperature gradually decreases to T_3, the seed crystals grow bigger in size. Note that,

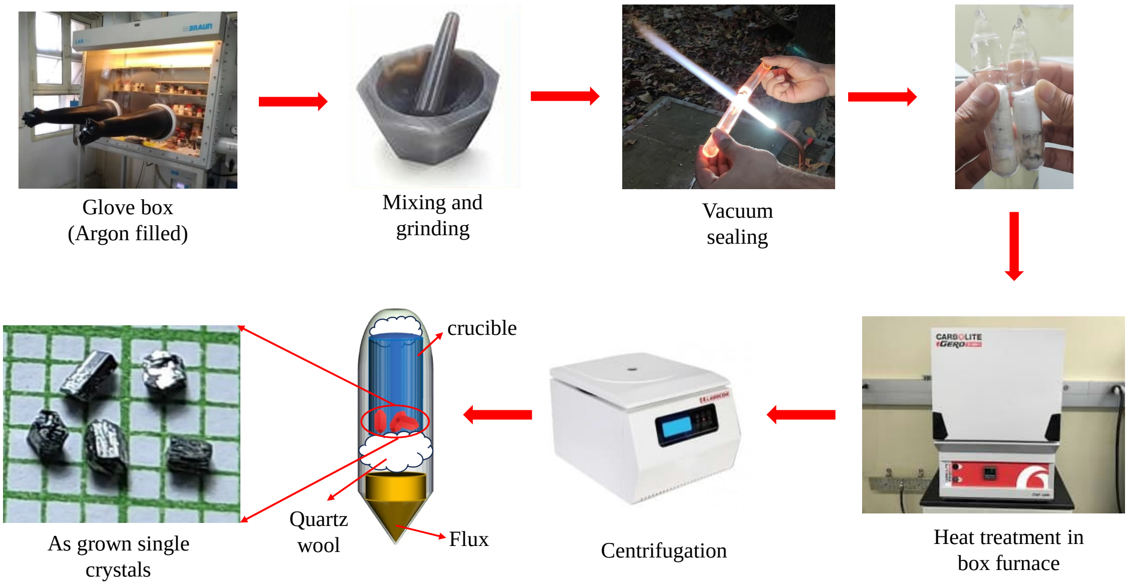

Figure 2.2: Flow chart of flux growth method

T_3 should be the temperature at which the flux should be in the liquid form. At T_3, one need to separate the crystals from the flux by centrifuging.

In this method, the flux comes from one of the elements of the desired compounds, such as A or B in case of AB. On the other hand, if the flux melting temperature is very high, one can choose a low-temperature-melting third-party flux. In this case both A and B elements get dissolved in the third-party flux to form AB.

Figure 2.2 describes the flux growth method sequentially. First, all the required precursor elements are weighed for appropriate quantity and mixed inside an argon filled glove box to avoid any oxidization and moisture formation. Then the mixture is poured into an alumina crucible and covered with quartz wool. This crucible is inserted into a quartz ampoule. After that, the quartz ampoule is sealed under partial argon atmosphere. Next, this whole object is subjected to undergo heat treatment inside a high-temperature electric box furnace, that is set to a fixed temperature at which all the elements would be melted. Then the furnace temperature is cooled down slowly to lower temperature ($\sim 2^{o}$C/hr). After that, the red-hot quartz ampoule is taken out of the furnace and placed it into a centrifuge to separate out the flux from the crystals. The formed crystals will be found on the top of the quartz wool which act as a filter to remove the excess flux as shown in Fig. 2.2. This way one can use the flux-growth technique to grow the single crystals.

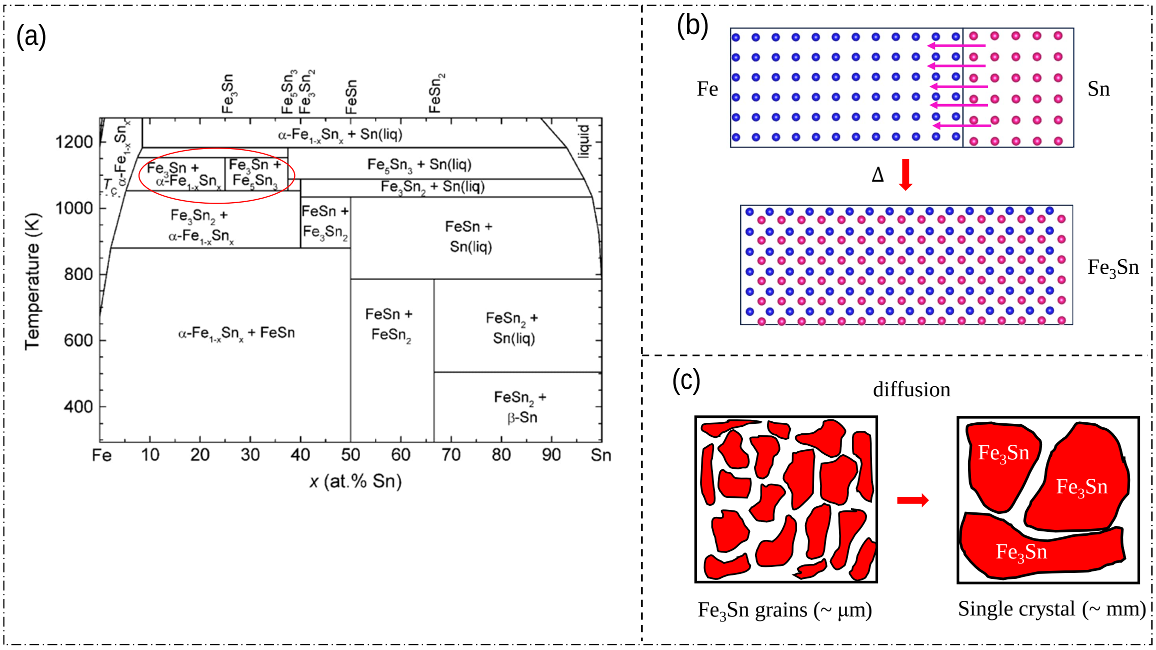

Figure 2.3: (a) Binary phase diagram of Fe-Sn system taken from Ref [86]. (b) Schematic presentation of growth of Fe_3Sn where Sn atoms diffuse to Fe chunks. (b) Fe_3Sn grains transformed to single crystals after heat treatment.

2.1.2 Solid State Single Crystal Growth (SSSG)

In the flux growth method, the precursors have to be melted either congruently (where the precursors are in stoichiometric ratio and have finite melting point) or incongruently (by adding other element or by taking more amount of one of the precursor element to reduce the meting temperature of the system) but in some systems it is possible that some compound could melt neither congruently nor incongruently. In such cases, it would be ideal to use other approach and one such approach is solid state single crystal growth (SSSG) technique which is a solid to solid phase transition.

For example consider the phase digram of Fe-Sn binary system as shown in Fig. 2.3(a). As one can see there are many compounds such as Fe_3Sn, Fe_5Sn_3, Fe_3Sn_2, FeSn, and $FeSn_2$. Now, if one choose to grow Fe_3Sn single crystal, it has no congruent melting point and Sn can not be used as a flux as Fe_5Sn_3 also forms around at the same temperature which prevents incongruent melting. So, here Fe_3Sn single crystal can be formed using SSSG method. In this method, high purity powder of Fe and Sn elements can be mixed and ground properly to make a homogeneous solid solution. With the application of temperature (where Fe_3Sn phase is stable in the phase diagram) the Sn atoms can diffuse to Fe grains and can form small Fe_3Sn grains in the mixture as shown schematically in Fig. 2.3(b). After a prolonged period of heat treatment (anealing), these micrometer size grains can merge together to form small milimeter size single crystals. This method is based on diffusion process which is why it is a slow process.

2.2 Structural characterization: X-ray diffraction

To know the structural information of the as grown single crystals, it is necessary to perform X-ray diffraction measurements on the grown samples. As we know, the inter-atomic distances in a solid is very small ($\sim$Å), so the visible range electromagnetic wave cannot be used for the diffraction as its wave-length is $\sim\ 10^3$ Å. Instead, X-ray is used to determine the crystal structure using the diffraction phenomenon as its wave length is comparable to the inter-atomic distances. In the X-ray diffraction technique, an X-ray beam of particular wavelength λ is incident on the surface of the crystal as shown in Fig. 2.4(a). The angle between the X-ray and the crystal surface is called the incident angle (θ). The X-ray reflected from different lattice planes, which introduces phase difference, causing constructive or destructive interferences. From Fig. 2.4(a) we can see the path difference is $2dsin\theta$ hence the phase difference is $\frac{2\pi}{\lambda}2dsin\theta$. For constructive interferences, the phase difference has to be even multiple of π. Thus,

$$\frac{2\pi}{\lambda}2dsin\theta = 2n\pi \implies 2dsin\theta = n\lambda \tag{2.2.1}$$

Where n is an integer. The Eqn. 2.2.1 is called Bragg's law of diffraction. By collecting the diffracted X-rays as a function of θ, one can observe intensity peaks at specific θ values, indicating constructive interference. Through the calculation of the lattice plane distance (d), using the Bragg's relation, we can estimate the lattice constants and symmetry of the crystal.

A XRD setup is schematically depicted in Figure 2.4(b). The process begins with the generation of X-rays by initiating an electron beam within a highly evacuated X-ray tube (Coolidge tube) through thermionic emission from a heated tungsten (W) cathode. This electron beam is directed towards a copper (Cu) anode to produce characteristic X-rays. Subsequently, the generated characteristic X-ray passes through various slits to form a focused X-ray beam that impinges on the sample surface. The diffracted X-ray beam is then guided through additional slits such as the Parallel slit analyzer, Soller slit, and receiving slit to enhance beam focus and the peak intensity of the collected XRD data. XRD measurements were conducted using a Rigaku SmartLab X-ray diffractometer (9 kW) with Cu-Kα radiation (λ = 1.5406Å) [see Figure 2.4(c)]. In this setup, electrons emitted from the W-cathode are accelerated by a voltage difference of 20-45 kV between the cathode and anode, while the electron current is maintained within 10-200 mA. This configuration generates an electron beam of up to 9 kW, which strikes the Cu anode to produce Cu Kα1 X-rays.

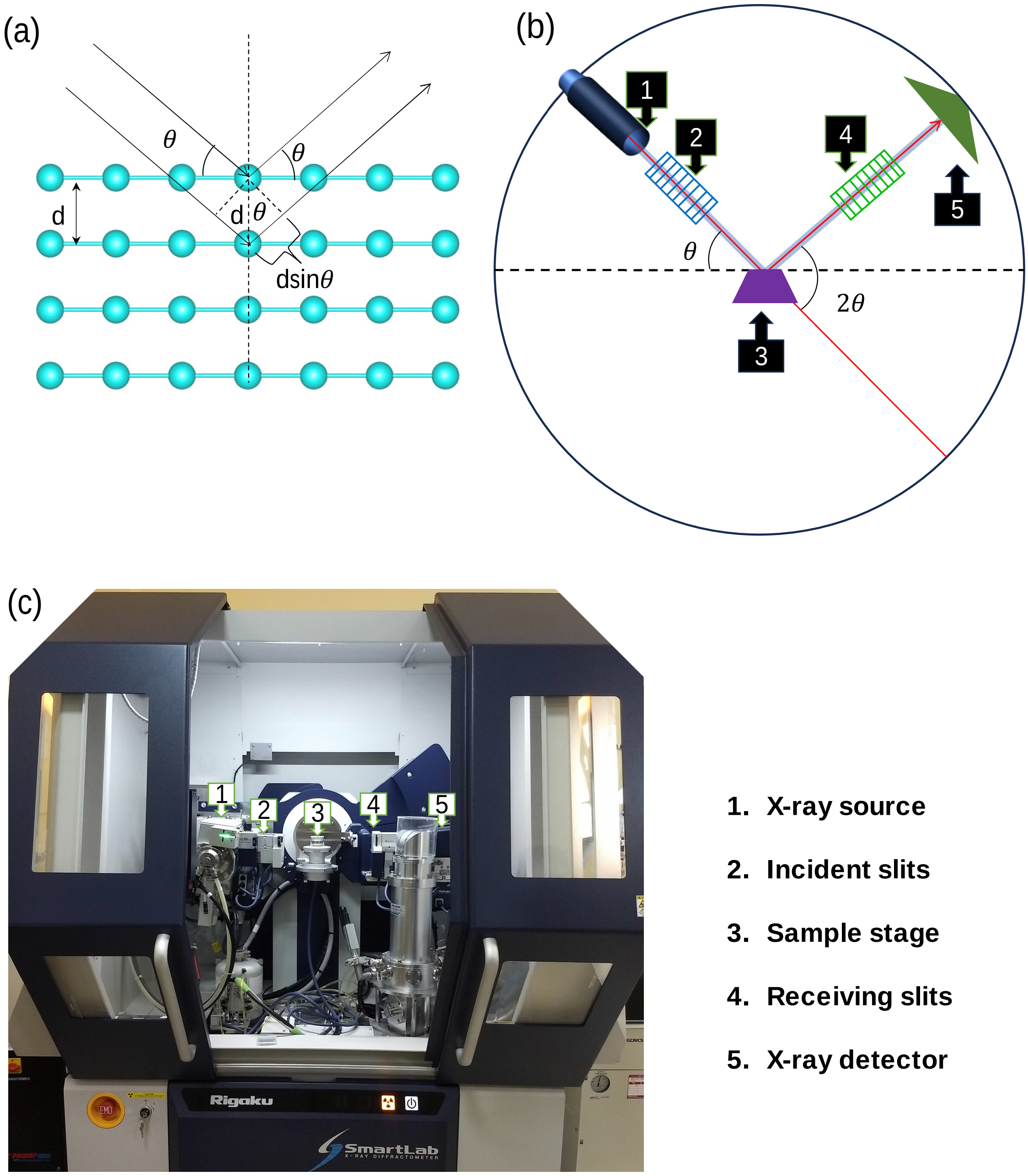

Figure 2.4: (a) X-ray diffraction from parallel Bragg planes. (b) Schematic diagram of X-ray diffractometer. (c) 9kW Rigaku-Smartlab XRD instrument at SNBNCBS.

The diffracted beam is recorded using a hybrid photon counting (HPC) detector. It's important to note that the mentioned diffractometer utilizes a $\theta - \theta$ goniometer setup, where the sample stage remains stationary while the X-ray tube and detector rotate to capture the XRD pattern. The angular positions of the X-ray tube and the detector are recorded as θ and θ, respectively. Alternatively, other XRD setups such as the Rigaku MiniFlex II employ a $\theta - 2\theta$ goniometer, where the X-ray tube is fixed at position and the detector is rotated by 2θ to record the data.

Rietveld refinement is an advanced analytical tool generally used on the X-ray diffraction (XRD) data to precisely analyze the crystal structure of materials. It employs a least-squares optimization approach to iteratively refine the parameters of the crystal structure model [87]. This method calculates the difference between the observed and calculated diffraction pattern, squares these differences, and then adjusts the model parameters to minimize their sum. During Rietveld refinement, various parameters are refined, such as atomic coordinates, thermal displacement parameters (B-factors), atomic occupancies, and lattice parameters. It also takes into account instrumental factors and sample characteristics by convoluting the calculated diffraction pattern with a profile function. This function describes the shape and broadening of diffraction peaks, considering the factors like instrumental resolution and sample microstructure. The calculated intensity in Rietveld refinement can be expressed using the following equation:

$$I_{\text{calc},i}(\theta) = F_i \cdot P_i(\theta) \cdot C(\theta) \cdot V \cdot R$$

Where:

- F_i is the structure factor for the i-th diffraction peak, representing the contribution of each atom in the crystal to the diffraction intensity.
- $P_i(\theta)$ is the profile function describing the instrumental broadening and sample characteristics at the given angle θ.
- $C(\theta)$ is the geometric correction factor, accounting for the variation in X-ray intensity with scattering angle θ.
- V is the the unit cell volume of the crystal.
- R is a scaling factor that accounts for the sample thickness, absorption, and instrumental efficiency.

The structure factor F_i depends on the atomic positions, atomic scattering factors, and other parameters describing the crystal structure. The profile function $P_i(\theta)$ characterizes the shape and broadening of the diffraction peak due to instrumental effects and sample properties. The geometric correction factor $C(\theta)$ adjusts for the variation in X-ray intensity with scattering angle.

2.3 Composition characterization: Energy Dispersive X-ray Spectroscopy (EDXS)

Energy Dispersive X-ray Spectroscopy (EDXS) also known as EDX, is a commonly employed to determine the elemental composition of the materials. In this technique, high energy electrons are bombarded to the sample.

When the sample is subjected to bombardment by a high-energy electron beam, the electrons bound within the inner shells of the atoms are excited. Consequently, vacancies are created in these inner shells. Electrons from the outer shells transit to fill these vacancies, emitting X-rays in the process. The energy of these emitted X-rays is equivalent to the energy difference between the two energy levels, which are defined by the principal quantum number n. The quantum numbers $n = 1, 2, 3$, and 4 are respectively represented by K, L, M, and N shells. A schematic diagram illustrating the process of generating different characteristic X-rays is shown in Fig. 2.5(a) . For instance, when an electron transitsfrom the L to the K shell, the emitted X-ray is designated as K_α. Similarly, when the transition occurs from the M to the K shell, the resultant X-ray is labeled as K_β. Analogously, transitions from the M and N shells to the L shell yield L_α and L_β X-rays, respectively. Since each element in the periodic table possesses a distinct atomic structure, the detection of characteristic X-rays emitted from a sample enables the identification of the elements present within it. In Fig. 2.5(c), a typical Energy Dispersive X-ray Spectroscopy (EDX) image is displayed, illustrating characteristic X-ray peaks such as K_α, K_β, L_α, and L_β corresponding to different elements within the sample (in this instance, Fe and Sn). The intensity of a specific X-ray peak is influenced by the likelihood of a particular electron transition. Generally, transitions from the L to K shell exhibit higher probabilities than those from the M to K shell. Consequently, K_α peaks tend to have higher intensities compared to K_β peaks for both Fe and Sn. For quantitative analysis, the background intensity [depicted by the black line in Fig. 2.5(b) EDX spectra] is initially subtracted from the acquired spectrum. Subsequently, the relative intensity of the peaks originating from various elements provides the weight percentage. The atomic percentage is then determined by dividing the corresponding atomic weight of each element.

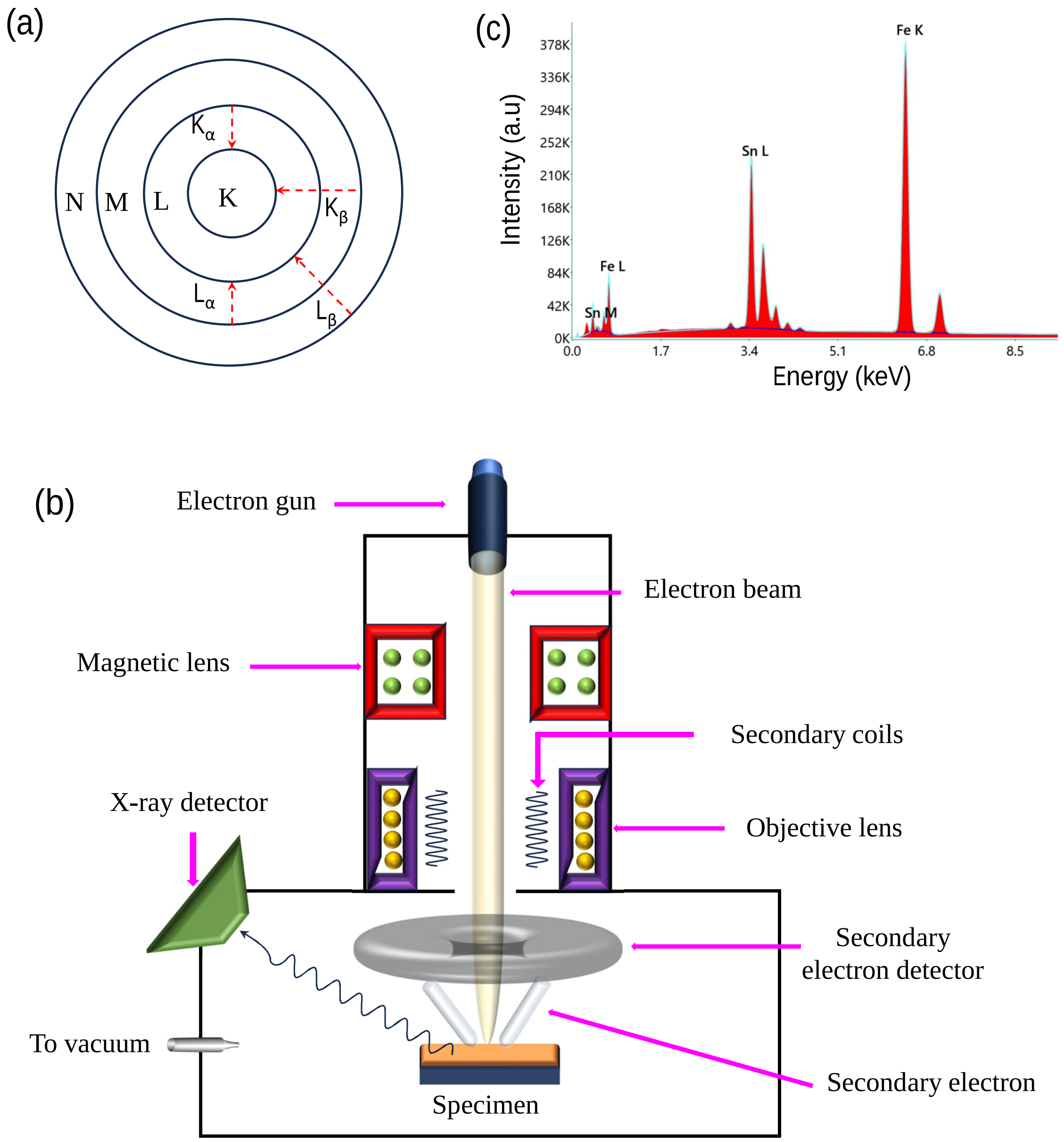

Figure 2.5: (a) Different energy levels of electrons and transition to lower energy levels generated K,L lines. (b) Schematic diagram of scanning electron microscope. (c) A typical EDXS spectrum containing characteristic X-rays emitted from elements.

2.4 Field Emission Scanning Electron Microscopy (FESEM)

: It is a powerful imaging technique used for high-resolution visualization of the surface morphology of materials at nanometer scales. It operates on the principle of scanning electron microscopy (SEM), where a focused beam of electrons is scanned over the surface of a sample, and the resulting signals are used to generate images with high spatial resolution. FESEM offers several advantages over conventional SEM, primarily due to its use of a field emission electron source. This source produces a highly focused electron beam with a smaller probe size and higher current density compared to conventional SEM, enabling enhanced imaging resolution and sensitivity to surface features. It provides exceptional imaging resolution, typically in the range of a few nanometers to sub-nanometer level. It is highly sensitive to surface features and can reveal surface morphology, texture, and composition with great precision. This technique also can detect the surface properties such as roughness, porosity, and surface defects. FESEM supports various imaging modes, including secondary electron (SE) imaging, backscattered electron (BSE) imaging, and energy-dispersive X-ray spectroscopy (EDS) for elemental analysis. Each imaging mode offers unique insights into sample characteristics and composition. Figure. 2.5(c) shows a schematic presentation of different components of FESEM instrument. First, the electron gun emits the high-energy electrons which are then primarily focused by the magnetic lenses and after fine tuning by the secondary coils and the objective lenses it falls on the surface of the specimen or sample. In thi way one can identify the surface morphology.

2.5 Magnetic Measurements

The magnetic measurements are carried out using the vibrating Sample Magnetometry (VSM). The VSM works on the method of varying magnetic field, while simultaniously detecting the magnetization response. Faraday's law states that a changing magnetic field induces an electromotive force (EMF) in a closed circuit. This induced EMF can result in the flow of electric current if the circuit is closed. In the context of VSM, when a varying magnetic field is applied to the sample, the magnetic moments within the sample respond by aligning themselves with the direction of the applied field. This alignment process involves changes in the magnetic flux passing through the sample. According to Faraday's law, this changing magnetic flux induces an EMF in the detection coil (pick-up coil) or sensor of the VSM system. If the magnetic flux passing through the coil is denoted as Φ_B, then the electromotive force (EMF), represented as ϵ, generated in the coil can be expressed as $\epsilon = -\frac{d\Phi_B}{dt}$. Here, $\frac{d\Phi_B}{dt}$ signifies the rate at which the magnetic flux changes with time. Following the Lenz's law, the direction of the induced current flow from the EMF is determined. As a result,

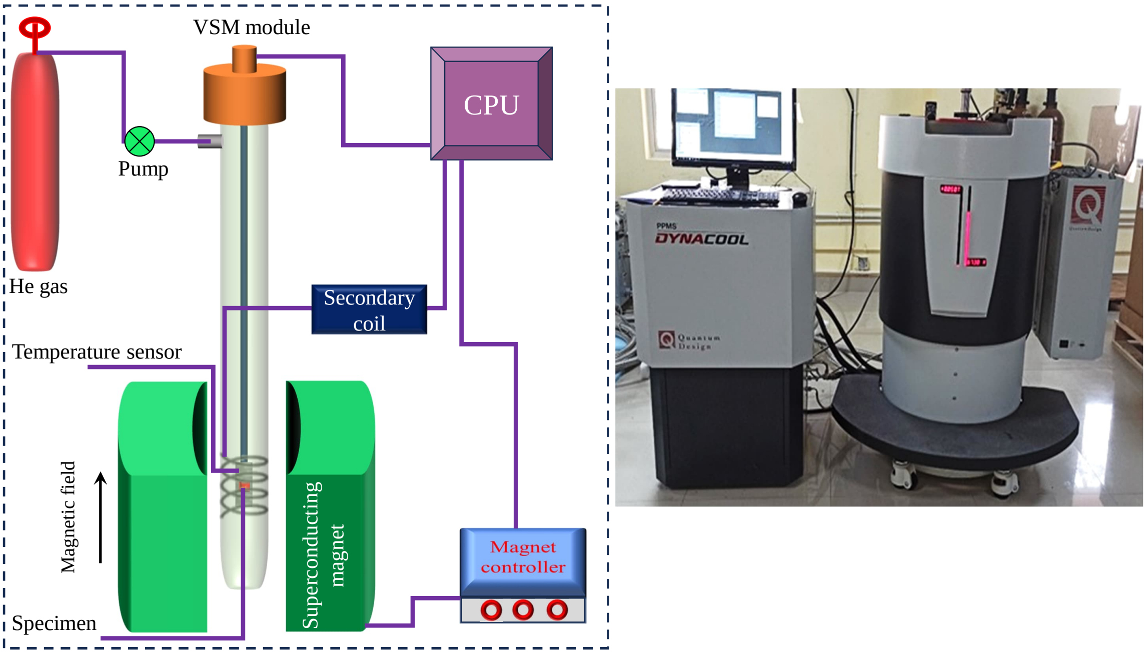

Figure 2.6: (Left) Schematic diagram of VSM instrument. (Right) Quantum Design (9T Dynacool) Physical properties measurement system (PPMS) at SNBNCBS

the induced current flows in such a direction that it produces a magnetic field opposing the varying applied magnetic field passing through the coil.

Various components of a VSM setup are illustrated in Fig. 2.6. The magnetic sample is fixed to a non-magnetic stick, which is connected to the vibration unit of the setup (VSM module). This stick is then inserted to a superconducting magnet where magnetic field is uniform. The external magnetic field somewhat aligns the magnetization along the field. As the sample oscillates up and down at high speed, the magnetic field generated by the magnetic moment of the sample changes with time. This alternating magnetic field from the sample induces an electric field in the pickup coils of the setup according to Faraday's law of induction. The voltage generated in the pickup coil, denoted as V_{coil}, can be expressed as $\frac{d\Phi_B}{dt}$. Expressed in terms of the vertical position of the sample (z), $\frac{d\Phi_B}{dt}$ can also be written as $\frac{d\Phi_B}{dz}\frac{dz}{dt}$. Consequently, for a sample oscillating sinusoidally at a frequency f and amplitude A, the induced voltage can be represented as $V_{\text{coil}} = 2\pi f C_m A \sin(2\pi f t)$, where C is the coupling constant, and m is the sample's magnetic moment intended to be measured. Thus, from the coil voltage, the sample magnetization at an applied magnetic field can be determined.

Our magnetization measurements were conducted using the VSM embedded in the Quantum Design Physical Property Measurement System (PPMS), where magnetic fields were varied up to 9 T across a temperature range from 2 K to 300 K. During the measurements, the sample underwent oscillation with a frequency of $f = 40$ Hz using the VSM linear motor. This vibration generated a voltage in the pickup coils. The setup is capable of detecting extremely low magnetic moments, down to the order of 10^{-6} emu. Moreover, the PPMS includes a VSM oven option, enabling VSM measurements to be conducted at elevated temperatures ranging from 400 K to 1000 K.

2.6 Electrical Transport Measurements

In metals or low band-gap semiconductors, the charge carriers freely move inside the system randomly in absence of any external force. Under the external force (electric or magnetic field) the charge carriers inside the materials will starts to follow in a specific path and encounter with several interactions such as electron-electron [88, 89], electron-phonon [90, 91], electron-spin [92], and electron-hole [93]. These low energy interactions influence the electrical resistivity. Therefore, the electrical resistivity measurement is an important tool of studying those interactions. There are mainly two methods exist to measure the electrical resistivity of a sample, (i) linear four-probe method, (ii) Van der Pauw method. For my transport measurements, I mainly used the linear four-probe technique

2.6.1 Linear four probe method

Linear four-probe technique is superior compared to the linear two-probe technique as the former minimizes the contact resistances in a much better way. The outer probes inject a known current into the material, while the inner probes measure the voltage. This configuration ensures that the voltage drop across the contacts does not affect the accuracy of the resistivity measurement. The four-probe setup eliminates the effects of lead resistance, which can distort measurements in traditional two-probe methods. Lead resistance refers to the resistance of the wires connecting the probes to the measurement instruments. Figure 2.7 represents the four-probe measurement set-up.

The four-probe measurement set-up has different components necessary to build temperature dependent resistivity measurement equipment.

(i) **Sample preparation**: First, we need to make the four-probe connections to the sample. Cu-wires (25-75 μm diameter) are generally used to make the contacts to the sample. The Cu-wires are attached using Epo-Tek H20E silver-epoxy where the resin and the hardener are mixed with 1:1 weight ratio. The mixture along with the contacts are cured by warming it at 80^0C inside the glove-box to avoid any oxidization. Then, the sample was

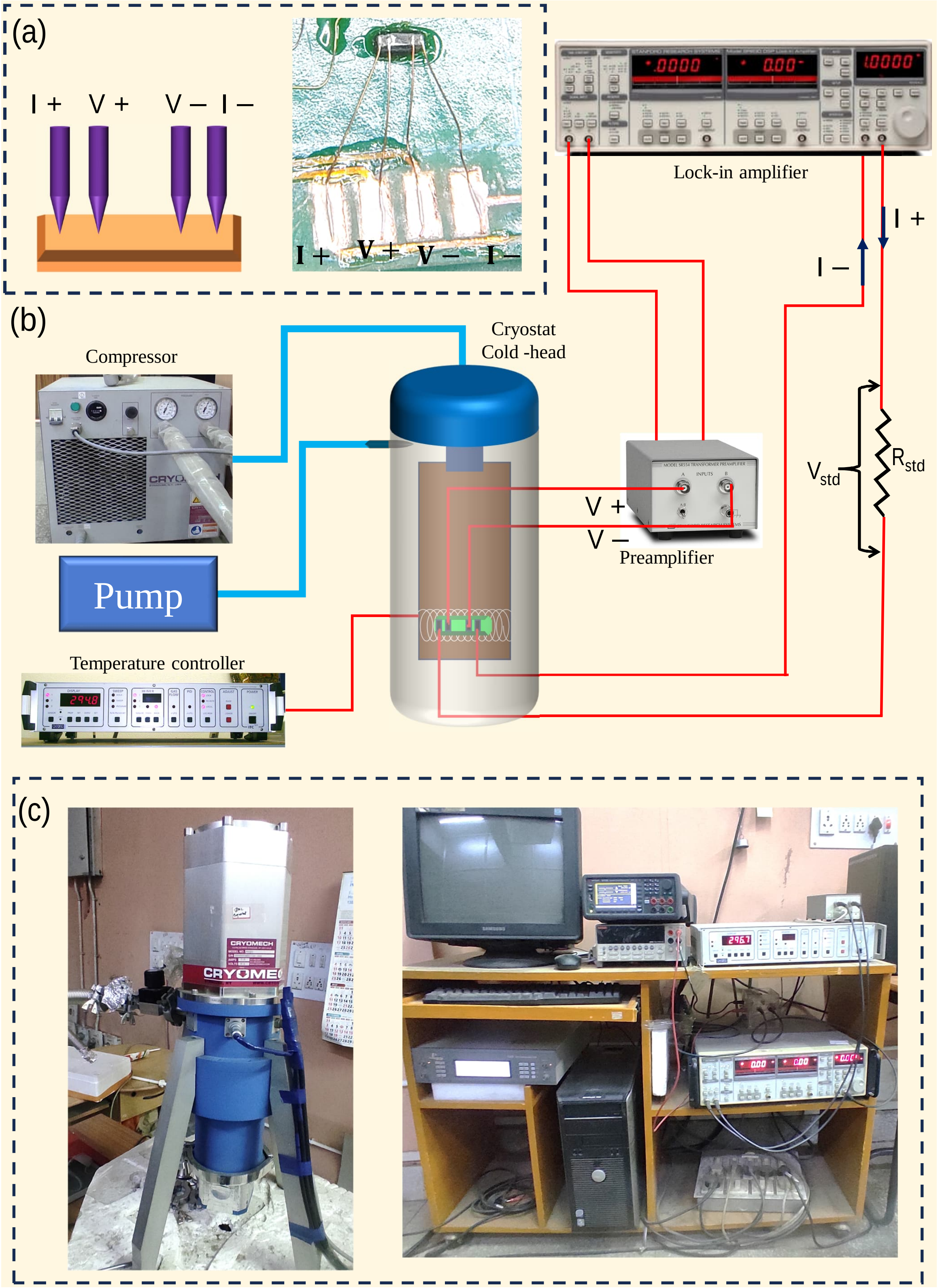

Figure 2.7: (a) Left image shows schematic presentation of four-probe connections and Right image shows four-probe connections in real material. (b) Schematic image of a temperature dependent resistivity set-up. (c) Temperature dependent resistivity set-up at our Lab.

mounted on the cryostat bar using Apiezon N Grease which is a electrical insulator but very good thermal conductor to make the sample thermally connected to the cryostat.
(ii) **Cryostat and Temperature controller**: Next to vary the sample temperature, the cryostat was kept under vacuum using Pfeiffer turbo pump and the the Cryomech compressor was used to lower the cryostat temperature to 3.5 K. Then an ITC 503 Proportional–integral–derivative (PID) controller was used to sweep the temperature.
(iii) **Lock-in amplifier**: Usually, in metallic samples the resistance is very low ($\sim \mu\Omega - m\Omega$ range). So its very hard to use conventional method where we can pass a current and measure the voltage drop against the probes and from then we can calculate the resistance. For instance, if we pass few mA current then the voltage drop will be (μV-nV range) which is in the resolution range of usual volt-meter. Here, we use Lock-in amplifier which amplifies the signal and reduces any other noise signals. A lock-in amplifier uses the phase sensitive detection (PSD) technique. First, the lock-in amplifier modulates the input signal of interest with a reference signal. This modulation is typically achieved by multiplying the input signal with a sinusoidal reference signal at a specific frequency, known as the reference frequency. Consider the voltage of the sample is $V_{sample} = V_s sin(\omega_s t + \phi_s)$ and the reference signal is $V_{ref} = V_r sin(\omega_r t + \phi_r)$. After multiplying these two voltages we get

$$\begin{aligned} V_{PSD} &= V_s V_r sin(\omega_s t + \phi_s) sin(\omega_r t + \phi_r) \\ &= \frac{1}{2} V_s V_r cos[(\omega_s - \omega_r)t + \phi_s - \phi_r] - \frac{1}{2} V_s V_r cos[(\omega_s + \omega_r)t + \phi_s + \phi_r] \end{aligned} \tag{2.6.1}$$

If we choose $\omega_s = \omega_r$ then the above output becomes

$$V_{PSD} = \frac{1}{2} V_s V_r cos[\phi_s - \phi_r] - \frac{1}{2} V_s V_r cos[2\omega_s t + \phi_s + \phi_r] \tag{2.6.2}$$

If this output is passes through a low-pass filter, then we are left with $V_{PSD} = \frac{1}{2} V_s V_r cos[\phi_s - \phi_r]$, which is a dc signal. So, by using this mechanism we can clearly get the voltage while the noise signals is filtered out. By changing the reference signal amplitude, we can amplify the voltage signals.

As for the resistivity data acquisition, first an ac-voltage is passes through a known standard resistance (R_{std}) substance followed by the sample. The current flowing through the sample can be calculated as $I = \frac{V_{std}}{R_{std}}$ where V_{std} is voltage drop across the standard resistance measured using Keithly 2000 digital multimeter (DMM). The samples voltage first passes through a transformer-based pre-amplifier (Standford Research Systems 554 pre-amplifier) where the noise signals are filtered out and the voltage signal is amplified significantly (100 times) then enter into the lock-in amplifier (Standford Research Systems 830

DSP Lock-in), where the voltage (V_s) is measured. Thus, the resistance of the sample would be $R_{sample} = \frac{V_s}{V_{std}}\frac{R_{std}}{100}$. The resistivity is calculated by $\rho = \frac{R_{sample}A}{L}$. Here, A is crossectional area and L is the length between the voltage probes of the sample. The automation of the instruments and the data acquisition is done using the LabVIEW programming and General Purpose Interface Bus (GPIB) connections.

2.6.2 Magneto-transport Measurements

In the previous section we have mentioned about how the resistivity of a sample is measured by varying the temperature alone. Here, using Quantum Design physical properties measurement system (PPMS 9T), along with temperature we can also vary the magnetic field, thus called as magneto-transport measurements. Magneto-transport measurements are usually performed to identify the magnetoresistance (MR) and Hall effect properties.

Figure 2.8(a) depicts the schematic representation of different parts of a magneto-transport set-up. To achieve high magnetic fields, the electromagnets made out of superconducting wires is a good choice as the superconductor below the superconducting transition temperature does not dissipate any heat. In PPMS, Niobium-Titanium (Nb-Ti) alloys is used for the superconducting magnet, its superconducting temperature is about 10K [94]. The superconducting magnet is kept inside the chamber is cooled down to 4.2 K using a CryoMech Helium compressor. The sample is mounted on the puck which is attached to a rotator. The magnetic field strength is varied using a current controller and all this attachment is connected to a CPU. As for the measurement the resistivity is measured using ac current signal applied to the sample as discussed in the previous section. For magnetoresistance we use linear four-probe connection, while for Hall measurement, we use transverse connection such that the voltage terminal are always perpendicular to the current terminals and the field will always be perpendicular to both current and voltage terminals as shown if Fig2.9

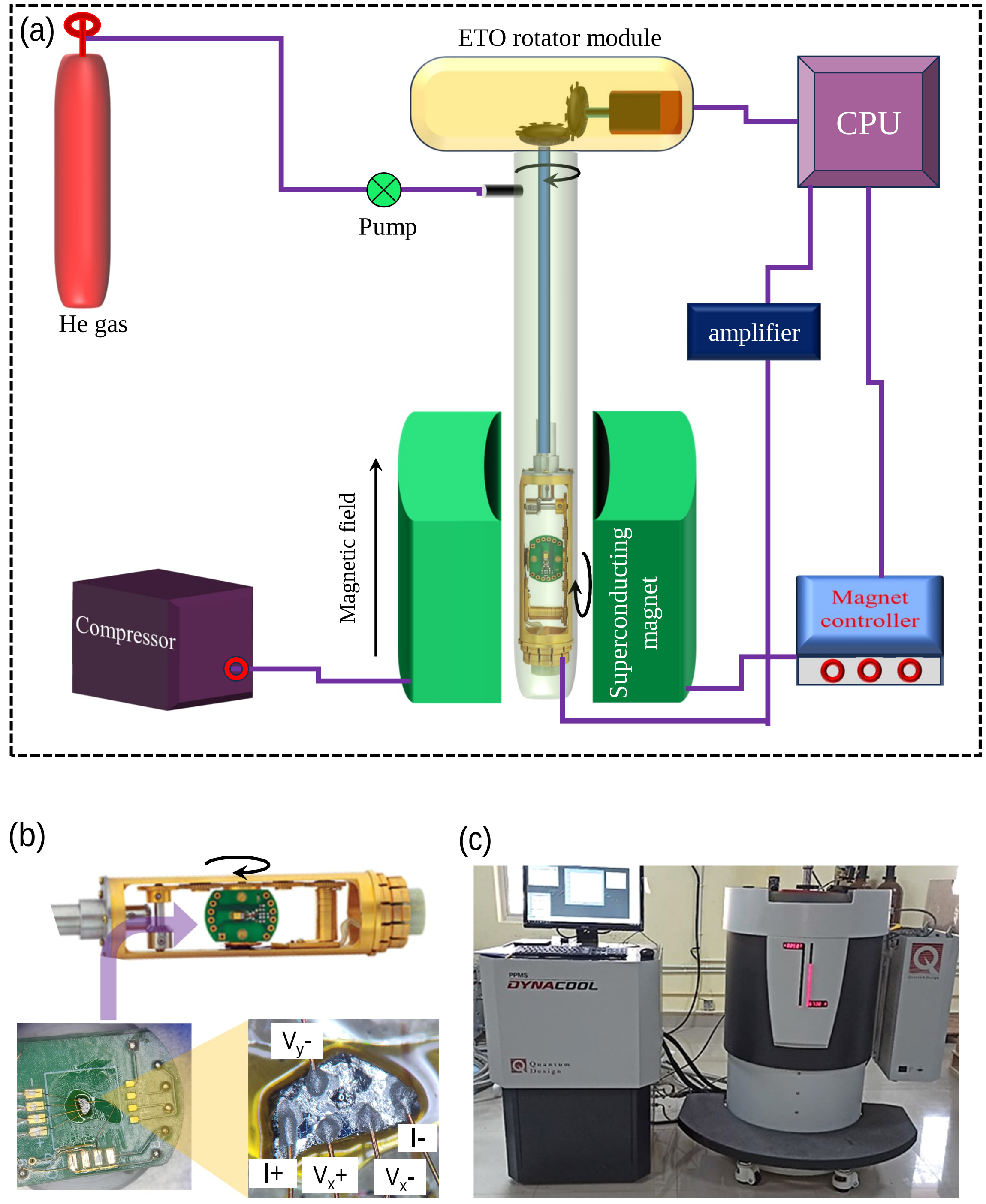

Figure 2.8: (a) Schematic diagram of magneto-transport set up. (b) Rotator stick and rotator puck and sample mounted on the puck. (c) Quantum Design physical properties measurement systems (PPMS 9T) at SNBNCBS.

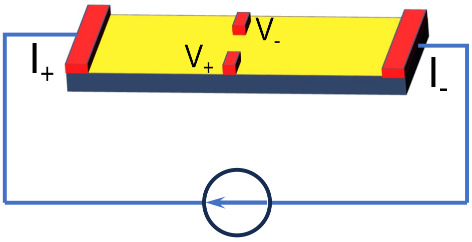

Figure 2.9: Schematic of Hall probe geometry

Chapter 3

Topological Hall Effect Instigated in Kagome Antiferromagnet $Mn_{3-x}Sn$ due to Mn-deficient Induced Noncoplanar Spin Structure

3.1 Introduction

Hall effect is one of the pioneering discoveries in condensed matter physics [95], gained a lot of attentiveness both from the fundamental and technological applications [96, 97]. Specifically, in the fundamental science, the Hall effect branched into various exotic phenomena such as the spin Hall effect (SHE) [98], the quantum Hall effect (QHE) [99–101], the anomalous Hall effect (AHE) [35], and the recently emerging topological Hall effect in helimagnets. Particularly, the topological Hall effect is a direct manifestation of real-space Berry phase acquired by the conduction electrons moving around the topologically stable knots, also called the skyrmions, in chiral spin structures [39, 102, 103]. Topological spin structures in helimagnets are driven by the geometrical frustration in triangular lattice or Dzyaloshinskii-Moriya interaction (DMI) in the absence of centrosymmetry of the crystal [32, 104–108]. There exists several geometrically frustrated Kagome systems such as $Co_3Sn_2S_2$ [77, 109], Fe_3Sn_2 [110], $EuCd_2As_2$ [111] and non-centrosymmetric crystals such as the cubic B20 chiral magnets MnSi [40], FeGe [112], MnGe [113], Cu_2OSeO_3 [114], and Mn_2RhSn [115] showing topological Hall effect. Importantly, most of these magnetic topological systems show THE besides the magnetization driven anomalous Hall effect hindering the potential applications of THE in the topological electronics [49, 116, 117]. Thus, finding materials merely with topological Hall effect is desirable for the technological applications.

In this letter, we report on the topological Hall effect of $Mn_{3-x}Fe_xSn$ (x=0, 0.2, 0.25, and 0.35) single crystals. Our studies show a large and pure room-temperature topological Hall effect with topological Hall resistivity $\rho^T_{xy} \approx 2\ \mu\Omega$-cm in Mn_3Sn at a low critical field of 0.3 T. To our knowledge, no other system shows such a pure and large THE signal at room temperature in its bulk form except Gd_2PdSi_3 which shows THE, with negligible AHE signal, but only at very low temperatures (< 25K) [48]. The value of ρ^T_{xy} increases further

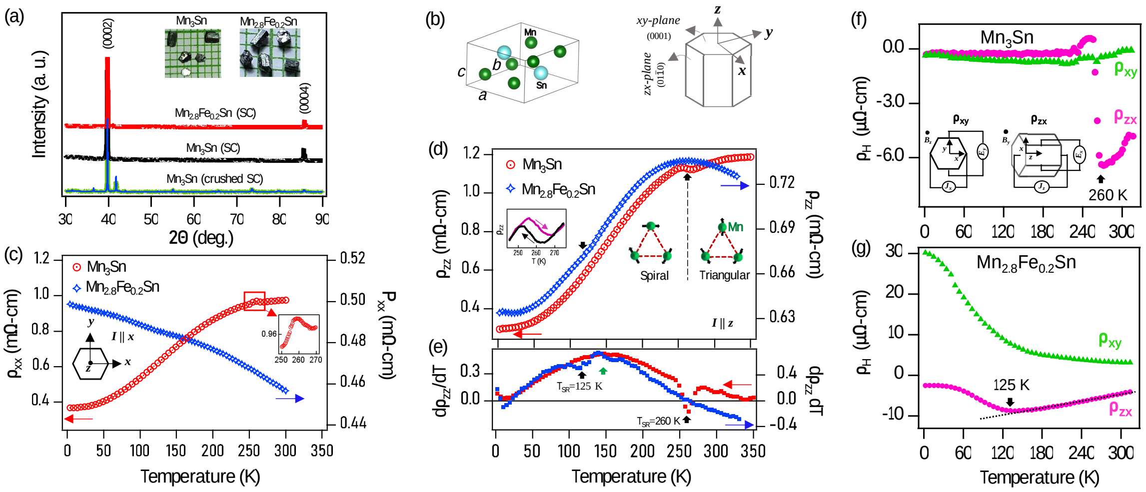

Figure 3.1: (a) Powder XRD data from crushed single crystals of Mn_3Sn, single crystal of Mn_3Sn, and $Mn_{2.8}Fe_{0.2}Sn$. Inset in (a) shows photographic image of Mn_3Sn and $Mn_{2.8}Fe_{0.2}Sn$ single crystals. Left-panel in (b) shows primitive unit cell of the hexagonal crystal structure of Mn_3Sn and the right-panel in (b) defines the crystal planes, zx-plane $(01\bar{1}0)$ and xy-plane (0001) on the hexagonal unit cell. (c) Resistivity measured along the a-axis, ρ_{xx}, as a function of temperature is plotted for both Mn_3Sn and $Mn_{2.8}Fe_{0.2}Sn$. (d) Resistivity measured along the c-axis, ρ_{zz}, as a function of temperature is plotted for both Mn_3Sn and $Mn_{2.8}Fe_{0.2}Sn$. Right-side inset in (d) shows schematic representation of the spin-reorientation above and below the transition temperature of 260 K for Mn_3Sn and 125 K for $Mn_{2.8}Fe_{0.2}Sn$. Left-side inset in (d) shows thermal hysteresis of the resistivity, ρ_{zz} (T), between heating and cooling cycles of data collection on Mn_3Sn. (e) First derivative of ρ_{zz} with respect to the temperature. (f) xy-plane (ρ_{xy}) and zx-plane (ρ_{zx}) Hall resistivity measured as a function of temperature from Mn_3Sn with a magnetic field of 1T applied parallel and perpendicular to the c-axis. Schematics in (f) show the measuring geometries used for recording the data of ρ_{xy} and ρ_{zx}. (g) Similar data of (f) but measured from $Mn_{2.8}Fe_{0.2}Sn$.

to 2.3 $\mu\Omega$-cm with decreasing temperature down to 260 K, but abruptly disappears below 260 K due to magnetic reorientation from coplanar AFM to spin-spiral structure [41, 118]. We uncover highly anisotropic topological properties of these systems at room temperature. That means, anomalous Hall effect (AHE) has been noticed in the zx-plane, while the topological Hall effect has been noticed in xy-plane. Moreover, the room-temperature THE decreases with increasing Fe doping and it is almost suppressed by the Fe doping of x=0.35. Additionally, low temperature topological properties emerge by Fe doping. In the below, we explore in detail our experimental findings.

3.2 Experimental details

For the growth of Fe doped single crystals, we followed the same method by adding the desired amount of iron powder (Alfa Aesar, 99.99%) to the Mn-Sn mixture. In this way, we obtained several shiny hexagonal-rod-shaped single crystals with typical dimensions of $2 \times 1 \times 1$ mm^3. Powder X-ray diffraction (XRD) was performed using Rigaku SmartLab 9kW Cu K$_\alpha$ X-ray source. Stoichiometry of the crystals were found to be $Mn_{2.95(1)}Sn_{1.05(1)}$ and $Mn_{2.76(1)}Fe_{0.21(1)}Sn_{1.03(1)}$ using Energy Dispersive X-ray Spectroscopy (EDXS). From the EDXS data, we can observe that both compounds have marginally higher Sn concentrations. For simplicity, we denote the compositions as Mn_3Sn and $Mn_{2.8}Fe_{0.2}Sn$. Electrical transport and Hall effect measurements were performed using the four-probe technique. Copper leads were attached to the sample using EPO-TEK H21D silver epoxy. Temperature-dependent resistivity data were recorded from physical properties measurement system (PPMS, Dynacool, Quantum Design) within the temperature range of 2-350 K. Hall measurements were done by sweeping the magnetic fields between -4 T and 4 T. Magnetic properties studies were done using the vibrating sample magnetometer (VSM) option of PPMS (Dynacool, Quantum Design) within the temperature range of 2-350 K and magnetic field was varied between -4 T and 4 T.

The powder XRD pattern of the crushed single crystals shown in the bottom panel of Figure3.1(a) in the main text confirms that Mn_3Sn crystalizes into hexagonal phase with a space group of $P6_3/mmc$ (194). No impurity peaks have been detected from the XRD pattern, which suggests pure-phase Mn_3Sn single crystals. From the XRD pattern refinement of Mn_3Sn we obtain lattice parameters a=b= 5.679(2) and c=4.533(4) which are comparable to the reported values of Mn_3Sn [118, 119]. The XRD patterns have taken on the single crystals of Mn_3Sn and $Mn_{2.8}Fe_{0.2}Sn$ show multiple reflections corresponding to (0002) and (0004) planes.

3.3 Results and Discussions

Electrical resistivity measured along the *a*-axis (ρ_{xx}) plotted as a function of temperature in Fig. 3.1(c) for both Mn_3Sn and $Mn_{2.8}Fe_{0.2}Sn$. From Fig. 3.1(c) we can observe that the ρ_{xx} resistivity of the parent compound shows a metallic nature, and interestingly for the first time, we find a hump-like structure at around 260 K [shown in the inset of Fig. 3.1 (c)], whereas, in the case of Fe doped $Mn_{2.8}Fe_{0.2}Sn$, the resistivity decreases with increasing temperature which is a kind of bad-metallic behaviour [120]. Similarly, electrical resistivity measured along the *c*-axis (ρ_{zz}) plotted as a function of temperature in Fig. 3.1(d) for both Mn_3Sn and $Mn_{2.8}Fe_{0.2}Sn$. As can be seen from the ρ_{zz} resistivity data, both parent and Fe doped systems show metallic behavior at low temperatures except for a significant increase in the impurity resistivity from 0.3 mΩ-cm to 0.63 mΩ-cm with Fe doping. Further, we observe a *kink* at around 260 K in Mn_3Sn which has been ascribed earlier to the spin structure reorientation of Mn atoms from a high-temperature noncollinear inverse triangular structure to a low-temperature noncoplanar spiral structure [41, 118]. But with Fe doping, we find that the spin reorientation transition temperature decreased to 125 K at which the *kink* has been observed from the ρ_{zz} resistivity of $Mn_{2.8}Fe_{0.2}Sn$ as shown in Fig. 3.1 (d). Inset in Fig. 3.1 (d) shows thermal hysteresis in the ρ_{zz} resistivity of Mn_3Sn taken around 260 K between heating and cooling cycles. Thermal hysteresis in the ρ_{zz} resistivity is consistent with the previous report on Mn_3Sn except that it was found at 270 K [41] and 275 K [118]. Such a thermal hysteresis is attributed to the first-order type magnetic transition from triangular to spiral structure in this system [118]. On the other hand, we do not observe such a thermal hysteresis in the ρ_{zz} resistivity of $Mn_{2.8}Fe_{0.2}Sn$ despite having the magnetic transition at around 125 K.

To pinpoint the spin-reorientation transition temperature (T_{SR}), we plotted $d\rho_{zz}/dT$ as a function of temperature as shown in Fig. 3.1 (e). From the first derivative, we can reaffirm T_{SR}=260 K for Mn_3Sn and 125 K for $Mn_{2.8}Fe_{0.2}Sn$. In addition, we also observe a decrease in $d\rho_{zz}/dT$ with increasing T for both systems below 10 K possibly due to weak local potentials at low temperatures [121] and above 143 K due to an electronic phase transition. Eventually, $d\rho_{zz}/dT$ becomes zero at 265 K and beyond this temperature, it is negative for $Mn_{2.8}Fe_{0.2}Sn$. That means, $Mn_{2.8}Fe_{0.2}Sn$ shows a metal-insulator (MI) transition at around 265 K. On the other hand, in Mn_3Sn, the MI transition seems to be happening at much-elevated temperatures as $d\rho_{zz}/dT$ approaches zero at around 345 K [122]. To emphasize here, Mn_3Sn shows nearly isotropic resistivity between *a* and *c* axes, while $Mn_{2.8}Fe_{0.2}Sn$ shows a large resistivity anisotropy.

Fig. 3.1(f) depicts Hall resistivity in the *xy*-plane (ρ_{xy}) and in the *zx*-plane (ρ_{zx}) plotted

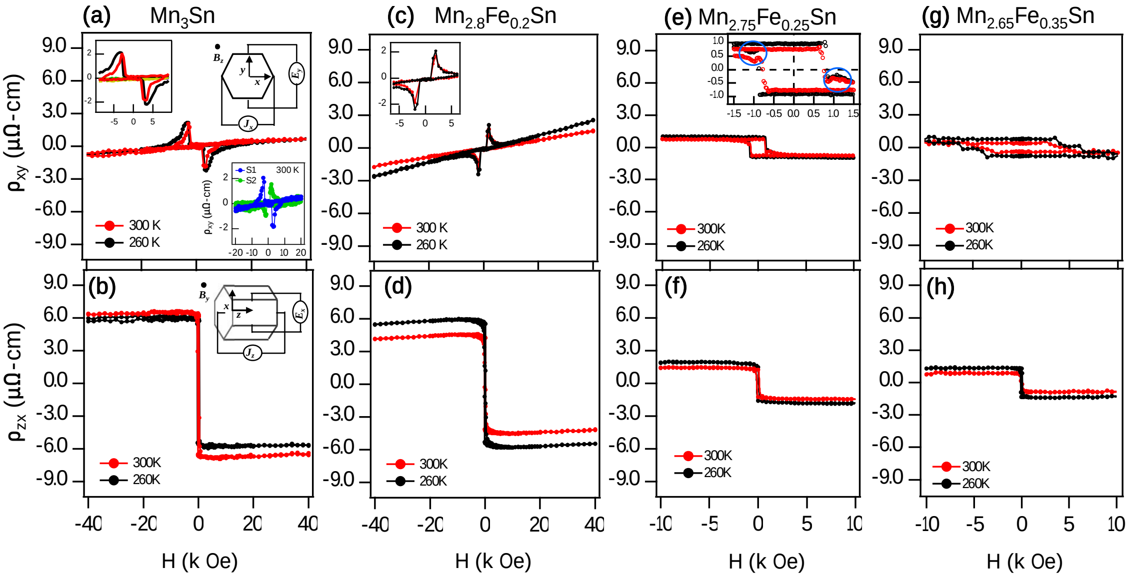

Figure 3.2: (a) xy-plane (ρ_{xy}) Hall resistivity plotted as a function of the magnetic field from Mn$_3$Sn. The measuring geometry is shown in the top-right inset of (a) and zoomed-in data at low magnetic fields are shown in the top-left inset of (a). Bottom-right inset in (a) shows the Hall resistance (raw data) measured on two different samples (S1 and S2) of Mn$_3$Sn at 300K. (b) zx-plane (ρ_{zx}) Hall resistivity plotted as a function of the magnetic field from Mn$_3$Sn. The measuring geometry is shown in the top-right inset of (b). (c) and (d), (e) and (f), and (g) and (h) are similar Hall resistivity data of (a) and (b) but measured from Mn$_{2.8}$Fe$_{0.2}$Sn, Mn$_{2.75}$Fe$_{0.25}$Sn, and Mn$_{2.65}$Fe$_{0.35}$Sn, respectively.

as a function of temperature from Mn$_3$Sn measured with a magnetic field of 1 T applied parallel and perpendicular to the c-axis. From Fig. 3.1(f), we notice an increase in ρ_{zx} from 320 K down to 260 K, which then instantaneously become nearly zero below 260 K. This sudden decrease in ρ_{zx} at 260 K coincides with the spin-reorientation transition temperature of the studied sample. The observation of drastic changes in the ρ_{zx} Hall resistivity at 260 K is in good agreement with previous studies on a similar system except for a slightly higher transition temperature of 270 K [41] and 275 K [118]. On the other hand, we observe no significant change in ρ_{xy} from 320 K down to 2 K, which is nearly zero all the time. Next, Fig. 3.1(g) depicts ρ_{xy} and ρ_{zx} Hall resistivity plotted as a function of temperature for Mn$_{2.8}$Fe$_{0.2}$Sn measured with magnetic field of 1 T applied parallel and perpendicular to the c-axis. From Fig. 3.1(g), we notice an increase in ρ_{zx} from 320 K down to 125 K, which gradually decreases with temperature from 125 K down to 40 K, and then saturates below 40 K. The decrease in ρ_{zx} coincides with the spin-reorientation transition temperature of 125 K as observed from the magnetization measurements on the doped sample [see Fig. 3.3(b)]. On the other hand, ρ_{xy} slowly increases from 320 K down to 125 K and exponentially increases from 125 K down to 40 K, and then tends to saturate below 40 K. Interestingly, we notice an extremely large ρ_{xy} value of 31 $\mu\Omega - cm$ with 1 T field at 2 K which is negligible in Mn$_3$Sn.

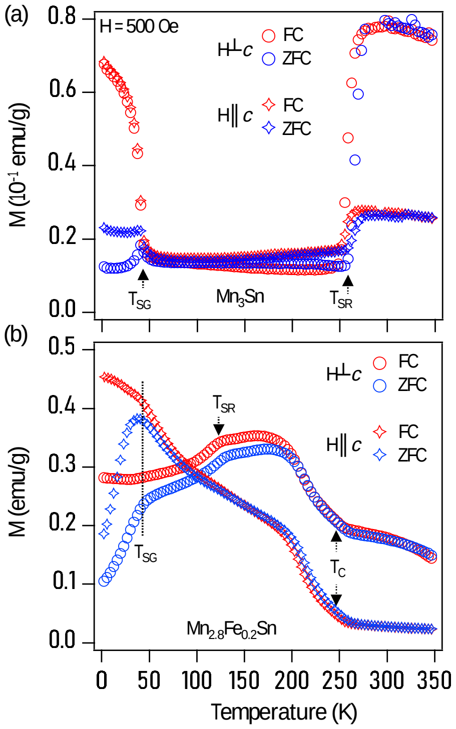

Figure 3.3: Magnetization as a function of temperature, M(T), plotted for Mn_3Sn (a) and $Mn_{2.8}Fe_{0.2}Sn$ (b). In figures, T_{SR} is spin reorientation transition temperature, T_{SG} is spin-glass transition temperature, and T_C is Curie-Weiss temperature. The data is collected with an external magnetic field of 500 Oe applied both in parallel and perpendicular to the *c*-axis.

Magnetization as a function of temperature M(T), plotted for zero-field cooling (ZFC) and field cooling (FC) modes with an external magnetic field of 500 Oe applied parallel and perpendicular to *c*-axis is shown in Fig. 3.3(a) for Mn_3Sn and in Fig. 3.3(b) for $Mn_{2.8}Fe_{0.2}Sn$. When the field is applied perpendicular to *c*-axis ($H \perp c$), in Mn_3Sn, a huge drop in magnetization is noticed at 260 K for both FC and ZFC modes, while the magnetization drop still present for the field applied parallel to *c*-axis ($H \parallel c$) but relatively small compared to $H \perp c$. The magnetization drop at 260 K for $H \perp c$ can be understood as a result of spin-reorientation from inverse-triangular to spin-spiral structure [32,106–108,123,124]. Further reduction in temperature leads to spin-glass transition at 40 K as we find a cusp-like splitting in the magnetization curve between ZFC and FC modes as shown in Fig. 3.3(a). Quantitative comparison of our Mn_3Sn magnetization data with the existing literature is quite challenging as the magnetic properties of this system are highly sensitive to the growth conditions and the chemical compositions [125]. However, the spin-reorientation and spin-glass transitions are inline with the previous reports [32, 106–108].

For a better understanding of the magnetism of these systems, we performed isothermal magnetization M(H) measurements as shown in figure 3.4. Figs. 3.4 (a) and 3.4 (b) depict M(H) isotherms from Mn_3Sn for $H \| c$ and $H \perp c$, respectively. From Fig. 3.4 (a), we see significant magnetic hysteresis in Mn_3Sn for $H \| c$ at 2 K without saturation even at an applied

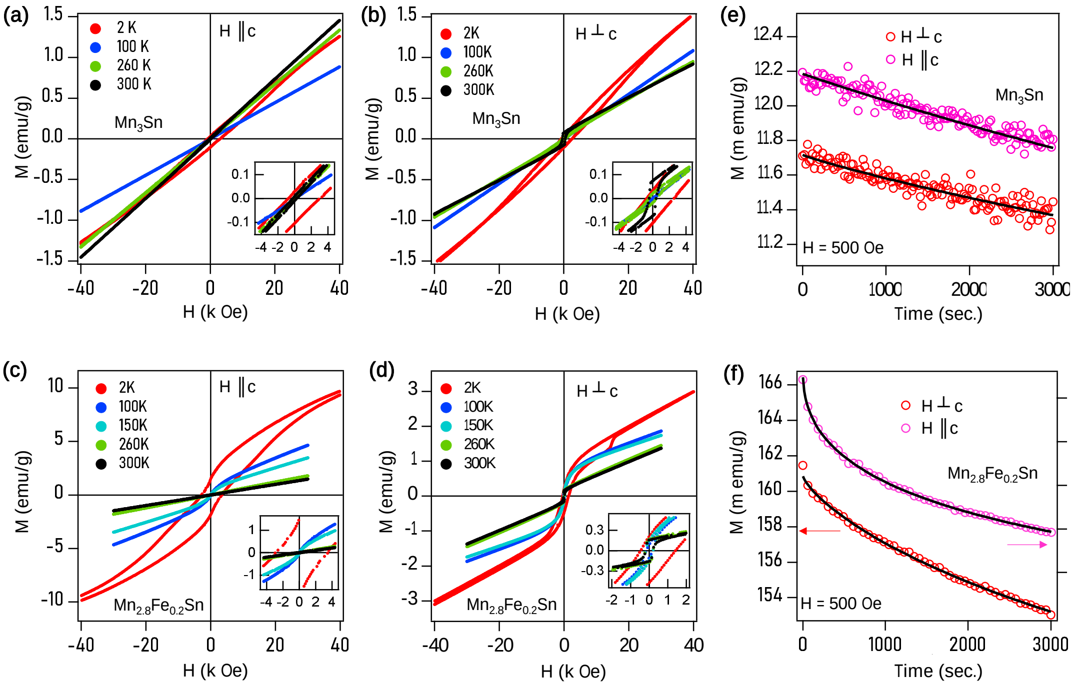

Figure 3.4: Magnetization isotherms, M(H), of Mn_3Sn for field applied parallel (a) and perpendicular (b) to the *c*-axis measured at various temperatures. Similarly, magnetization isotherms of $Mn_{2.8}Fe_{0.2}Sn$ for field applied parallel (c) and perpendicular (d) to the *c*-axis measured at various temperatures. (e) and (f) show magnetization relaxation data plotted as a function of time, measured at 5 K with an external field of 500 Oe applied parallel and perpendicular to the *c*-axis from Mn_3Sn and $Mn_{2.8}Fe_{0.2}Sn$, respectively.

field of 4 T. But at higher temperatures, the magnetic hysteresis disappears. The observed magnetic hysteresis at 2 K is possibly due to short-range magnetic ordering due to spin fluctuations in the spin-glass state. As shown in Fig. 3.4 (b), for $H \perp c$ also the isotherms M(H) are found to be similar to $H \| c$ with significant magnetic hysteresis at 2 K again due to glassy spin nature. In contrast, we find a weak ferromagnetic-like hysteresis with large coercivity and remanence at 300 K. Moreover, the slope dM/dH obtained at higher fields ($>$ 3 T) decreases with increasing temperature, hinting at reduced antiferromagnetism in Mn_3Sn at higher temperatures. Therefore, we conclude that the observed magnetic hysteresis at low temperatures for both $H \perp c$ and $H \| c$ in Mn_3Sn is due to the short-range magnetic interactions below $<$ 40 K. The anisotropic magnetization between $H \perp c$ and $H \| c$ in Mn_3Sn is in good agreement with previous magnetic studies on Mn_3Sn [119].

Figures 3.4(c) and 3.4(d) depict M(H) isotherms measured on $Mn_{2.8}Fe_{0.2}Sn$ at various temperatures for both $H \| c$ and $H \perp c$, respectively. From Fig. 3.4(c), for $H \| c$, we can see that the Fe doping induces a long-range ferromagnetic ordering as the magnetic hysteresis is found with increased coercivity at 2 K. But the magnetic hysteresis disappears at temperatures of 100 and 150 K, while still having a sigmoid-like M(H) curve. On the other hand, at the temperatures of 260 and 300 K, we observe that the system completely transforms into antiferromagnet as we find linear M(H) isotherms. Next from Fig. 3.4(d), for H$\perp c$, we observe M(H) isotherm with a coercivity of 850 Oe at 2 K. Interestingly, we also notice a field-induced asymmetric M(H) curve at 2 K that is not visible for H$||c$. We further observe reduced coercivity of 220 Oe at 260 K, which is nearly constant up to 300 K without any field-induced asymmetry in the M(H) loop. Note here that the coercivity of $Mn_{2.8}Fe_{0.2}Sn$ is almost a factor of 2 less compared to the parent system for H$\perp c$ at 300 K. Whereas, the coercivity of $Mn_{2.8}Fe_{0.2}Sn$ is nearly 2 times higher compared to Mn_3Sn at 2 K for H$||c$.

The glassy-spin nature of the systems is further examined by performing magnetization relaxation measurements for both Mn_3Sn and $Mn_{2.8}Fe_{0.2}Sn$ as shown in Figs. 3.4(e) and 3.4(f), respectively, measured with an applied magnetic field of 500 Oe in the FC mode at 5 K. Magnetization relaxation for a spin-glass system can be explained using the Stretched function, $M(t) = A\ exp[-(\frac{t}{\tau})^{\alpha}]$ [126]. Here, A is an exponential factor, t is the time, τ is a characteristic relaxation time constant, and α is stretching exponent which is temperature dependent and can take the values $0 < \alpha < 1$ [127]. From the Stretched function fitting to Mn_3Sn [see Fig. 3.4(e)], we obtain α=0.96$\pm$0.04 and τ=(1.03$\pm$0.17)10^5 s for H$||c$. Similarly, α=0.85$\pm$0.1 and τ=(1.83$\pm$0.77)10^5 s are obtained for H$\perp c$. The α values close to 1 and higher relaxation time constants suggest Mn_3Sn to be nearly an isotropic spin-glass system. On the other hand, the best fit for the magnetization relaxation curves from $Mn_{2.8}Fe_{0.2}Sn$ is obtained using the modified Stretched function $M(t) = M_0 + A\ exp[-(\frac{t}{\tau})^{\alpha}]$ [43, 128, 129]. Here, the additional term M_0 is the magnetization due to long-range ferromagnetic ordering at t=∞ [130]. From the fitting [see Fig. 3.4(f)] we obtained M_0= 0.21$\pm$0.1 emu/g, τ=5672$\pm$512 s and α=0.47$\pm$0.01 for H$||c$. Similarly, we obtained M_0= 0.14$\pm$0.01 emu/g, τ=7316.8 $\pm$ 31.9 s and α=0.76$\pm$0.02 for H$\perp c$. Here, different α values (<1) for different crystal orientations found in $Mn_{2.8}Fe_{0.2}Sn$ suggest for anisotropic ferromagnetism induced with Fe doping, which is consistent with the anisotropic magnetization isotherms, M (H), shown in Figs. 3.4(c) and 3.4(d).

Fig. 3.2 shows Hall resistivity, $\rho_{xy}(H)$ for $H \parallel c$ and $\rho_{zx}(H)$ for $H \perp c$, of $Mn_{3-x}Fe_xSn$ measured at sample temperatures of 260 and 300 K. From Fig. 3.2(a), we observe that the Hall resistivity (ρ_{xy}) of Mn_3Sn is as high as 2.3 $\mu\Omega$-cm at 260 K driven by a critical field of 0.3 T which is slightly reduced to 2 $\mu\Omega$-cm at 300 K. From $\rho_{zx}(H)$ of Mn_3Sn shown in Fig. 3.2(b), we observe anomalous Hall resistivity (AHR) as high as 6.5 $\mu\Omega$-cm at 300 K that in good agreement with previous studies on this system [131]. Next, from $\rho_{xy}(H)$ of $Mn_{2.8}Fe_{0.2}Sn$ as shown in Fig. 3.2(c), we observe Hall resistivity as high as 2 $\mu\Omega$-cm at 260 K at a critical field of 0.19 T which then reduces to 1.6 $\mu\Omega$-cm at 300 K. Compared to Mn_3Sn, we notice significant decrease in AHR in $Mn_{2.8}Fe_{0.2}Sn$ [see $\rho_{zx}(H)$ from Fig. 3.2(d)], particularly at room temperature. Ideally, anomalous Hall effect is not expected in the in-plane Hall resistivity [$\rho_{xy}(H)$] of these systems [32]. But we find non-negligible anomalous Hall signal from the $\rho_{xy}(H)$ data of $Mn_{2.75}Fe_{0.25}Sn$ [see Fig. 3.2(e)], possibly a component of $\rho_{zx}(H)$ [see Fig. 3.2(f)] projected due to difficulties in making perfect Hall connections on the sub-millimeter sized crystals. However, from the zoomed-in ρ_{xy}(H) data of $Mn_{2.75}Fe_{0.25}Sn$ [see inset in Fig. 3.2(e)] we can clearly identify a cusp in Hall signal (marked by blue circles) at a critical field of 0.1 T. Similarly, Fig. 3.2(g) shows $\rho_{xy}(H)$ of $Mn_{2.65}Fe_{0.35}Sn$ in which again we find non-negligible anomalous Hall signal coming from $\rho_{zx}(H)$ [see Fig. 3.2(h)]. Most importantly, we do not find any visible cusp in ρ_{xy}(H) data of $Mn_{2.65}Fe_{0.35}Sn$. Thus, as we go from Mn_3Sn to $Mn_{2.65}Fe_{0.35}Sn$ we can clearly notice two things: i) The intensity of cusp in $\rho_{xy}(H)$ and the critical field at which the cusp appears decrease with increasing Fe doping and ii) Anomalous Hall signal in $\rho_{zx}(H)$ decreases with increasing Fe doping. Particularly, $\rho_{xy}(H)$ and $\rho_{zx}(H)$ of $Mn_{2.65}Fe_{0.35}Sn$ are nearly suppressed at room temperature.

Next, coming to the important results of this study, Figs. 3.5(a)-(d) show topological Hall resistivity (THR), $\rho^T_{xy}(H)$, of $Mn_{3-x}Fe_xSn$ (x=0, 0.2, 0.25, and 0.35) extracted from the total Hall resistivity [$\rho_{xy}(H)$] shown in Figs. 3.2(a), 3.2(c), 3.2(e), and 3.2(g), respectively. Note here that the total Hall resistivity shown in Fig. 3.2 has contributions from normal Hall resistivity (ρ^N_H) which varies linearly with the field ($\rho^N_H = R_0\mu_0H$), anomalous Hall resistivity (ρ^A_H) which depends on the magnetization ($\rho^A_H = S_A\rho^2M$), and topological Hall resistivity (ρ^T_H). All these contributions lead to a total Hall resistivity as per the relation $\rho_H = \rho^N_H + \rho^A_H + \rho^T_H = R_0\mu_0H + S_A\rho^2M + \rho^T_H$. Here R_0 is a normal Hall coefficient and S_A is an anomalous Hall coefficient. To find the topological Hall resistivity one has to subtract the normal and anomalous Hall contributions from the total Hall resistivity, following a method that has been explained thoroughly in several reports [32, 54, 79, 131]. However, since the anomalous Hall effect is negligible in ρ_{xy} of these systems, we extracted ρ^T_{xy} by simply subtracting the normal Hall contribution in the case of x=0 and x=0.2. For x=0.25 and x=0.35, we extracted ρ^T_{xy} by subtracting the anomalous Hall component originated from ρ_{zx}(H). Overall, Fig. 3.5 suggests that room temperature ρ^T_{xy} is maximum in Mn_3Sn which then decreases with increase in doping and completely gets suppressed by x=0.35 of Fe doping. Moreover, the critical field at which the THE takes places also decreases with increase in doping.

Fig. 3.6(a) and 3.6(b) show $\rho_{xy}(H)$ and $\rho_{zx}(H)$ of $Mn_{2.8}Fe_{0.2}Sn$, respectively measured at low temperatures ($\leq$150 K). Interestingly, unlike in Mn_3Sn (see Ref. [132] for low temperature data), significant Hall resistivity was found in $Mn_{2.8}Fe_{0.2}Sn$ as high as 36 $\mu\Omega$-cm at 2 K at an applied field of 4 T. We further observe hysteresis in ρ_{xy}(H) when measured at 2 and 5 K, which is consistent with our magnetization $M(H)$ data [see Fig.3.4(c)]. This sug-

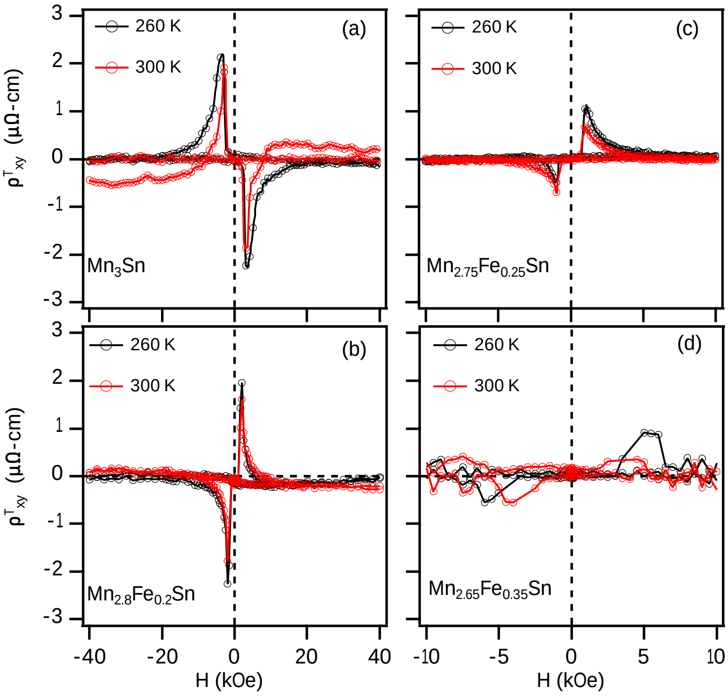

Figure 3.5: xy-plane topological Hall resistivity (ρ^T_{xy}) plotted as a function of the field from Mn_3Sn (a), $Mn_{2.8}Fe_{0.2}Sn$ (b), $Mn_{2.75}Fe_{0.25}Sn$ (c), and $Mn_{2.65}Fe_{0.35}Sn$ (d).

gests that the anomalous Hall resistivity observed in $Mn_{2.8}Fe_{0.2}Sn$ is mostly originated by the Fe-doping induced ferromagnetism [132]. Further, unlike in Mn_3Sn, from Fig. 3.6(b), we can see finite ρ_{zx} in $Mn_{2.8}Fe_{0.2}Sn$ even at 2 K which increases with temperature. We find $\rho_{zx}\approx$ 9.5 $\mu\Omega$-cm at 150 K. We also notice field-induced asymmetric hysteresis in ρ_{zx} (H) at 2 and 5 K. Observation of asymmetric hysteresis in $\rho_{zx}(H)$ is consistent with the field-induced asymmetric $M(H)$ isotherm measured at 2 K [see Fig.3.4(d)]. Fig. 3.6(c) depicts $\rho^T_{xy}(H)$ extracted from $Mn_{2.8}Fe_{0.2}Sn$ by following the above discussed technique. While Mn_3Sn shows no topological Hall resistivity in the xy-plane below 260 K, $Mn_{2.8}Fe_{0.2}Sn$ shows topological Hall resistivity as high as 4.5 $\mu\Omega$-cm at 2 K, which gradually decreases with increasing temperature. But at 100 K, we notice that the sign of ρ^T_{xy} switches from negative to positive for the positive magnetic fields and from positive to negative for the negative magnetic fields as shown in Figs. 3.6(c). Fig. 3.6(d) shows the normal Hall coefficient (R_0) and the anomalous Hall coefficient (S_A) plotted as a function of temperature, from which we notice negative normal Hall coefficient at low temperatures, suggesting for dominant electron carriers and at high temperatures R_0 becomes positive due to dominant hole carriers. The normal Hall coefficient sign switching is in-line with the sign change observed in the topological Hall resistivity [see Fig. 3.6(c)]. Further, the anomalous Hall coefficient gradually decreases with increasing temperature from 0.18 V^{-1} at 2 K to 0.01 V^{-1} at 150 K and beyond 150 K S_A is temperature independent.

Overall, the room-temperature pure and large topological Hall effect observed in Mn_3Sn

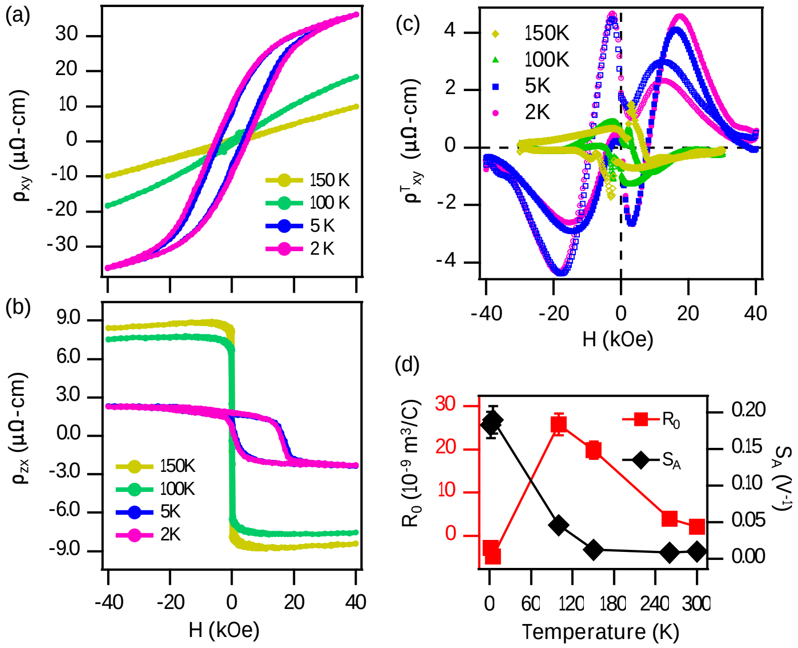

Figure 3.6: Low temperature ($\leq$150 K) Hall resistivity of $Mn_{2.8}Fe_{0.2}Sn$ plotted as a function of field from the xy-plane (a) and zx-plane (b). (c) topological Hall resistivity (ρ^T_{xy}) plotted as a function of the field. (d) Normal Hall coefficient (R_0) and anomalous Hall coefficient (S_A) are plotted as a function of temperature (see the text for more details).

is an important discovery of this study as to date no other system shows ρ^T_{xy} as high as 2 $\mu\Omega$-cm at 300 K for such a low critical field of 0.3 T. Moreover, earlier studies on Mn_3Sn reported topological Hall resistivity, ρ^T_{xy}, in the range of 0.3 - 2.1 $\mu\Omega$-cm besides large anomalous Hall signal [41, 133, 134]. Also, a few systems other than Mn_3Sn show room-temperature THE but again with coexisting AHE. For instance, noncollinear ferromagnet $LaMn_2Ge_2$ shows topological Hall resistivity of $\approx 1\mu\Omega$-cm, in addition to a comparable anomalous Hall resistivity of 0.5 $\mu\Omega$-cm at 300 K [135]. Frustrated Kagome ferromagnet, Fe_3Sn_2, shows topological Hall resistivity of $2\mu\Omega$-cm besides a large anomalous Hall resistivity of 4.5 $\mu\Omega$-cm at 300 K [136]. Similarly, there exists many chiral and skyrmionic systems such as $CrTe_2$ [137], NiMnGa [138], Mn_2PtSn [139], and YMn_6Sn_6 [140] showing room-temperature topological Hall resistivity with a significant AHE signal. So far, Gd_2PdSi_3 is the only system showing a large topological Hall resistivity of 2.5 $\mu\Omega$-cm, with negligible AHE signal, but at very low-temperatures ($<$ 25 K) [48]. Interestingly, $Mn_{2.8}Fe_{0.2}Sn$ also show pure room-temperature THE with $\rho^T_{xy} \approx$ 1.6 $\mu\Omega$-cm at a critical field of 0.2 T, which then increases up to $\approx 4.5\mu\Omega$-cm with decreasing temperature down to 2 K at a critical field of 1.7 T. Note here that the low temperature THE in $Mn_{2.8}Fe_{0.2}Sn$ is coexisted with AHE.

Topological Hall resistivity has been observed in many skyrmionic [39, 48, 102, 103] and non-coplanar spin-structured systems [42, 51, 135, 140]. There exist various proposals to understand the stabilization of the skyrmion lattice in solids such as (i) DM interaction in noncentrosymmetric systems [108, 141, 142], (ii) uniaxial magnetocrystalline anisotropy in the centrosymmetric systems [46, 47, 143, 144], and (iii) in the systems with chiral domain walls [145–148]. Based on our experimental findings, we propose that the clean room-temperature xy-plane THE signal found in $Mn_{3-x}Fe_xSn$ for x=0, 0.2, 0.25 is originated either from the real-space Berry phase due to skyrmion lattice generated from the field-induced domain walls (DW) [41, 145, 149, 150] or from the non-coplanar spin structure [39, 48, 102, 103]. However, the low-temperature large THE found in $Mn_{2.8}Fe_{0.2}Sn$ and in other Fe doped systems (x=0.25 and 0.35, reported separately in [132]) could be originated from the magnetocrystalline anisotropy induced by Fe doping [132, 143, 151].

3.4 Summary

In summary, for the first time, we show a room-temperature pure in-plane topological Hall effect in $Mn_{3-x}Fe_xSn$ which decreases with increasing Fe doping and is suppressed by a doping concentration of x=0.35. We show that the room-temperature topological properties are highly anisotropic in these systems. We also discovered that a small amount of Fe doping in Mn_3Sn causes dramatic changes in the low temperature topological properties. Additional experimental studies using Lorentz transmission electron microscopy (LTEM) would be helpful to map the skyrmionic lattice in these systems. Moreover, our findings demand suitable theoretical models for understanding the high-temperature topological Hall effect in the Kagome lattice systems.

Chapter 4

Tuning of Topological Properties in the Strongly Correlated Antiferromagnet Mn_3Sn via Fe Doping

---

4.1 Introduction

Magnetic topological materials are the illustrations of an interplay between magnetic and electronic states of matter, providing an important stage for illuminating several exotic phenomena such as the anomalous Hall effect (AHE) [35, 152, 153], the topological Hall effect (THE) [39, 54, 154], the skyrmionic lattice [40, 155, 156], and etc. On the other hand, the kagome lattice in which atoms are arranged in star-like formation anticipates a geometrical frustration, leading to noncollinear antiferromagnetic (AFM) ordering [142, 157–161]. So far, several kagome intermetallics have been explored to a great extent due to their potential magnetic topological properties. For instance, $Co_3Sn_2S_2$ is a magnetic Weyl semimetal showing giant AHE in addition to chiral anomaly [73, 77], $Mn_3Sn(Ge)$ are time-reversal symmetry broken Weyl semimetals, despite being antiferromagnets, show large AHE induced by the nonzero k-space Berry curvature [32, 33, 78, 79], Fe_3Sn_2 which is a kagome ferromagnet generates skyrmionic bubbles in addition to the giant AHE [53, 162], YMn_6Sn_6 is a rare earth based kagome system showing several competing magnetic orders and large THE [140], and $Gd_3Ru_4Al_{12}$ posses low temperature skyrmion lattice induced by the magnetic frustration [52].

Skyrmions, the vortex-like spin texture formation in the real space, are topologically protected and characterized by their topological charge called the winding number [44]. The skymions pursuit futuristic technological applications in the high-density data storage devices [49, 163], fine current controlled devices [164], and information processing devices [165]. There exist several systems showing skyrmion lattice that is originated from different mechanisms. For example, in noncentrosymmetric magnetic systems such as MnSi [156], FeGe [112], and FeCoSi [155] the skyrmion lattice formation was understood

---

[0] Results presented in this chapter are published in Phys. Rev. B 106, 144429 (2022)

by the Dzyaloshinskii-Moriya interaction (DMI) under the strong spin-orbit coupling [50, 104]. In the centrosymmetric magnetic systems such as $La_{2-2x}Sr_{1+2x}Mn_2O_7$ [46] and Fe_3Sn_2 [53] the competition between magnetic dipole interactions and uniaxial magnetocrystalline anisotropy stabilizes the skyrmion lattice [143, 151, 166]. In addition, recent studies show the existence of skyrmions in rare-earth based intermetallics Gd_2PdSi_3 and $Gd_3Ru_4Al_{12}$ due to the magnetic frustration [48, 52].

Mn_3Sn is a kagome itinerant antiferromagnet with a Néel temperature of 420 K, has hexagonal crystal structure with a space group of $P6_3/mmc$ [32, 122]. Here, the Mn atoms form kagome network in the *ab* plane of the crystal, showing chiral 120° inverse triangular spin structure stabilized by the DM interaction [108, 142]. Due to a slight distortion in kagome lattice and as well off-stoichiometry of the system, usually, weak-ferromagnetism is present in this system [32, 161]. Moreover, low-temperature magnetic structure depends on the elemental ratio of Mn and Sn, annealing temperature, and crystal growth techniques. Thus, some studies report helical spin structure in Mn_3Sn at low temperatures [119, 167] while the other studies realized spin-glass state below 50 K [123, 168]. At room temperature, Mn_3Sn shows noncollinear antiferromagnetic ordering with 120^0 inverse triangular spin structure [32, 108, 142, 161] leading to large anomalous Hall effect. Particularly, Mn_3Sn is of great research interest as the triangular-coplanar magnetic order reshapes into a spiral-noncoplanar magnetic ordering with a finite net magnetization along the *c*-axis at a critical spin-reorientation transition temperature ($T_{SR} \approx 260$ K) [32, 108, 142] which is not found in Mn_3Ge [169]. As a result, the large AHE is suppressed below T_{SR} in Mn_3Sn but not in Mn_3Ge [80].

Theoretically, Mn_3Sn is not expected to show topological Hall effect (THE) as the stoichiometric Mn_3Sn does not possess chiral-spin texture. However, there are few reports claiming the observation of a small topological Hall resistivity due to the field induced chiral-spin texture in polycrystalline Mn_3Sn [131] at low temperature and due to domain wall formation in the single crystalline Mn_3Sn at room temperature [133, 134]. On the other hand, Fe_3Sn sharing similar crystal structure of Mn_3Sn is a ferromagnetic metal with an easy axis of magnetization in the *ab* plane that can be shifted to the *c*-axis with doping [170, 171]. Motivated from the polymorphic magnetic properties of Mn_3Sn and flexibility of manipulating the easy axis in Fe_3Sn, we have substituted Fe atoms at Mn sites of Mn_3Sn to enhance the topological properties of Mn_3Sn as Fe substitution introduces ferromagnetism to the system.

In this work, single crystals of $Mn_{3-x}Fe_xSn$ (x=0, 0.25, and 0.35) were systematically studied for their electrical resistivity, magnetic, and topological properties. While Mn_3Sn is found to be metallic in nature up to room temperature with a spin-reorientation driven kink at 260 K, with Fe doping the system shows magnetism induced metal-insulator (MI) transition at 240 K for x=0.25 and 150 K for x=0.35. In addition to MI transition, x=0.35 system shows disorder induced resistivity upturn with a minima at T_m=50 K. As for the magnetic properties, Mn_3Sn is found to show a sudden drop in magnetization at a spin-reorientation transition temperature of 260 K and spin-glass-like transition below 40 K. On the other hand, with Fe doping ferromagnetic transition has been introduced alongside with enhanced magnetic anisotropy. Also, anisotropic anomalous Hall resistivity has been induced at low temperatures with Fe doping. Particularly, the out-of-plane Hall resistivity (ρ_{zx}) increases with decreasing temperature for all the compositions from 300 K down to their respective magnetic transition temperatures where a sudden change in Hall resistivity is noticed. Though not much change in out-of-plane Hall resistivity is noticed with Fe doping at 2 K, the in-plane Hall resistivity (ρ_{xy}) is gigantically enhanced from -0.25 $\mu\Omega$-cm to 48 $\mu\Omega$-cm in going from x=0 to x=0.35. Along with the anomalous Hall resistivity, a large topological Hall resistivity also is observed for both Fe doped systems at 2 K.

4.2 Experimental details

Single crystals of $Mn_{3-x}Fe_xSn$ (x=0, 0.25, and 0.35) were prepared by self flux method [41, 118, 172]. First, Mn (Alfa Aesar 99.995%), Fe (Alfa Aesar, 99.99%), and Sn (Alfa Aesar 99.998%) powders were taken with a ratio of (7-x) : x : 3, mixed thoroughly before inserting into a preheated quartz tube, and sealed under partial Argon pressure. The mixture was then heated up to 1000^oC, slowly cooled down to 900^oC, and then was air quenched to room temperature by taking out the ampoule from furnace. In this way, we obtained shiny hexagonal and rod shaped single crystals with a typical size of 1.5 mm × 1 mm × 1 mm. X-ray diffraction (XRD) measurements were done on different surfaces of the single crystals using Rigaku SmartLab equipped with 9 kW Cu K_α X-ray source. Elemental compositions of the crystals were calculated to be $Mn_{2.97}Sn_{1.03}$, $Mn_{2.74}Fe_{0.26}Sn$, and $Mn_{2.64}Fe_{0.36}Sn$ using energy dispersive X-ray spectroscopy (EDXS) technique. For convenience we denote the compositions $Mn_{2.97}Sn_{1.03}$, $Mn_{2.74}Fe_{0.26}Sn$, and $Mn_{2.64}Fe_{0.36}Sn$ by x=0, x=0.25, and x=0.35, respectively, wherever applicable.

Electrical resistivity measurements were carried out in the linear four-probe method and Hall measurements were done in the measuring geometry shown in the schematic of Fig. 6.1(e). Magneto-transport and magnetization measurements were performed in Physical Properties Measurement System (9T PPMS, DynaCool, Quantum Design) using ETO and VSM options, respectively. Hall resistivity was measured for two different orientations as shown in Fig. 6.1(e). ρ_{xy} stands for current along the x direction and field along the z direction where Hall voltage was measured along the y direction. Similarly ρ_{zx} stands for current along z direction, field along the y direction, and Hall voltage was measured along

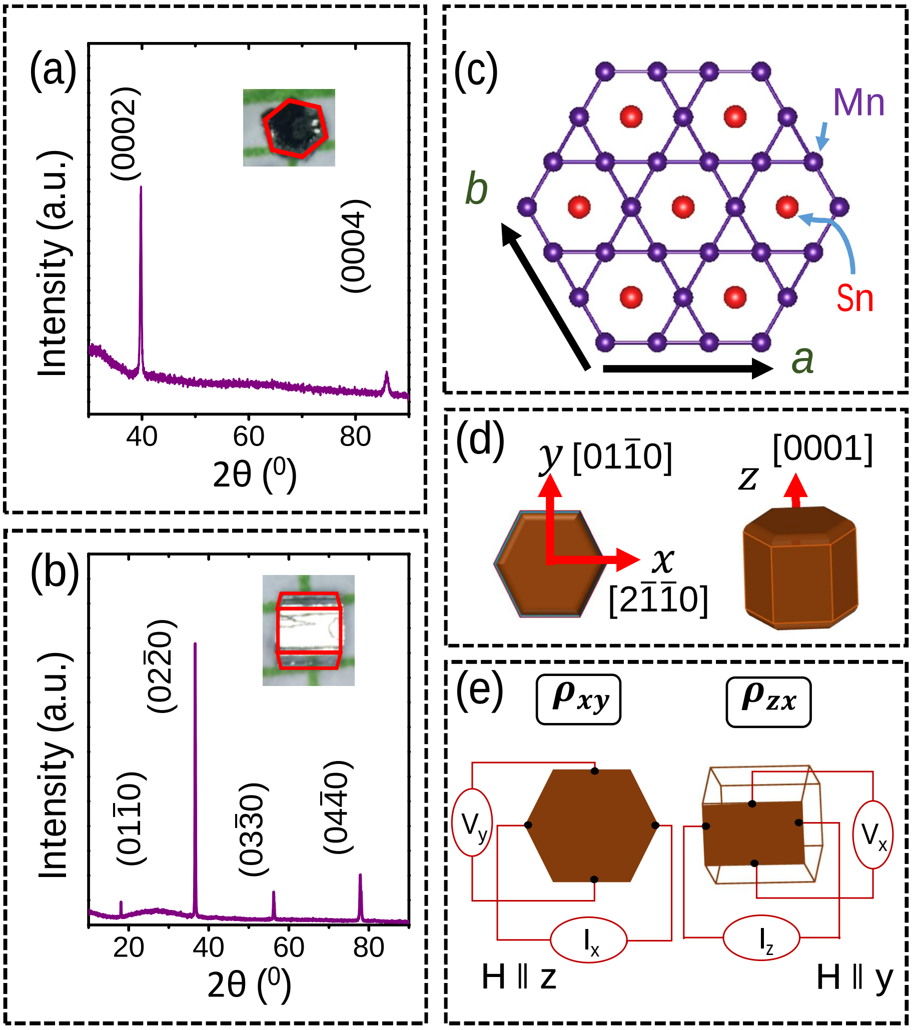

Figure 4.1: (a) and (b) show typical XRD patterns of Mn$_3$Sn single crystal taken from two different orientations as shown in the inset images. (c) Schematic hexagonal lattice of Mn_3Sn in the ab plane where Mn atoms form kagome geometry and Sn atoms sit in the center of hexagon. In (d), x, y, and z -axes correspond to $[2\bar{1}10]$, $[01\bar{1}0]$, and $[0001]$ orientations, respectively. Magnetotransport measuring geometry is shown in (e), where ρ_{xy} is measured with current along the x-axis and external magnetic field applied along the z-axis to find Hall voltage along the y-axis and ρ_{zx} is measured with current along the z-axis and field applied along the y-axis to find Hall voltage along the x-axis.

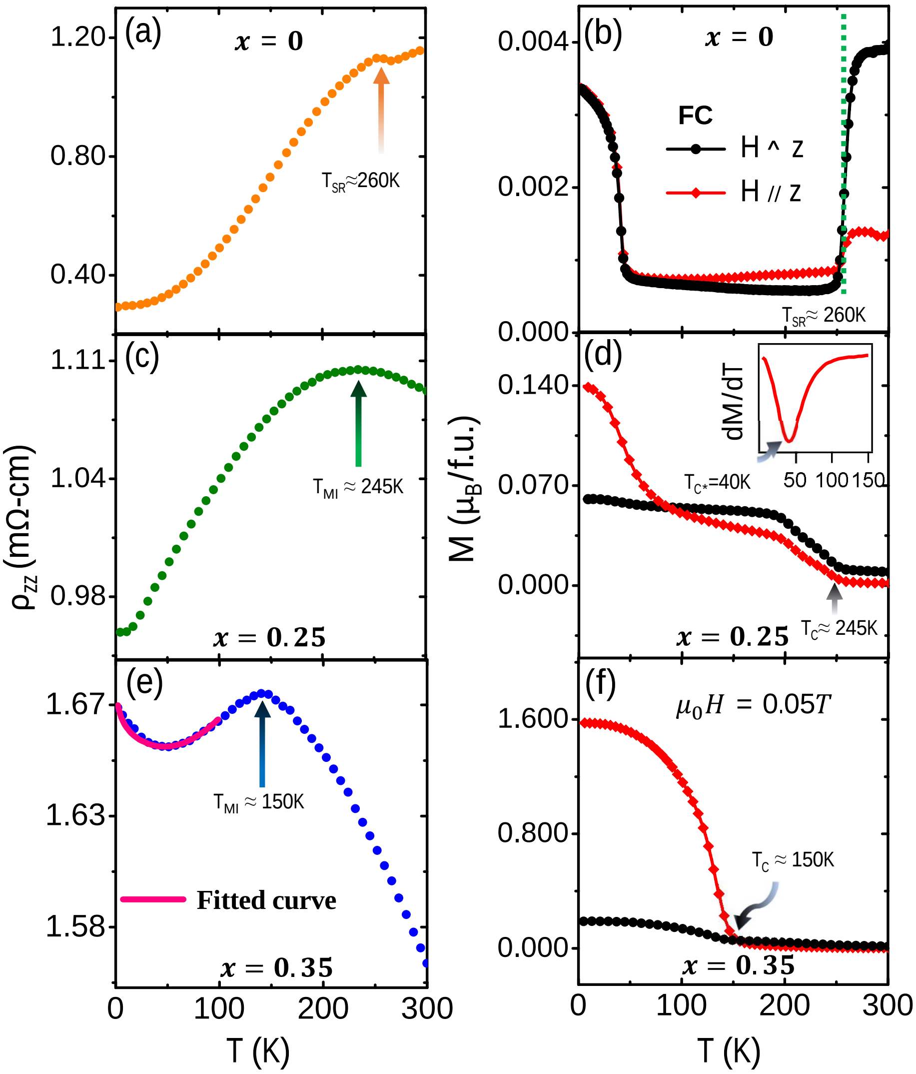

Figure 4.2: Temperature dependent resistivity (ρ_{zz}) is measured with current along the z-axis for $Mn_{3-x}Fe_xSn$ where (a) x=0, (c) x=0.25, and (e) x=0.35. (b), (d), (f) show temperature dependent magnetization for x=0, x=0.25, and x=0.35, respectively, measured in the field-cooled (FC) mode.

the x direction. To eliminate longitudinal voltage contribution due to any possible misalignment of the probes, the Hall resistivity was calculated by $\frac{\rho(H)-\rho(-H)}{2}$. Temperature dependent Hall resistivity measurements were done using both positive (H) and negative (-H) applied fields and then calculated using the formula $\frac{\rho(T,H)-\rho(T,-H)}{2}$.

4.3 Results and Discussions

XRD patterns shown in Figs. 6.1(a) and 6.1(b) represent intensity reflections of (0002) and $(01\bar{1}0)$ hexagonal planes, respectively, taken from Mn_3Sn single crystal. Figs. 5.3(a), (c), and (e) depict zero-field out-of-plane resistivity (ρ_{zz}) measured between 2 and 300 K from Mn_3Sn, $Mn_{2.75}Fe_{0.25}Sn$, and $Mn_{2.65}Fe_{0.35}Sn$ single crystals, respectively. Overall,

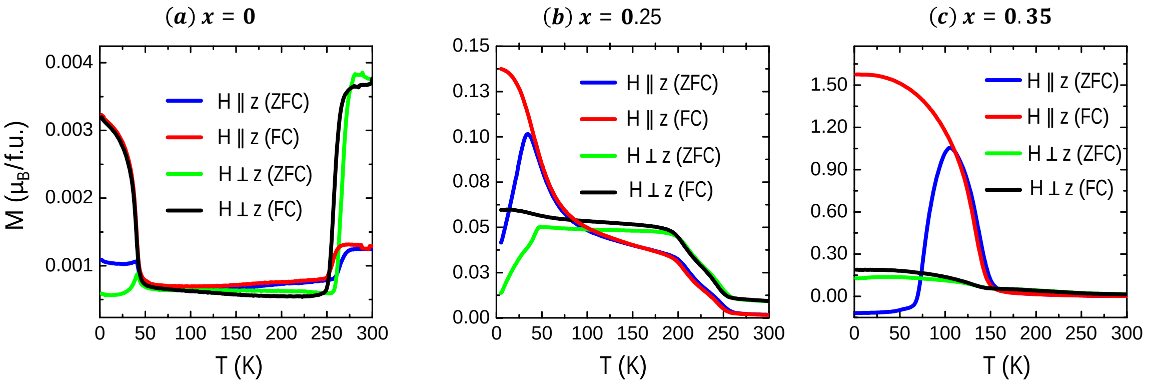

Figure 4.3: Zero field cooled and field cooled magnetization data for (a) $x = 0$, (b) $x = 0.25$, and (c)$x = 0.35$

a metallic nature of resistivity is observed from Mn_3Sn, except that a kink has been noticed at $T_{SR} = 260K$ where a spin-reorientation (SR) transition from in-plane noncollinear AFM order to an out-of-plane spin-spiral structure occurs [118, 119]. Observation of kink in the electrical resistivity of Mn_3Sn is consistent with earlier reports [41, 118, 122]. On the other hand, we observe a metal-insulator (MI) transition in $Mn_{2.75}Fe_{0.25}Sn$ at 240 K, which further reduced to 150 K in $Mn_{2.65}Fe_{0.35}Sn$ as shown in Figs. 5.3(c) and 5.3(e) with increasing Fe concentration. Earlier, the authors found a MI transition at 265 K in the case of $Mn_{2.8}Fe_{0.2}Sn$ [173]. In addition to the MI transition, in $Mn_{2.65}Fe_{0.35}Sn$, we identify low-temperature resistivity upturn with a minima at T_m=50 K. The resistivity upturn at low temperature could be due to (i) weak localization [174–176], (ii) Kondo effect [175, 177], or (iii) elastic electron-electron ($e-e$) scattering [175, 178]. In order to elucidate the mechanism of resistivity upturn, we fit the data with relevant formulae involved in the above mentioned three mechanisms. We got the best fitting for the $e-e$ scattering which takes the form $\rho(T) = \rho_0 - \alpha T^{\frac{1}{2}} + \beta T^2$, as Fe doping induces disorder in addition to the electron carrier population. See the references [119, 161, 167, 174, 175, 177–180] for more details.

To witness the effect of Fe doping on the magnetic properties, we performed temperature dependent magnetization M(T) with field applied parallel ($H \parallel z$) and perpendicular ($H \perp z$) to the z-axis. From the M(T) data of Mn_3Sn as shown in Fig. 5.3 (b) we find a sudden drop in the in-plane magnetic moment at T_{SR}=260 K due to spin transformation from inverse triangular to helical or spiral configuration [41, 118]. Similarly, we find drop in the out-of-plane magnetic moment as well at T_{SR}=260 K but not as large as the in-plane. Reducing the sample temperature to below 40 K, we observe increasing in-plane and out-of-plane magnetic moments due to spin-glass-like transition [118, 168]. With Fe doping, in the case of x=0.25, isotropic increase in magnetization is observed [see Fig. 5.3(d)] for both $H \parallel z$ and $H \perp z$ field orientations with a ferromagnetic-like transition at a T_C=240 K. With fur-

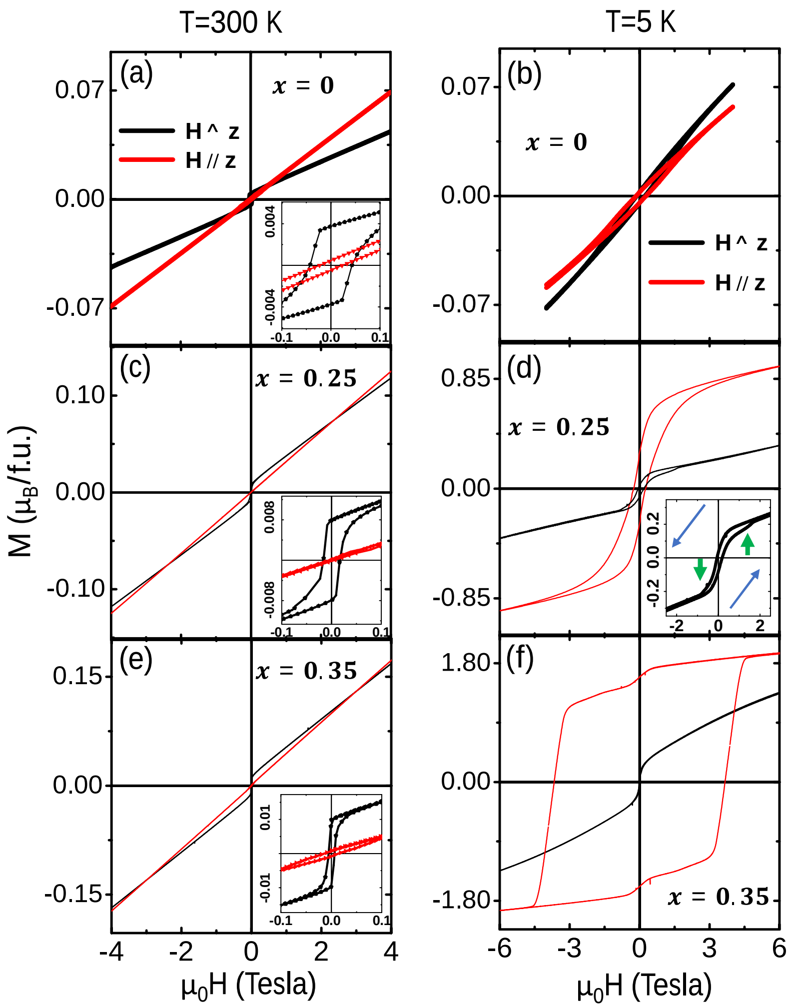

Figure 4.4: (a), (c), and (e) show M(H) isotherms of $Mn_{3-x}Fe_xSn$ measured at 300 K for x=0, x=0.25, and x=0.35, respectively. (b), (d), and (f) show M(H) isotherms measured at 5 K for x=0, x=0.25, and x=0.35 respectively. Zoomed-in images of respective isotherms are show in the insets. Inset of (d) points to the asymmetric hysteresis (see the text for more details).

ther lowering sample temperature the in-plane magnetic moment gets saturated, while the out-of-plane magnetization show additional ferromagnetic-like transition at T_{C^*}=40 K, enhancing the anisotropy of the magnetic structure at low temperatures. Further, with more Fe doping, i.e., from x=0.35 we see a ferromagnetic-like transition at T_C=150 K for both orientations though the out-of-plane magnetization ($1.6\mu_B/f.u.$) is much stronger compared to in-plane magnetization ($0.3\mu_B/f.u.$) at 2 K. Decreasing T_C with increasing Fe concentration is consistent with a previous report [181]. In conjunction, from the magnetization data shown in Figs. 5.3(b), (d), and (f) and the electrical resistivity shown in Figs. 5.3(a), (c), and (e) we find that the metal-insulator transition occur nearly at the same temperature of ferromagnetic transition in $Mn_{2.75}Fe_{0.25}Sn$ and $Mn_{2.65}Fe_{0.35}Sn$, suggesting that ferromagnetism could be a plausible origin of MI transition in these systems.

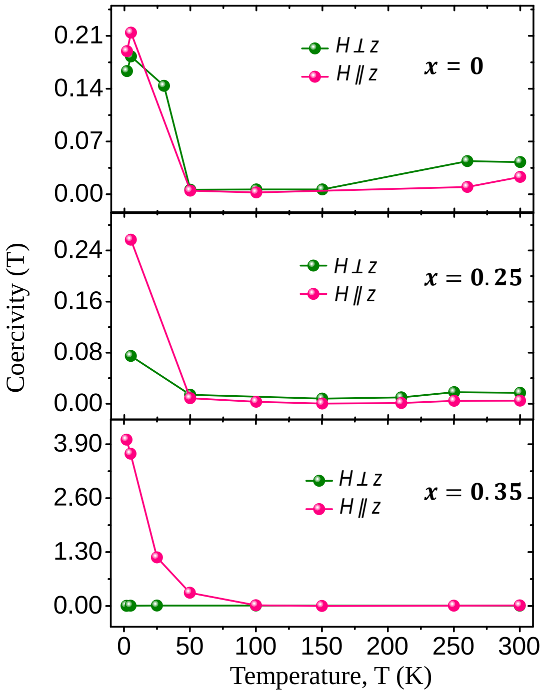

Figure 4.5: Coercivity plotted as a function of temperature for both H || z and H $\perp$ z. Top panel shows the data from Mn_3Sn, middle panel shows the data from $Mn_{2.75}Fe_{0.25}Sn$, and the bottom panel shows the data from $Mn_{2.65}Fe_{0.35}Sn$.

Fig. 5.4 depicts magnetization isotherms M(H) measured at various sample temperatures for both $H \parallel z$ and $H \perp z$ orientations. Figs. 5.4(a), 5.4(c), and 5.4(e) show isotherms of x=0, x=0.25, and x=0.35 samples, respectively, measured at 300 K and Figs. 5.4(b), 5.4(d), and 5.4(f) show isotherms of x=0, x=0.25, and x=0.35, respectively, measured at 5 K. From the inset of Fig. 5.4(a) we observe significant hysteresis for Mn_3Sn at 300 K, similar to a previous report where a weak in-plane ($H \perp z$) ferromagnetism is observed with an effective magnetization of 0.004 $\mu_B/f.u.$ [32]. Origin of this weak ferromagnetism is understood from the kagome lattice distortion or off-stoichiometry of the composition [32,118]. On the other hand, the out-of-plane magnetization ($H \parallel z$) changes linearly with applied field like a typical AFM system.

Next examining the isotherms measured at 5 K [see Figs. 5.4(b), (d), and (f))], from Mn_3Sn, the M(H) curves look almost linear for both $H \parallel z$ and $H \perp z$ except that a small hysteresis due to spin-glass transition is observed. On the other hand, from the x=0.25 and x=0.35 systems we observe significant changes in the out-of-plane magnetic structure with Fe doping as the coercivity and spontaneous magnetization increase dramatically, while changes in the in-plane magnetic structure are minimal with Fe doping though the M(H) loop modifies from linear to sigmoid-like ingoing from x=0 to x=0.35. For x=0.35, the out-of-plane magnetization (1.8 $\mu_B/f.u.$) and coercivity (4 T) are extremely large compared to the in-plane magnetization (1 $\mu_B/f.u.$) and coercivity (50 Oe), demonstrating an enhanced magnetic anisotropy with Fe doping. From a closer observation on the M(H) curve of x=0.25, we find field induced asymmetric M(H) loop [see inset of Fig. 5.4(d)], also observed previously on the metamagnetic Heusler alloy $Ni_{50}Mn_{35}In_{15-x}B_x$ [182] and spin-glass $SrRuO_3/SrIrO_3$ superlattice [43], possibly due to metastable magnetic phase churned out by Fe doping.

To quantify the magnetic anisotropy induced by the Fe doping, we plotted the coercivity measured at various sample temperatures for both $H \parallel z$ and $H \perp z$ orientations in Fig. 4.5. As can be seen from the top panel of Fig. 4.5, for x=0, there is not difference between the in-plane and out-of-plane coercivities and almost constant from 300 K down to 50 K. However below 50 K, though isotropic, it increases drastically with decreasing temperature. For x=0.25, again we find almost constant and nearly zero in-plane and out-of-plane coercivities from 300 K down to 50 K. Below 50 K, both in-plane and out-of-plane coercivities increase with decreasing temperature. However, the out-of-plane coercivity ($H \parallel z$) is almost three times higher than the in-plane coercivity ($H \perp z$) at 2 K. Similarly, in the case of x=0.35, the in-plane coercivity always found to be zero for all the measured temperatures, while the out-of-plane coercivity starts increasing from zero at 100 K to 4 T at 2 K. Further, we estimate the magnetocrystalline anisotropy energy density (K_U) using the Stoner-Wohlfarth model [183, 184] by considering the z-axis as the easy axis (uniaxial) of magnetization. Concentrating only at the low temperature (2 K) where the coercivity is maximum, uniaxial magnetocrystalline anisotropic energy density (K_U) is calculated to be $1.2\times 10^4\ J/m^3$ for x=0.25 and $5.3 \times 10^5\ J/m^3$ for x=0.35. These values are significantly higher compared to previously reported in-plane magnetocrystalline anisotropic energy density of $\sim 10^3\ J/m^3$ from Mn_3Sn [119].

The effect of Fe doping on the topological properties of Mn_3Sn is studied by performing Hall measurements at low temperatures. As shown in Fig. 4.6, we measured out-of-plane [$\rho_{zx}(T)$] and in-plane [$\rho_{xy}(T)$] Hall resistivities as a function of temperature at an applied magnetic filed of 1 T. From Fig. 4.6(a) we can notice that ρ_{zx} of Mn_3Sn increases (negatively) with decreasing temperature from 300 K down to T_{SR}=260 K, and below ρ_{zx} suddenly becomes zero. On the other hand, from Fig. 4.6(b) we can see that ρ_{xy} of Mn_3Sn is almost constant from 300 K down to 2 K. Fig. 4.6(c) depicts ρ_{zx} of x=0.25 in which we can notice an increase (negatively) in Hall resistivity linearly with decreasing temperature down to T_{SR}=115 K, and below this temperature ρ_{zx} slightly increases to -3.6 $\mu\Omega$-cm at 2 K. Fig. 4.6(d) depicts ρ_{xy} of x=0.25 in which we can notice slight increase (positively) in Hall resistivity with decreasing temperature and reaches to 30 $\mu\Omega$-cm at 2 K. Inset in Fig. 4.6(d)

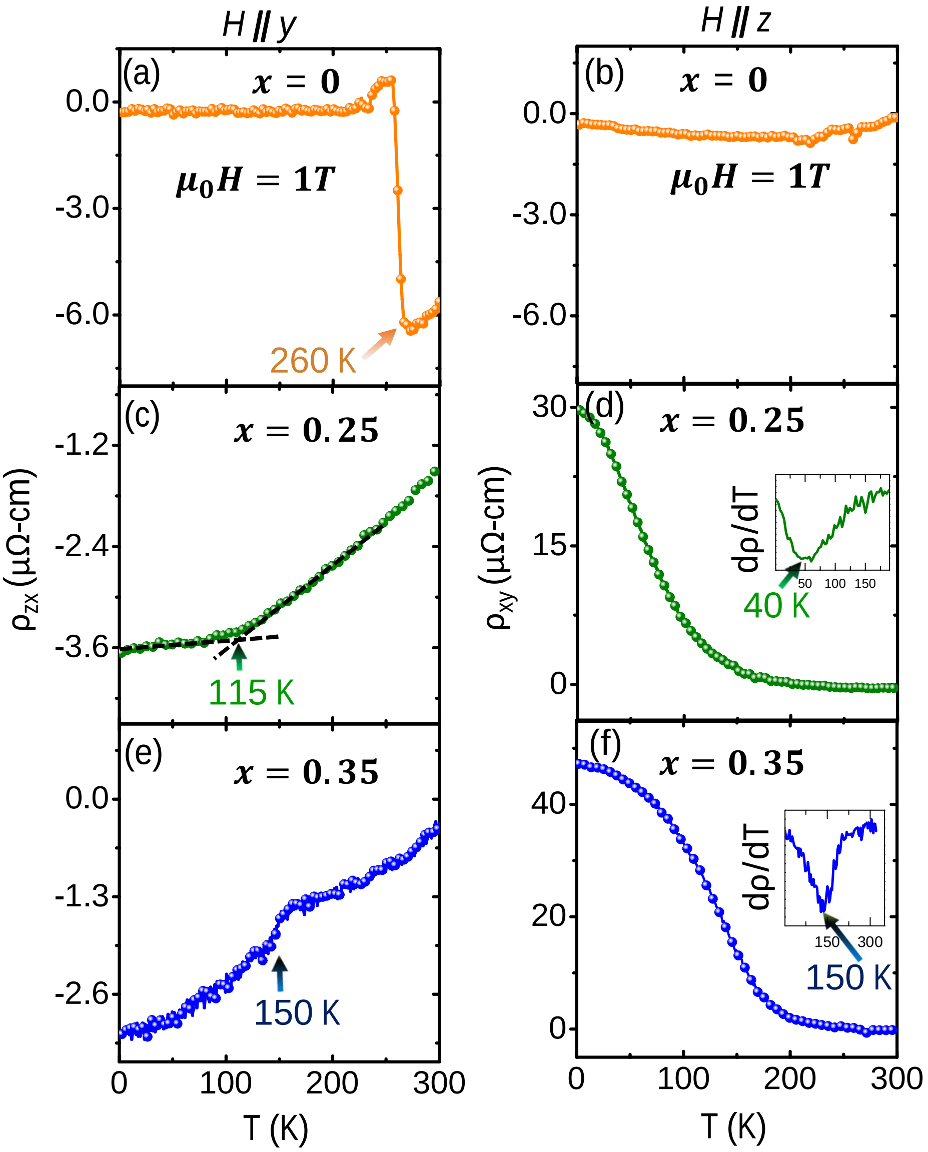

Figure 4.6: Out-of plane Hall resistivity (ρ_{zx}) plotted as a function of temperature measured under the field of 1T from (a) x=0, (c) x=0.25, and (e) x=0.35. (b), (d), and (f) show in-plane Hall resistivity (ρ_{xy}) plotted as a function of temperature measured under the field of 1T from x=0, x=0.25, and x=0.35, respectively. Insets of (d) and (f) show the first derivative of their Hall resistivity with respect to temperature.

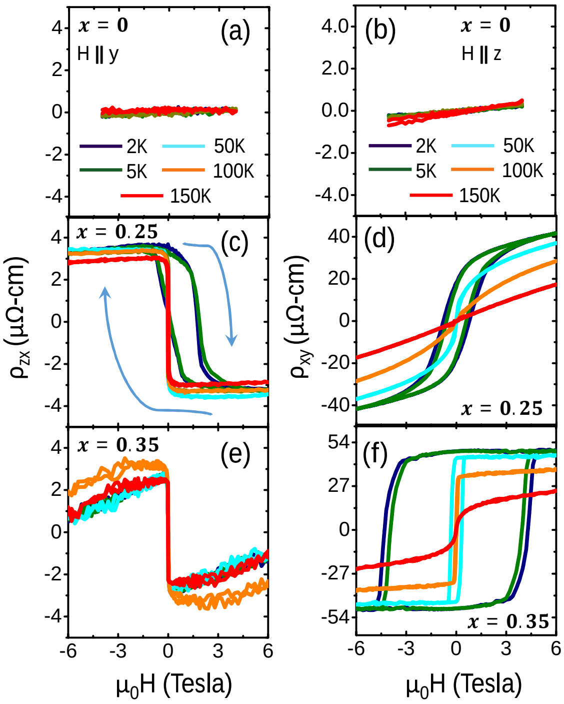

Figure 4.7: Field dependent out-of-plane Hall resistivity ρ_{zx} measured at different temperatures from x=0 (a), x=0.25 (c), and x=0.35 (e). Curved blue arrows in (c) indicate field sweeping direction. Similarly, field dependent in-plane Hall resistivity ρ_{xy} measured at different temperatures from x=0 (b), x=0.25 (d), and x=0.35 (f).

represent $d\rho_{xy}/dT$ having a minima at 40 K, consistent with the ferromagnetic transition temperature of T_{C^*}=40 K [see Fig. 5.3(d)]. Fig. 4.6(e) depicts ρ_{zx} plotted for x=0.35 in which we can notice increase (negatively) in Hall resistivity linearly with decreasing temperature down to 2 K, except that a hump at T_C=150 K is observed. Fig. 4.6(f) depicts ρ_{xy} of x=0.35 in which we notice increase (positively) in Hall resistivity with decreasing temperature and gets saturated to 48 $\mu\Omega$-cm at 2 K. Inset in Fig. 4.6(f) depicts $d\rho_{xy}/dT$ showing minima at the ferromagnetic transition temperature of T_C=150 K [see Fig. 5.3(f)].

From the Hall measurements shown in Fig. 4.6(a) it is clear that the large Hall resistivity (ρ_{zx}) observed from Mn_3Sn at high temperatures is mainly driven by the nonzero k-space Berry phase [32, 78]. However, at low temperatures ($<$ 260 K), the Berry phase disappears due to spin reorientation, and thus, ρ_{zx} is negligible. Whereas the Berry phase is always absent in the xy plane of Mn_3Sn, ρ_{xy} is in general negligible [32]. In this study, we notice T_{SR}=115 K for x=0.25 while no spin-reorientation transition is observed for x=0.35. Worth to mention here that the authors have found spin-reorientation transition at 125 K in the case of $Mn_{2.8}Fe_{0.2}Sn$ [173]. Thus, linear increase (negative) in ρ_{zx} with decreasing temperature down to 115 K for x=0.25 and down to 2 K for x=0.35 is due to nonzero k-space Berry phase [see Figs. 4.6(c) and 4.6(e)]. Astonishingly, the in-plane Hall resistivity (ρ_{xy}) has

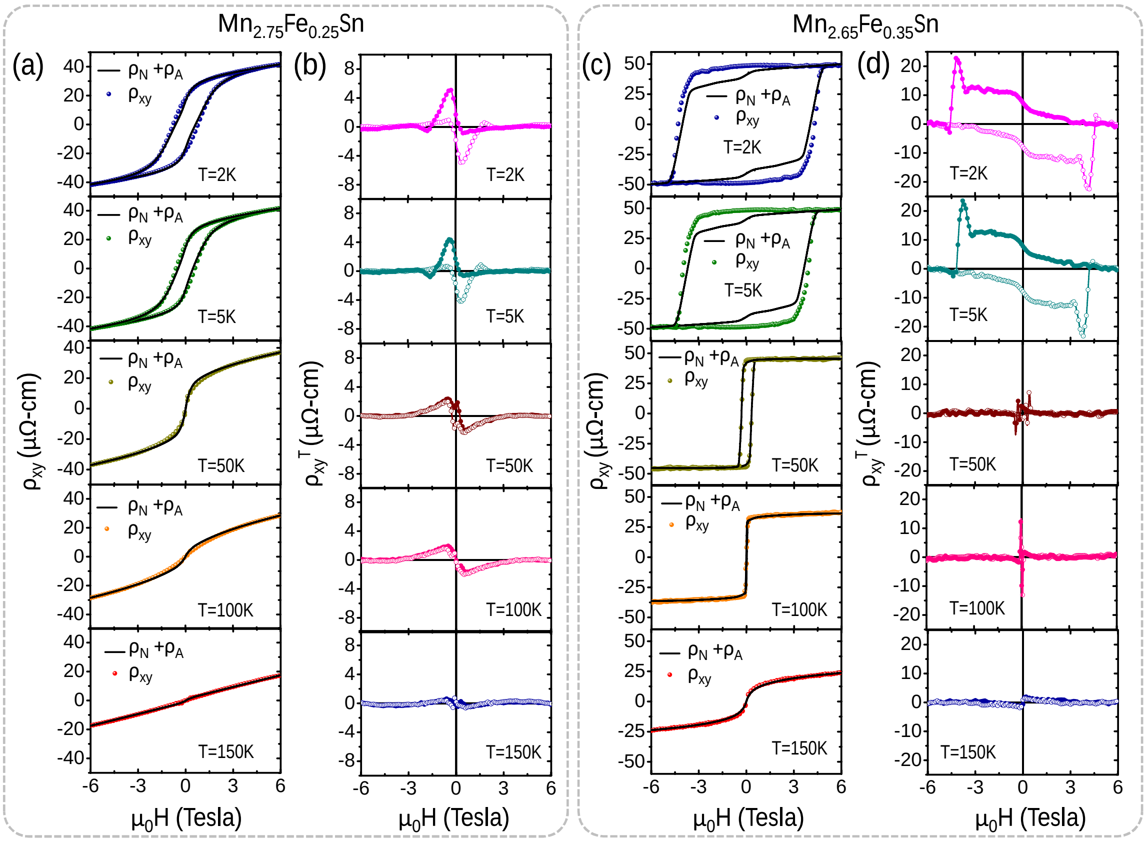

Figure 4.8: (a) and (c) are the field dependent in-plane Hall resistivity (ρ_{xy}) measured at various temperatures from x=0.25 and x=0.35, respectively. The circles are experimental data and the solid black curves are fits to the equation $\rho_H = \rho_N + \rho_A = \mathrm{R}_0\mu_0\mathrm{H} + \mathrm{R}_S\mathrm{M}$ (see the text for more details). (b) and (d) show the derived in-plane topological Hall resistivity (ρ^T_{xy}) from x=0.25 and x=0.35, respectively.

been gigantically enhanced with Fe doping as high as 30 $\mu\Omega$-cm for x=0.25 and 48 $\mu\Omega$-cm for x=0.35 at 2 K. Note here that the in-plane Hall resistivity (ρ_{xy}) is due to the ferromagnetism induced by the Fe doping.

On the other hand, with Fe doping, the spin-reorientation transition temperature reduces to low-temperatures and eventually disappears for higher Fe concentration.

Field dependent Hall resistivity, $\rho_{zx}(H)$ and $\rho_{xy}(H)$, from all the samples measured at different temperatures are shown in Fig. 4.7. Here we mainly focus at low temperatures ($\leq$ 150 K) as the doping induced ferromagnetism significantly increases the Hall resistivity at low temperatures. Since below 260 K, Mn_3Sn is already in the spin-spiral texture we find only the ordinary Hall effect as the out-of-plane Hall resistivity (ρ_{zx}) linearly depends on the field [see Fig. 4.7(a)]. Similarly, we again find ordinary Hall effect from the in-plane Hall resistivity (ρ_{xy}) as well [see Fig. 4.7(b)]. Fig. 4.7(c) depicts $\rho_{zx}(H)$ of x=0.25 in which we observe anomalous Hall resistivity (AHR) with a sudden jump near zero field. Consistent with asymmetric M(H) data of x=0.25 shown in Fig. 5.4(d), asymmetric hysteresis in AHR is noticed at low temperatures (2 and 5 K). As for $\rho_{xy}(H)$ of x=0.25 shown in Fig. 4.7(d), we observe sign reversed anomalous Hall resistivity compared to $\rho_{zx}(H)$. Moreover, low temperature $\rho_{xy}(H)$ curves show hysteresis in AHR resembling the M(H) data of a typical ferromagnetic system [see $H \parallel z$ data in Fig. 5.4(d)]. Fig. 4.7(e) depicts $\rho_{zx}(H)$ of x=0.35 in which we observe an anomalous Hall resistivity with a sudden jump near zero field, similar to x=0.25. However, unlike in x=0.25, we do not find asymmetric hysteresis in $\rho_{zx}(H)$ at low temperatures. Although at zero field we observe a sudden jump in ρ_{zx}, at higher fields ρ_{zx} is dominated by the ordinary Hall effect as it linearly depends on the field. Fig. 4.7(f) depicts $\rho_{xy}(H)$ of x=0.35 in which we observe sign reversed anomalous Hall effect compared to $\rho_{zx}(H)$, again similar to the case of x=0.25. Moreover, the $\rho_{xy}(H)$ curves show hysteresis in AHR resembling the M(H)data of a typical ferromagnetic system [see $H \parallel z$ data in Fig. 5.4(f)]. From Figs. 4.7(d) and 4.7(f) we observe increase in AHR hysteresis with decreasing temperature in both x=0.25 and x=0.35 systems.

The Hall resistivity of a ferromagnetic metal can be expressed as $\rho(H) = \rho^N(H) + \rho^A(H) = \mu_0 R_0 H + R_s M$ [35], where R_0 is normal Hall coefficient which is inversely proportional to carrier density ($R_0 = 1/nq$), R_s is anomalous Hall coefficient, and M is magnetization. However, we are unable to fit properly $\rho_{xy}(H)$ of x=0.25 and x=0.35 using this formula at low temperatures as demonstrated in Figs. 4.8(a) and 4.8(c). This is because $\rho_{xy}(H)$ has significant contribution from the topological Hall resistivity ρ^T_{xy} which can extracted using the formula $\rho^T_{xy}(H) = \rho_{xy}(H) - \rho^N(H) - \rho^A(H)$ as plotted in Figs. 4.8(b) and 4.8(d) for x=0.25 and x=0.35, respectively. A maximum ρ^T_{xy} of 5 $\mu\Omega - cm$ has been derived at a critical field of 0.35 T from x=0.25 and 22 $\mu\Omega - cm$ has been at a critical field of 4 T from x=0.35 at 2 K. The maxima of ρ^T_{xy} decreases with increasing temperature and disappears at around 150 K in x=0.25 [see Fig. 4.8(b)], while the maxima of ρ^T_{xy} in x=0.35 becomes negligible above 50 K [see Fig. 4.8(d)].

The topological Hall resistivity is generated by the itinerant electrons by acquiring real space Berry curvature when passing through the nontrivial spin structure of a scalar spin chirality $\chi_{ijk} = (\delta \mathbf{S}_i . [\delta \mathbf{S}_j \times \delta \mathbf{S}_k])$ [39, 56]. The nontrivial spin structure is topologically protected and produces skyrmion lattice, characterised by the nonzero topological charge called the winding number Q [185, 186]. By taking into account the skyrmionic picture, we can estimate the skyrmion density (n_{sk}) using the relation $B_{\text{eff}} = \phi_0 n_{\text{sk}}$ [54–56]. Here, ϕ_0 is magnetic flux quantum (h/e) and B_{eff} is the effective magnetic field. Also, the topological Hall resistivity ρ^T is directly related to B_{eff} as $\rho^T \approx P R_0 B_{\text{eff}}$ [39, 54, 56, 141]. Here, P is the local spin polarization of charge carrier ($P = \mu_{\text{spon}}/\mu_{\text{sat}}$) [39, 56]. From the fittings shown in Fig. 4.8(a) we derived R_0=-1×10^{-9} m^3/C and from the M(H) data shown in Fig. 5.4(d) we estimated $P = 0.07$ for x=0.25. Here,μ_{spon}=0.659 $\mu_B/f.u.$ taken from Fig. 5.4(d) and μ_{sat}=9 $\mu_B/f.u.$ (3 μ_B/Mn) [32, 124]. Using these values, B_{eff} is calculated to be 720 T. Also, the skyrmion density is estimated to $n_{\text{sk}} \approx 1.7 \times 10^{17}$ m^{-2} with a skyrmion size (helical period) of about $\lambda_{sk} \approx 2.4\ nm$. Similarly, for $Mn_{2.65}Fe_{0.35}Sn$, by taking the fitted value of $R_0 = -1.5 \times 10^{-9}$ m^3/C and calculated value of $P = 0.19$, the estimated effective field $B_{\text{eff}} \approx 770$ T which gives a skyrmion density $n_{\text{sk}} \approx 1.9 \times 10^{17}$ m^{-2} and the skyrmion size $\lambda_{sk} \approx 2.2\ nm$. The skyrmion size is estimated using the formula $\lambda_{sk} = (\frac{h}{e}\frac{\sqrt{3}}{2B_{eff}})^{\frac{1}{2}}$ [48]. For x=0.35, we used μ_{spon}=1.76 $\mu_B/f.u.$ taken from Fig. 5.4(f) and μ_{sat}=9 $\mu_B/f.u.$ (3 μ_B/Mn) [32, 124]. Note here that we presumably considered the same atomic magnetic moment of 3 $\mu_B/atom$ for both Mn and Fe [170]. Further, by assuming that $\approx$ 11.4% (x=0.35) of Fe doing into Mn_3Sn does not significantly change the lattice parameters [187] we estimated the skyrmion density of 9×10^{17} m^{-2} for x=0.25 and 12×10^{17} m^{-2} for x=0.35. skyrmion density values estimated from the crystal structure information are in good agreement with the values estimated from the topological Hall resistivity data.

The skyrmion sizes (λ_{sk}), 2.4 nm from x=0.25 and 2.2 nm from x=0.35, obtained in this study are comparable to the skyrmion size of 2.49 nm observed from Gd_2PdSi_3 [48]. On the other hand, the helical period of $\approx$ 1 nm is obtained from polycrystalline Mn_3Sn [131] which is a factor of 2.4 smaller compared to the size of $Mn_{2.75}Fe_{0.25}Sn$. However, the B20 systems in their bulk form show much longer-period helical structures (skyrmions). For instance, MnSi shows a helical period of $\approx$18 nm [188], FeGe shows a helical period of $\approx$70 nm [189], and Cu_2OSeO_3 shows a helical period of $\approx$62 nm [190]. Worth to mention here that all three above B20 systems show very large helical periods compared to our studied samples of $Mn_{2.75}Fe_{0.25}Sn$ and $Mn_{2.65}Fe_{0.35}Sn$.

Several mechanisms are proposed to understand the stabilization of the skyrmion lattice in solids such as (i) DM interaction in noncentrosymmetric systems [108, 141], (ii) chiral domain wall induced skyrmion lattice [145–148], and (iii) uniaxial magnetocrystalline anisotropy in the centrosymmetric systems [46, 53, 143, 144]. It is quite possible to tune the magnetic anisotropy by doping with alien atoms [191]. For instance, doping Ni or Pd in Fe_3P at the Fe site converts the in-plane anisotropy to the uniaxial out-of-plane anisotropy and thus the formation of antiskyrmions [192] and Li ion doped in Mott insulator La_2CuO_4 acts as a vortex center for the skyrmion [193]. Overall, our study demonstrates that Fe doping into Mn_3Sn converts the in-plane magnetic structure of Mn_3Sn to a uniaxial anisotropic magnetic structure having easy magnetic axis in the z-axis. Hence, Fe doping generates sufficient uniaxial magnetocrystalline anisotropy in Mn_3Sn in addition to the geometrical frustration which help to stabilize the low temperature skyrmion lattice.

4.4 Summary

In summary, we have thoroughly examined the effect of Fe doping on the electrical resistivity, magnetic, and topological properties of Mn_3Sn. Low temperature magnetic structure has been significantly modified with Fe doping. Especially, we find that Fe doping induces ferromagnetism below 240 K in x=0.25 and below 150 K in x=0.35. In addition, we observe ferromagnetism driven metal-insulator transition in Fe doped systems that is absent in Mn_3Sn. We further observe $e-e$ scattering driven resistivity upturn at low temperature with a resistivity minima at 50 K in x=0.35. Fe doping induces magnetic anisotropy such way that the easy magnetisation axis shifts from in-plane in Mn_3Sn to the out-of-plane (z-axis) in x=0.35. Thus, the large uniaxial magnetocrystalline anisotropy in addition to the competing magnetic interactions at low temperature produces nontrivial spin texture which is responsible for the induced low temperature THE with Fe doping. Further, the topological properties of Mn_3Sn are very sensitive to the Fe doping. That means, although Mn_3Sn does not show THE at low temperatures, 8% (x=0.25) of Fe doping shows topological Hall resistivity as high as $5\mu\Omega - cm$ at a critical field of 0.35T and 11.4% (x=0.35) of Fe doping shows topological Hall resistivity as high as $22\mu\Omega - cm$ at a critical field of 4T when measured at 2 K.

Chapter 5

Effect of Electron-Phonon Scattering on the Anomalous Hall Conductivity of Fe_3Sn : a Kagome Ferromagnetic Metal

5.1 Introduction

Hall effect due to which the fast-moving charge carriers get deflected transversely under the external magnetic fields in metals and semiconductors [26] has found lately many real-life technological applications [194, 195]. While an ordinary Hall effect has been noticed in the nonmagnetic metals, an anomalous Hall effect (AHE) was found in the collinear ferromagnetic metals [30, 34] and in the non-collinear antiferromagnetic metals [32, 33, 79]. Moreover, the anomalous Hall effect produces substantially higher Hall resistivity than the ordinary Hall effect, and the field dependent Hall resistivity perfectly scales with magnetization [30, 34]. Though the origin of AHE in non-collinear AFM metals is widely understood by the presence of non-zero Berry phase in momentum space, several mechanisms were proposed to understand the AHE in collinear ferromagnets.

Foremost, Karplus and Luttinger (KL) predicted that the AHE in ferromagnetic metals originates from the interband scattering of the charge carriers under spin-orbit coupling [35], which is recently connected to the Berry curvature of the electronic state of solids [196]. Since the KL theory does not take into account the impurity scattering effects and mainly talks on the intrinsic band structure, considered as the intrinsic theory of AHE. Later on, Smit *et al.,* proposed an extrinsic theory of AHE by incorporating the impurity scattering [37]. The extrinsic AHE happens by two scattering mechanisms, (i) the skew-scattering: whereby the charge carriers scatter asymmetrically by the localized magnetic impurities [37] and (ii) the side-jump: whereby the charge carrier takes a small side jump up on scattering with impurity under spin-orbit coupling [38, 197]. Although many ferromagnetic metals are known to show the AHE [34], the Kagome ferromagnets are quite fascinating systems as they show an intrinsic geometrical frustration, leading to several exotic elec-

---

[0] Results presented in this chapter are published Phys. Rev. B 108, 094404 (2023)

tronic properties such as the flat-bands near the Fermi level [81,82,198–201], quantum spin-liquid ground state [66, 68], Chern insulating state [5, 202], Weyl fermions [61, 203, 204], Dirac fermions [61,65,205], and magnetic topological Skyrmions [44,156], manifesting the anomalous and topological Hall effects.

Thus, the ferromagnetic metal $Co_3Sn_2S_2$ is found to exhibit giant intrinsic anomalous Hall conductivity ($\sigma_{xy} \approx 505$ S/cm) [73] due to the presence of Weyl nodes near the Fermi level [77] and Fe_3Sn_2 is found to show extremely large anomalous Hall conductivity ($\sigma_{xy} \approx$ 1150 S/cm) [206] below 2K and large topological Hall conductivity (-0.875$\mu\Omega$ cm) above room temperature [53, 134]. On the other hand, recently, a few reports on polycrystalline Fe_3Sn suggested it to be a ferromagnetic metal in which the Fe atoms form a Kagome network in the *ab* plane. Further, it was also shown that Fe_3Sn exhibits a large magnetocrystalline anisotropy energy [170, 171] in addition to the anomalous Nernst effect [207]. Although the previous report shows temperature-dependent anomalous Hall conductivity to some extent, a thorough understanding of the anomalous Hall effect in Fe_3Sn is still missing, especially the influence of electron-phonon scattering on the AHC.

Fe_3Sn belongs to the Ni_3Sn-type family of crystal structure with an in-plane Kagome network. Unlike its sister compound Mn_3Sn which is a non-collinear antiferromagnet metal, Fe_3Sn is a collinear in-plane (*ab*-plane) ferromagnetic metal. In this paper, we mainly focus on the anomalous Hall effect of Fe_3Sn as a function temperature. For this, we have grown high-quality single crystals of Fe_3Sn and performed magnetic and magnetotransport studies. Our results unravel two important contributions to the total Hall conductivity of Fe_3Sn. One of them is the temperature independent intrinsic Hall conductivity originated from the electronic band structure and the other one is the temperature dependent extrinsic Hall conductivity originated from the asymmetric skew-scattering. Most importantly, we observe that the extrinsic skew-scattering Hall conductivity strongly depends on the inelastic electron-phonon scattering rate (γ), $\sigma_{zx}^{ext} = \frac{\sigma_{zx0}^{ext}}{(\gamma/\gamma_0+1)^2}$. In addition, the linear dependence of longitudinal electrical resistivity confirms the presence of electron-phonon scattering at higher temperatures. We further show that Fe_3Sn is a soft ferromagnet with an easy-axis of magnetization lying parallel to the *ab* plane. We derive a magnetocrystalline anisotropy energy density as large as 1.02×10^6 J/m^3.

5.2 Experimental details

High quality single crystals of Fe_3Sn were grown by the solid-state crystal growth (SSCG) technique. In SSCG method, the crystals are grown out of polycrystalline matrix. Initially, Fe powder (99.99%, Stern chemicals) and Sn powder (99.995%, Alfa Aesar) were taken in stoichiometric ratio, grounded thoroughly, and heated at 810^{o}C for 7 days. As prepared

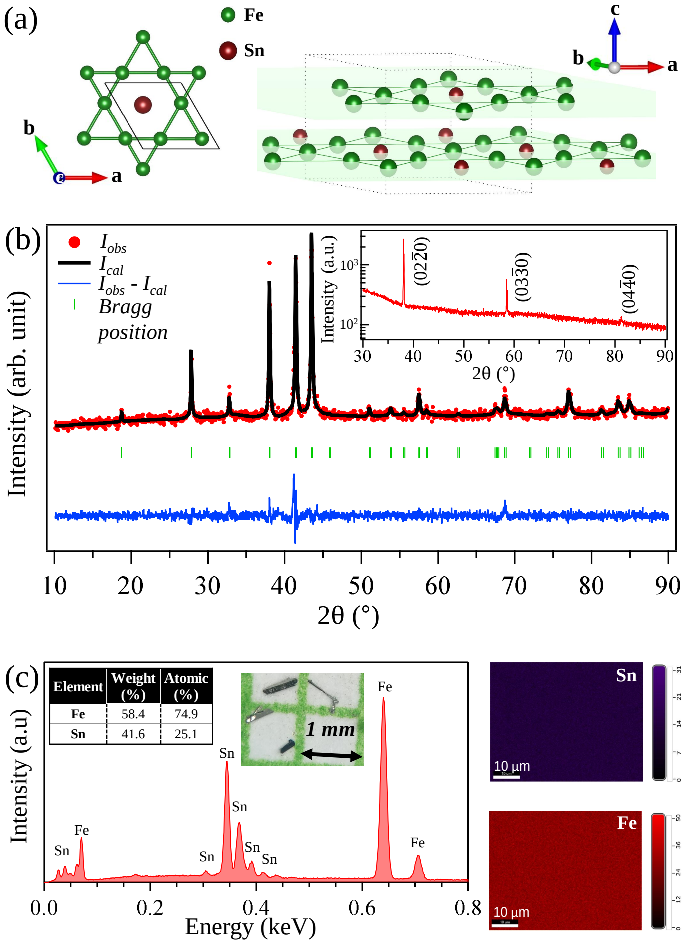

Element	Weight (%)	Atomic (%)
Fe	58.4	74.9
Sn	41.6	25.1

Figure 5.1: (a) Schematic crystal structure and Kagome lattice of Fe_3Sn. (b) Powder XRD pattern of crushed Fe_3Sn single crystals. Inset of (b) shows intensity reflections correspond to (02$\bar{2}$0) Brag planes. Left panel in (c) presents EDS spectra of Fe_3Sn along with tabulated elemental ratios and photographic image showing typical Fe_3Sn single crystals. Right panels in (c) show the elemental mapping of measured single crystal for Fe and Sn.

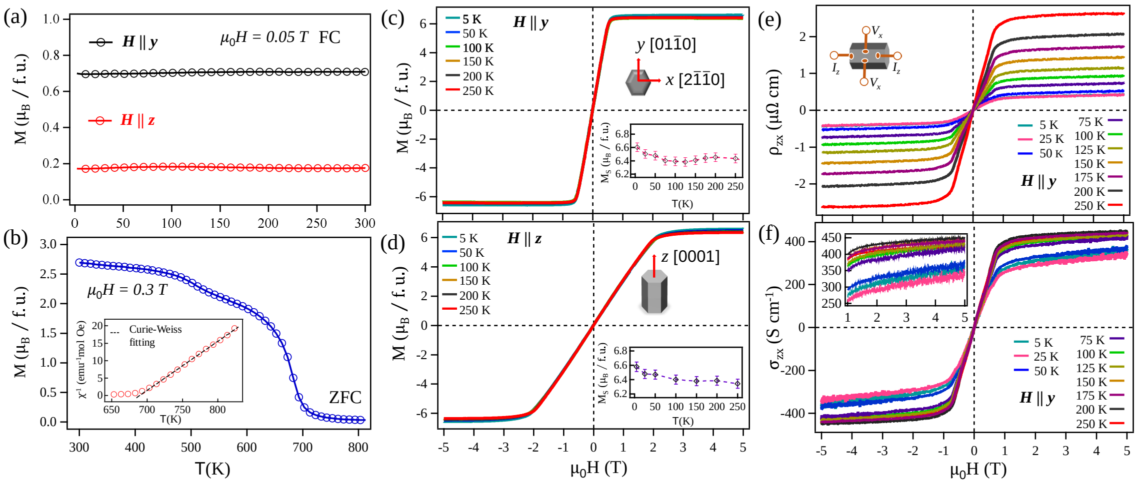

Figure 5.2: (a) and (b) Magnetization measured as a function of temperature on Fe_3Sn single crystals and pellets, respectively. Inset of (b) is Curie-Weiss fitting of inverse susceptibility plotted as a function of temperature. (c) and (d) are the magnetization isotherms $[M(H)]$ for $H \parallel y$ and $H \parallel z$, respectively. Insets in (c) and (d) show the saturation magnetization. (e) and (f) Hall resistivity and Hall conductivity, respectively, plotted as a function of field at various sample temperatures for $H \parallel y$.

Fe_3Sn powder was again grounded and pressed into a pellet which was then annealed at 810°C for another 45 days. Several small rod-shaped shiny crystals with a typical size of 1 mm×0.2 mm×0.2 mm were grown on the surface of the pellet. X-ray diffraction (XRD) technique was performed on a rod-shaped single crystal and on the crushed crystals using Rigaku SmartLab 9kW Cu K_α X-ray source. Elemental analysis was done using the Energy Dispersive X-ray Spectroscopy (EDS of EDAX) suggests an actual chemical composition of $Fe_{2.98}Sn$, which is very close to the nominal composition of Fe_3Sn. For the electrical transport and magnetotransport measurements linear four-probe and Hall probe connections were made, respectively, using the copper wire and silver paint. Magnetic and magnetotransport measurements were carried out on the 9T Physical Properties Measurement Systems (PPMS, Quantum Design-DynaCool) using VSM and ETO options. To eliminate the longitudinal voltage contribution due to any misalignment of the connections, the Hall resistivity was measured by applying both positive and negative magnetic fields and average Hall resistivity was calculated by ρ_H=$\frac{\rho_H(H)-\rho_H(-H)}{2}$.

5.3 Results and Discussions

Fig 6.1(a) depicts schematic crystal structure of Fe_3Sn where the Fe atoms form a Kagome structure with Sn sitting at the center of the Kagome lattice. Fig. 6.1(b) shows the powder XRD pattern of crushed Fe_3Sn single crystals, confirming the hexagonal Ni_3Sn type crystal structure with the space group of P6₃/mmc (No. 194). Inset of Fig. 6.1(b) depicts the

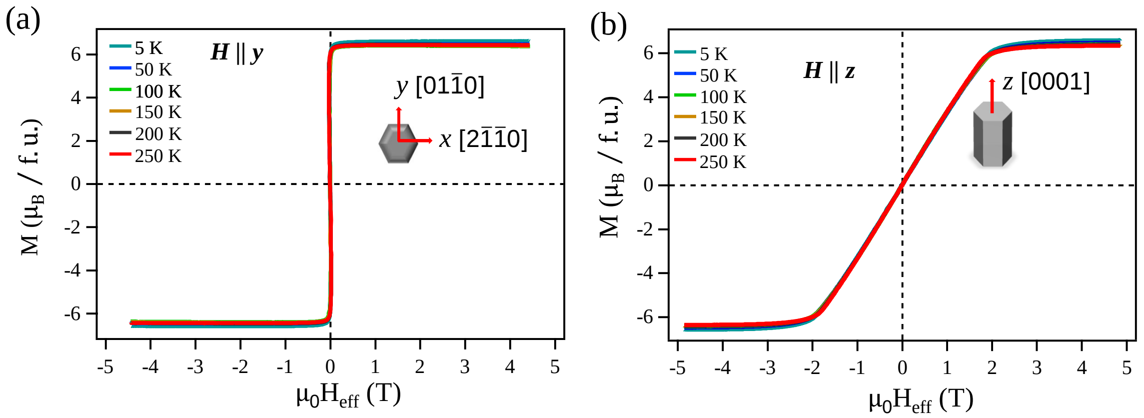

Figure 5.3: Magnetization isotherms $[M(H_{eff})]$ measured at various sample temperatures for $H \parallel y$ (a) and $H \parallel z$ (b). Here, H_{eff} is the effective magnetization field after excluding the shape demagnetizing factor of the approximately rod-shaped sample using the formula, $H_{eff} = H - N_d M$, where N_d is the demagnetization factor. For our rod-shaped sample, the calculated $N_d^{-1} = 2 + \frac{1}{\sqrt{(2)}}\frac{a}{c}$ for $H \parallel y$ is 0.45 and $N_d^{-1} = 1 + 1.6\frac{c}{a}$ for $H \parallel z$ is 0.15 [209]. Here, a=0.2 mm and c=0.7 mm are the sample diameter and length, respectively.

XRD performed on a rod-shaped single crystal, showing intensity of reflections from the (0 2 $\bar{2}$ 0) Bragg plane, suggesting that the length of rod-shaped crystals is parallel to the c-axis. Rietveld refinement performed on the powder XRD of crushed single crystals using the Fullprof software [208] derives the lattice parameters a=b=5.4631(4) and c=4.3552(4), in good agreement with previous reports [170]. Left panel of Fig. 6.1(c) shows the EDS data from which the atomic and weight percentage of the elements are tabulated on the top-left inset of Fig. 6.1(c). Photographic image of typical Fe$_3$Sn single crystals is shown in Fig. 6.1(c). Elemental mapping performed for Fe and Sn using the EDAX is shown in the right-side panel of Fig. 6.1(c), implies good homogeneity of single crystals.

Temperature dependent magnetization $[M(T)]$ between 2 and 300 K performed on Fe$_3$Sn single crystal with the field (H) applied parallel to y-axis ($H \parallel y$) and parallel to z-axis ($H \parallel z$) in the field-cooled mode is shown in Fig. 5.3(a). From Fig. 5.3(a) it is evident that below 300 K, $M(T)$ is completely temperature independent. Fig. 5.3(b) shows $M(T)$ performed between 300 and 800 K on Fe$_3$Sn pellet in the zero-field-cooled mode in order to identify the ferromagnetic transition. From Curie-Weiss fitting of the inverse susceptibility ($\chi^{-1}(T)$), using the formula $\chi = \frac{C}{T-\theta}$, we derive a Curie constant of $C = 7.1 \pm 0.1$ $emu.mol^{-1}$Oe^{-1}K^{-1} and a Curie-Weiss temperature of $\theta = 689 \pm 2$ K, which are consistent with a previous report [170]. The effective magnetic moment of Fe atom in Fe$_3$Sn is found to be μ_{eff}(Fe)=2.51 μ_B using the relation μ_{eff}=2.828 $\sqrt{C}$ [210].

Figs. 5.3(c) and 5.3(d) depict the magnetization isotherms $[M(H)]$ measured at various sample temperatures for $H \parallel y$ and $H \parallel z$, respectively. The saturation field for $H \parallel y$ is around 0.5 T whereas it is 2 T for $H \parallel z$, clearly suggesting that Fe$_3$Sn has an easy-axis of magnetization parallel to the ab-plane. Also, the absence of hysteresis in the $M(H)$ data for the filed applied parallel both directions makes this system a good soft ferromagnet. The saturation magnetic moment per Fe atom is found to be M_s=2.2 μ_B which is close to value of effective magnetic moment μ_{eff}=2.51 μ_B. From the magnetization isotherms shown in Figs. 5.3(c) and 5.3(d), we estimated the magnetocrystalline anisotropic energy density K_u = 1.02×10^6 J/m^3 using the relation $K_u = \mu_0 \int_0^{M_s} [H_y(M) - H_z(M)]\, dM$ after excluding the geometrical demagnetization factor [209]. Here, M_s represents saturation magnetization, H_z and H_y represent $H \parallel z$ and $H \parallel y$, respectively.

Hall resistivity (ρ_{zx}) as a function of field is shown in Fig. 5.3(e) measured at various sample temperatures. Here, the current is applied along the z-axis and the magnetic field is applied along the y-axis to measure the Hall voltage along the x-axis of the crystal as depicted in the inset of Fig. 5.3(e). It is evident from Fig. 5.3(e) that Fe$_3$Sn shows anomalous Hall effect with a little normal Hall effect that is visible at very high temperatures. Next, the Hall conductivity (σ_{zx}) is calculated using the formula $\sigma_{zx} = -\frac{\rho_{zx}}{\rho_{zx}^2+\rho_{zz}^2}$, where ρ_{zz} is the longitudinal resistivity measured along the z-axis of the crystal. Fig. 5.3(f) shows σ_{zx} plotted as a function of field in which we observe a large anomalous Hall conductivity in the range of 410-425 S-cm^{-1} between 75 and 250 K when measured at 5 T, and a sudden drop to 370 S-cm^{-1} is observed upon lowering the sample temperature below 75 K. Though high temperature Hall conductivity obtained in this study is consistent with previous report made on polycrystalline Fe$_3$Sn [207], the low temperature Hall conductivity of 200 S-cm^{-1} at 2 K observed in Ref. [207] is significantly smaller than our findings ($\approx$ 370 S-cm^{-1} at 5 K).

Next, Fig. 5.4(a) depicts temperature dependent longitudinal resistivity (ρ_{zz}) measured with current applied along the z-axis of the crystal. We notice that ρ_{zz} quadratically depends on the temperature ($\rho_{zz} \propto T^2$) up to $\approx$75 K, demonstrating a Fermi-liquid type nature of the resistivity at low temperatures [211]. Nevertheless, above 75 K, ρ_{zz} shows linear depends on the temperature ($\rho_{zz} \propto T$) due to a strong electron-phonon interaction [212]. The temperature dependent resistivity profile of our Fe$_3$Sn single crystal is consistent with previous report on the polycrystalline Fe$_3$Sn [207]. Particularly, the linear dependence of ρ_{zz} above 75 K is in very good agreement with Ref. [207]. Temperature dependent longitudinal conductivity (σ_{zz}) also is shown in Fig. 5.4(a). In general, the total Hall resistivity presented in Fig. 5.3(e) can be expressed by the empirical formula, $\rho_H = \rho_H^N + \rho_H^A$ [34]. Where, the first term represents normal Hall contribution $\rho_H^N = \mu_0 R_0 H$ and the second term represents the anomalous Hall contribution which in turn depends on the magnetization (M) as $\rho_H^A = \mu_0 R_S M$. Here, R_0 and R_S are normal and the anomalous Hall coefficients, respectively. Further, with the help of normal Hall coefficient (R_0) one can calculate the charge carrier (q) density using the relation, $n = \frac{1}{R_0|q|}$. Since the field dependent anomalous Hall effect is

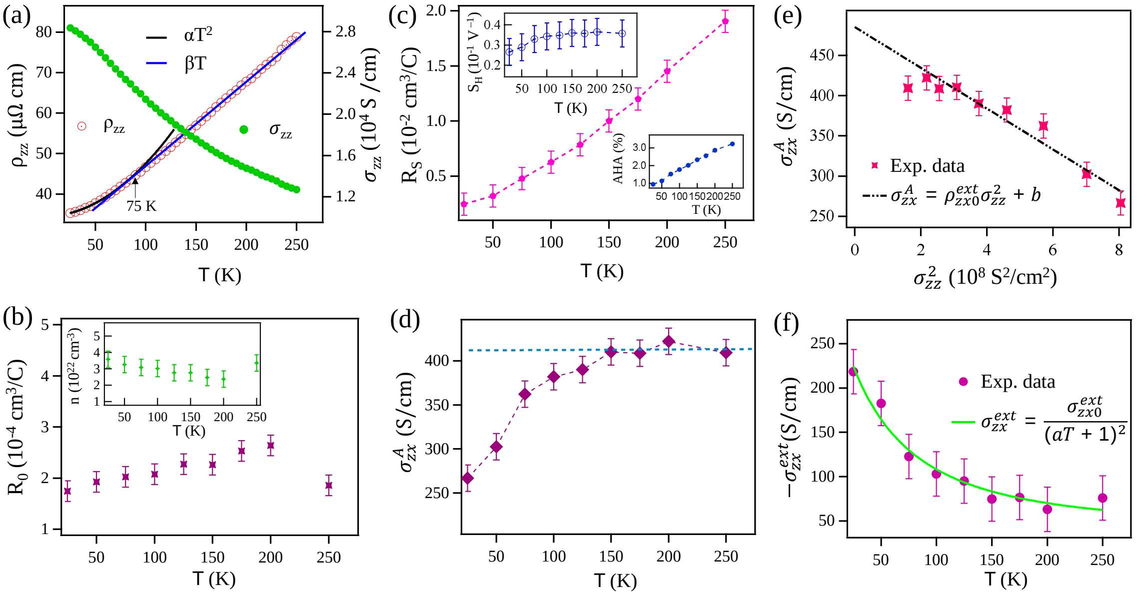

Figure 5.4: (a) Longitudinal electrical resistivity (ρ_{zz}) and electrical conductivity (σ_{zz}) plotted as a function of temperature. (b) and (c) Normal Hall coefficient (R_0) and Anomalous Hall coefficient (R_S) plotted as a function of temperature, respectively. Charge carrier density (n) is shown in the inset of (b). Top inset in (c) shows anomalous Hall scale factor (S_H) and bottom inset in (c) shows anomalous Hall angle percentage (AHA%). (d) Anomalous Hall conductivity (-σ_{zx}^{A}) as a function of temperature. (e) -σ_{zx}^{A} *vs.* σ_{zz}^{2} plot. The dashed line in (e) is a linear fitting using the relation -$\sigma_{zx}^{A} = \rho_{zx0}^{ext}\sigma_{zz}^{2} + b$. (f) Extrinsic anomalous Hall conductivity σ_{zx}^{ext} plotted as a function of temperature. The solid green curve in (f) is a fit with the equation $\sigma_{zx}^{ext} = \frac{\sigma_{zx0}^{ext}}{(aT+1)^2}$.

a replica of magnetization, anomalous Hall resistivity saturates beyond a critical field and becomes almost field independent while the normal Hall resistivity linearly depends with field.

Thus, in order to separate the anomalous Hall resistivity from the normal Hall contribution, we fitted the high field region of the total Hall resistivity with a linear function of field and subtracted the normal Hall contribution from the total Hall resistivity. In this way, we extracted various important parameters such as the normal (R_0) and anomalous (R_S) Hall coefficients. Fig. 5.4(b) depicts R_0 plotted as a function of temperature. The positive R_0 values throughout the measured temperature range as observed in Fig. 5.4(b) suggest hole-carrier dominant electrical transport in Fe_3Sn. Inset of Fig. 5.4(b) demonstrates almost temperature independent hole carrier density (n_h) which is of the order of $\sim 10^{22}\ cm^{-3}$, suggesting Fe_3Sn to be a good metal. Fig. 5.4(c) shows the anomalous Hall coefficient (R_S) plotted a function of temperature. Top-left inset of Fig. 5.4(c) presents the anomalous Hall scaling factor (S_H), defined as $S_H = \frac{-\sigma_{zx}^A}{M} = \frac{\mu_0 R_S}{\rho_{zz}{}^2} (\cong \frac{\rho_{zx}^A}{M\rho_{zz}{}^2})$, plotted as a function of temperature. We observe that S_H is almost temperature independent within the error-bars. Moreover, the value of S_H=0.03±0.01 V^{-1} derived in this study is within the range of 0.01-0.2 V^{-1}, for any typical ferromagnetic metal [213, 214]. Bottom-right inset of Fig. 5.4(c) shows temperature dependent anomalous Hall angle (AHA), defined as the deviation of electron flow from the current direction, is calculated using the formula AHA(%)= $\frac{\sigma_{zx}}{\sigma_{zz}} \times 100(\%)$. We clearly notice that AHA(%)≈3% at 250 K which decreases with temperature. The value of AHA(%)≈3% is close to the AHA values reported on a similar Kagome ferromagnetic system Fe_3Sn_2 (≈1.1%) [214], Kagome antiferromagnetic systems such as Mn_3Sn (≈3.2%) [32] and Mn_3Ge (≈5%) [33], but much smaller than the Shandite Kagome ferromagnet $Co_3Sn_2S_2$ (≈20%) [73].

Several mechanisms were proposed for understanding the anomalous Hall effect in magnetic and nonmagnetic metals. In most of the proposals, the anomalous Hall resistivity (ρ_{zx}^A) is represented mainly by the function of longitudinal resistivity (ρ_{zz}), $\rho_{zx}^A = f(\rho_{zz})$. More explicitly, (i) The intrinsic Karplus-Luttinger mechanism of AHE describes the Hall resistivity $\propto \rho_{zz}^2$ due to the interband scattering in presence of strong spin-orbit coupling [35], (ii) The extrinsic side-jump mechanism of AHE describes the Hall resistivity $\propto \rho_{zz}^2$ due to side-jump scattering of charge carriers at the impurities [38], (iii) The extrinsic skew-scattering mechanism of AHE describes the Hall resistivity $\propto \rho_{zz}$ due to skew-scattering of charge carrier at the impurities [37], (iv) a ρ_{zz}^{α} $(1 < \alpha < 2)$ dependency of ρ_{zx}^A was proposed in the case of bad metals [215]. For our case, the mechanism (iv) can be ignored as the longitudinal conductivity of Fe_3Sn is found to be σ_{zz}=31.4 $\frac{e^2}{hc}$ (where c is the lattice constant) which is in the metallic regime [216]. Recently, a new mechanism (TYJ) was proposed by Tian *et. al.* [217] in order to understand the AHE in ferromagnetic metals. According to TYJ theory, the anomalous Hall resistivity is described by $\rho_{zx}^{A} = f(\rho_{zz0}, \rho_{zz})$ which includes the residual resistivity (ρ_{zz0}). Thus, following the TYJ theory [217, 218], the anomalous Hall resistivity takes the form $\rho_{zx}^{A} = (\alpha\rho_{zz0} + \beta\rho_{zz0}^{2}) + b\ae_{zz}^{2}$ and the anomalous Hall conductivity is represented by $-\sigma_{zx}^{A} = (\alpha\sigma_{zz0}^{-1} + \beta\sigma_{zz0}^{-2})\sigma_{zz}^{2} + b = \rho_{zx0}^{ext}\sigma_{zz}^{2} + b$. Here, α and β are real constants, $\sigma_{zz0} = 1/\rho_{zz0}$ is the residual conductivity, and b is the intrinsic Hall conductivity originated from the momentum space Berry curvature. It is well known that the intrinsic Hall conductivity (b) is usually temperature independent [34, 73] except for the systems showing electronic or magnetic phase transitions [118, 196]. Since Fe_3Sn shows neither electronic nor magnetic transition within the measured temperature range of 2-250 K, change in the Berry phase is not expected. From Fig. 5.4(d), we notice that the anomalous Hall conductivity is almost constant at higher temperatures, but decreases below 150 K. To understand this phenomenon, we employed TYJ mechanism to fit the data of -σ_{zx}^{A} *vs.* σ_{zz}^{2} as shown in Fig. 5.4(e), demonstrating a good fitting within the error-bars. From the fitting , we extracted intrinsic Hall conductivity b=485± 60 S/cm that is close to the previously reported values on polycrystalline Fe_3Sn ($\approx$ 500 S/cm) [207] and predicted by a theoretical calculation ($\approx$ 600 S/cm at E_F) [219].

Next, Fig. 5.4(f) shows the extrinsic Hall conductivity (σ_{zx}^{ext}) extracted from the total conductivity by subtracting the intrinsic Hall contribution (b). From Fig. 5.4(f), it is evident that the extrinsic Hall conductivity decreases with increasing sample temperature. Further, the sign of extrinsic Hall conductivity is opposite to the intrinsic Hall conductivity, resulting into the reduced total Hall conductivity at lower temperatures. As we know, in the clean limit, for $\hbar/\tau \rightarrow 0$ (τ is the relaxation time) the extrinsic skew-scattering contribution diverges [220]. On the other hand, from Fig. 5.4(f), we can see that as the sample temperature decreases the extrinsic Hall conductivity rapidly increases. This observation indicates that skew-scattering playing a major role to generate the anomalous Hall conductivity in Fe_3Sn. The longitudinal resistivity (ρ_{zz}) suggests electron-phonon scattering at higher temperatures in this system. In order to understand the phonon influence on the anomalous Hall conductivity, we employed the mechanism proposed by Shitade and Nagaosa [216] which involves the electron-phonon inelastic scattering rates (γ). In this mechanism, the extrinsic Hall conductivity decays with γ following the relation $\sigma_{zx}^{ext} = \frac{\sigma_{zx0}^{ext}}{(\gamma/\gamma_0+1)^2}$. Since the inelastic scattering rate is proportional to the longitudinal resistivity [$\gamma \sim (\rho_{zz} - \rho_{zz0})$] and $\rho_{zz} - \rho_{zz0}$ linearly depends on temperature [$(\rho_{zz} - \rho_{zz0}) \propto T$] above 75 K [see Fig. 5.4(a)], we can rewrite the equation as $\sigma_{zx}^{ext} = \frac{\sigma_{zx0}^{ext}}{(aT+1)^2}$. Here, $a = 0.011 \pm 0.003\ \mathrm{K}^{-1}$ represents the measure of inelastic electron-phonon scattering strength. In this way, we could fit the σ_{zx}^{ext} data very well as shown in Fig. 5.4(f). Thus, our results clearly demonstrate the influence of electron-phonon interaction on the extrinsic skew-scattering anomalous Hall conductivity which decreases with increasing temperature. Finally, we would like to mention here that during the course of our manuscript preparation a preprint on the magnetic studies of Fe_3Sn single crystals has appeared [221]. The magnetic properties presented in their study are consistent with our findings. Particularly, the magnetocrystalline anisotropy energy density of $1.23 \times 10^6\ J/m^3$ reported in Ref. [221] is in good agreement with the value of 1.02×10^6 J/m^3 found in this study.

5.4 Summary

In summary, we have successfully grown high quality single crystals of Fe_3Sn. In this study, we mainly focussed on understanding the anomalous Hall effect as a function temperature. Our results unravel two main contributions to the total Hall conductivity of Fe_3Sn. One of them is the temperature independent intrinsic Hall conductivity originated from the electronic band structure and the other one is the temperature dependent extrinsic Hall conductivity due to the asymmetric skew-scattering. Most importantly, we find that the extrinsic skew-scattering Hall conductivity is significantly influenced by the electron-phonon scattering at higher temperatures and obeys the relation $\sigma_{zx}^{ext} = \frac{\sigma_{zx0}^{ext}}{(aT+1)^2}$. In addition, the longitudinal electrical resistivity (ρ_{zz}) confirm the presence of electron-phonon scattering as the resistivity linearly depends on the temperature. We show that Fe_3Sn is a soft ferromagnet with easy-axis magnetization lying parallel to the *ab* plane. We estimate a magnetocrystalline anisotropic energy density as large as 1.02×10^6 J/m^3 in Fe_3Sn.

Chapter 6

Anisotropic Nonsaturating Magnetoresistance Observed in $HoMn_6Ge_6$: A Kagome Dirac Semimetal

6.1 Introduction

The combination of frustrated magnetism, strong electronic correlations, and quantum topology in the kogome systems immensely attracts the researchers from the fundamental sciences and potential technological applications points of view [100,222–228]. Particularly, the interplay among these peculiar physical properties in the kagome lattice features intriguing quantum phenomena including the quantum spin liquid phase [229–232], flat bands [74, 81,198,200], Dirac and Weyl fermions [32,73,74,79,206,233], Chern quantum phase [72, 234], and Skyrmionic lattice [52,235]. So far, the transition metal-based kagome systems have been extensively explored to find the Weyl fermions in Mn_3Sn(Ge) [79, 80], giant anomalous Hall effect in $Co_3Sn_2S_2$ [73], Nernst effect in Fe_3Sn [207], Skyrmion lattice in Fe_3Sn_2 [53]. On the other hand, the recent discovery of a nearly ideal quantum limit Chern magnet with massive Dirac fermion in $TbMn_6Sn_6$ has ignited an intense search for the rare-earth based kagome systems [72].

Following this discovery, several experimental reports appeared discussing the tuning of topological properties in RMn_6Sn_6 (R = Gd-Tm, Lu) [76], large anomalous Hall effect in RMn_6Sn_6 (R = Tb, Dy, and Ho) [236], Chern magnetic state in $TbMn_6Sn_6$ [72], Dirac-like band crossings in $HoMn_6Sn_6$ [237], linear unsaturated magnetoresistance in RMn_6Sn_6 (R = Gd, Tm, Lu) [76]. Among these, $HoMn_6Sn_6$ is a ferrimagnetic metal in which the spins of the Ho-4f sub-lattice align antiferromagnetically with spins of Mn-3d sub-lattice. Thus, the interplay between the ferrimagnetism and the electronic band structure plays a vital role in shaping the linear non-saturated magentoresistance of these systems [76,237,238]. On the other hand, though $HoMn_6Ge_6$ shares similar crystal of $HoMn_6Sn_6$, no systematic study is available on $HoMn_6Ge_6$ in detail discussing the magnetotransport properties.

---

[0] Results presented in this chapter are accepted in Phys. Rev. B (in press).

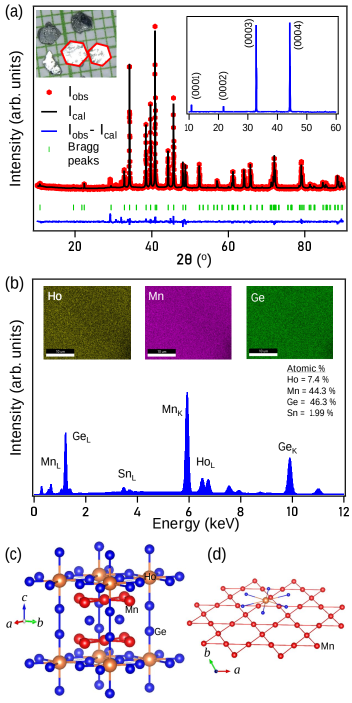

Figure 6.1: (a) Powder XRD pattern taken on the crushed singles crystals of $HoMn_6Ge_6$ overlapped with Rietveld refinement. The left inset in (a) shows optical image of as-grown single crystals. The right inset in (a) represents the XRD pattern corresponding to (000l) Bragg planes of the $HoMn_6Ge_6$ single crystal. (b) EDXS data taken on $HoMn_6Ge_6$ single crystal. Insets in (b) show the elemental mapping of Ho, Mn, and Ge atoms. (c) Schematic representation of the primitive unit cell of $HoMn_6Ge_6$. (d) Kagome lattice plane formed by the Mn atoms when projected onto the *ab*-plane.

$HoMn_6Ge_6$ crystallizes into $HfFe_6Ge_6$-type hexagonal structure with the space group $P6/mmm$, orders antiferromagnetically at a Néel temperature of 466 K [239]. The magnetic moments of Mn and Ho are arranged in a skew-spiral fashion and the plane of magnetic moments (Ho and Mo) is angled at 60^o with the z-axis in $HoMn_6Ge_6$ [240], whereas in RMn_6Sn_6 systems the moments of R and Mn are aligned antiparallelly to form a ferrimagnetic structure having an easy-axis of magnetization angled with z-axis. The angle between the z-axis and the easy-axis of magnetization strongly depends on the rare-earth element [240]. Furthermore, the magnetic structure of these systems is very sensitive to the sample temperature [241]. For instance, in the low-temperature region ($<$ 55 K), the Ho and Mn magnetic moments form a skew-spiral ($\widetilde{SS}$) structure, coupled antiferromagnetically, with a plane of moments making an angle θ_S with the z-axis, producing finite net magnetization along both the in-plane and out-of-plane directions. But as the temperature is increased the skew-spiral structure gets distorted and other magnetic transitions emerge at 220 and 260 K. Beyond 260 K, the $\widetilde{SS}$ structure completely gets destroyed and the system enters into an antiferromagnetic state are around 300 K.

In this work, high-quality single crystals of $HoMn_6Ge_6$ were grown using the Sn flux to study the magnetic and magnetotransport properties. Electrical resistivity demonstrate an overall metallic nature throughout the measured temperature range with a few magnetic transition-driven anomalies. A crossover from negative to positive magnetoresistance (MR) is observed at a critical temperature of 150 K. While the linear nonsaturating positive MR exits in the low-temperature region mainly driven by the Dirac-like linear band dispersion, the negative MR observed in the higher temperature region is due to the spin-flop type magnetic transition. Most importantly, we identify a large anisotropy in the magnetoresistance due to the anisotropic Fermi surface present in this system. Further, we observe anomalous Hall effect in addition to a switching of dominant charge carriers from electrons to holes at around 220 K, ingoing from high temperature to low temperature. Also, we performed density functional theory calculations on $HoMn_6Ge_6$ by considering the skew-spiral magnetic structure that is experimentally obtained [241] for a better understanding of our magnetotransport data.

6.2 Experimental and First-principles Calculation Details

Single crystals of $HoMn_6Ge_6$ were grown using Sn flux. Firstly, Holmium (Ho) chunk (Alfa Aesar, 99.9%), Manganese (Mn) powder (Alfa Aesar, 99.95%), Germanium (Ge) powder (Alfa Aesar, 99.99%), and Tin (Sn) shots (Alfa Aesar, 99.995%) were weighed in the ratio of 1 : 6: 6: 24. The mixture was kept in an alumina crucible and sealed the crucible together with the mixture inside an evacuated quartz ampoule. The mixture was heated up to 1000^oC at a rate of 50^o/hr and kept there for another 18 hrs before cooling the molten mixture down to 600^oC at a rate of 5^oC/hr. Finally, the molten is annealed for another two days at 600^oC. Then, the ampoule was quickly transferred to a centrifuge to separate the Sn flux from the samples. In this way, we obtained several hexagonal-shaped $HoMn_6Ge_6$ single crystals with a typical size of 2mm × 2mm × 0.4mm as shown in the inset of Fig. **??**(a). X-ray diffraction (XRD) was done on flat-shaped single crystals and as well on the powders of crushed crystals using Rigaku SmartLab with 9 kW Cu K_α x-ray source. The exact chemical composition of the as-grown single crystals was found using the energy dispersive x-ray spectroscopy (EDXS). The electrical resistivity and magnetotransport measurements were measured with the four-probe and Hall-probe connections. Electrical, magnetic, and magnetotransport measurements were carried out in the 9 T physical properties measurement system (PPMS, DynaCool of Quantum Design) using the VSM and ETO options. To eliminate the longitudinal voltage contributions due a possible misalignment of the Hall connections, the Hall resistivity was calculated using the relation $\frac{\rho_H(H)-\rho_H(-H)}{2}$.

To understand the magnetotransport properties, the electronic band structure of $HoMn_6Ge_6$ was calculated using the density-functional theory (DFT) within the Perdew-Burke-Ernzerhof-type generalized-gradient approximation (GGA) [242] as implemented in the Quantum Espresso (QE) simulation package [243]. The electronic wavefunction is expanded using plane waves up to a cutoff energy of 100 Ry. Brillouin zone sampling is done over a $10\times10\times6$ Monkhorst-Pack k-grid. The crystal structure was optimized through the variable-cell relaxation method as implemented in QE. Notably, the non-collinear skew-spiral magnetic structure was considered to determine the ground state electronic properties. The band structure was produced with and without considering the spin-orbit coupling (SOC).

6.3 Results and Discussions

Figure 6.1(a) depicts x-ray diffraction (XRD) pattern of the crushed $HoMn_6Ge_6$ single crystals overlapped with Rietveld refinement performed using the Fullprof software. The Rietveld refinement confirms that $HoMn_6Ge_6$ crystallizes into the hexagonal kagome $HfFe_6Ge_6$-type crystal structure with a space group of $P6/mmm$ (No. 191). The refined lattice parameters are $a = b = 5.2415(5)$ and $c = 8.1831(4)$. The right-inset in Fig. 6.1(a) shows the XRD pattern taken on the flat surface of the single crystal, confirming that the crystal growth plane is parallel to (0001)-plane direction. Fig. 6.1(b) depicts the EDXS data conforming the exact chemical composition of the sample $Ho_{0.96}Mn_{5.74}Ge_6$. For convenience, hereafter we represent it by the nominal composition of $HoMn_6Ge_6$. Since the crystals were grown out of Sn flux, the crystals were found with a maximum 2% of Sn impurity. The elemental mappings done for Ho, Mn, and Ge as shown in the top insets of Fig. 6.1(b) imply a good homogeneity of the studied single crystals.

Longitudinal electrical resistivity [$\rho_{xx}(T)$] is plotted as a function of temperature, as shown in Fig. 6.2(a), measured without magnetic field (red-colored data) and with $\mu_0 H = 9$ T of magnetic field (blue-colored data) applied parallel to the z-axis [0001]. The low-temperature resistivity ($<$ 100 K) can be reasonably fit with the quadratic equation of the Landau Fermi-liquid theory, $\rho_{xx}(T) = \rho_0 + \alpha T^2$. Here, $\rho_0 = 8.42\ \mu\Omega - cm$ is the residual resistivity due to impurity scattering and $\alpha = 2 \times 10^{-9}\ \mu\Omega - cm/K^2$ is the electron-electron scattering coefficient. Further, in the resistivity data ($\mu_0 H = 0$ T) we observe *kinks* at $T_1 \approx 260$ K and $T_2 \approx 220$. The transition temperatures T_1 and T_2 shift towards higher temperatures under the external magnetic fields. For instance, at a field of 9 T, the transition temperature T_1 shifted beyond 300 K which we could not identify, while the transition temperature T_2 shifted to 245 K. This observation clearly indicates the magnetic origin of the *kinks*. Fig. 6.2(b) depicts the magnetoresistance percentage

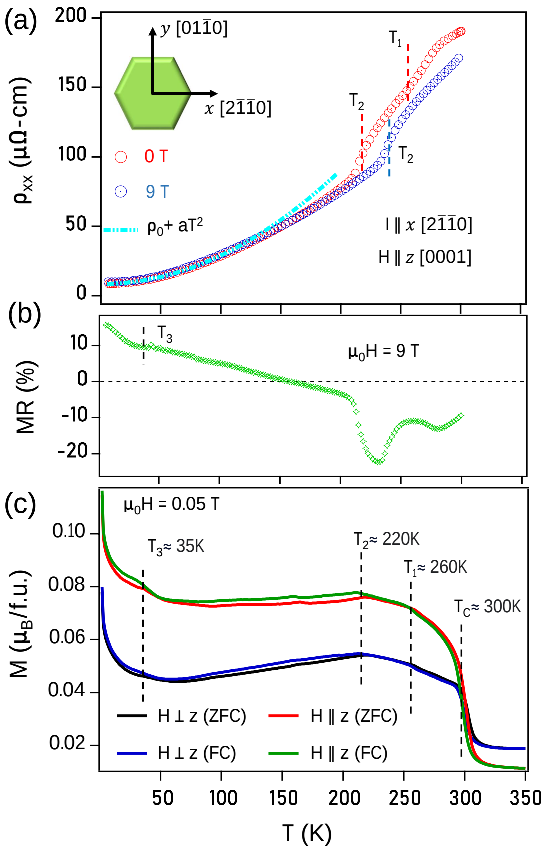

Figure 6.2: (a) Longitudinal resistivity ρ_{xx} plotted as a function of temperature with current applied along x $[2\bar{1}\bar{1}0]$-axis for both 0 T (red curve) and 9 T (blue curve) fields applied along z $[0001]$-axis of the crystal. (b) Magnetoresistance MR(%)= $\frac{\rho_{xx}(9T)-\rho_{xx}(0T)}{\rho_{xx}(0T)} \times 100(\%)$ plotted as a function of temperature. (c) Magnetization plotted as a function of temperature $[M(T)]$ for both $H \parallel z$ and $H \perp z$ directions measured under field-cooled and zero-field-cooled modes with $\mu_0 H = 0.05$ T.

$[MR\% = (\rho_{xx}(T,H) - \rho_{xx}(T,0))/\rho_{xx}(T,0)]$ plotted as a function of temperature from which another transition is identified at $T_3 \approx 35$ K though it is not clearly visible from the $\rho_{xx}(T)$ data [see Fig. 6.2(a)]. Overall, the longitudinal electrical resistivity shows metallic nature throughout the measured temperature range with a residual resistivity ratio (RRR) of ρ_{xx}(300K)/ρ_{xx}(2K) $\approx$ 20.

Fig. 6.2(c) presents the magnetization plotted as a function of temperature $[M(T)]$ under the magnetic field $\mu_0 H = 0.05$ T applied parallel ($H \parallel z$) and perpendicular ($H \perp z$) to the z-axis, measured both in the field-cooled (FC) and zero-field-cooled (ZFC) modes. Clear overlapping between FC and ZFC data suggests that the magnetic moments are thermally reversible in the system throughout the measured temperature range of 2 - 350 K. On the other hand, previous neutron diffraction study on similar system revealed a complex magnetic structure with different magnetic states at different temperatures [241]. For instance, in the low-temperature region (< 55 K), the Ho and Mn magnetic moments form a

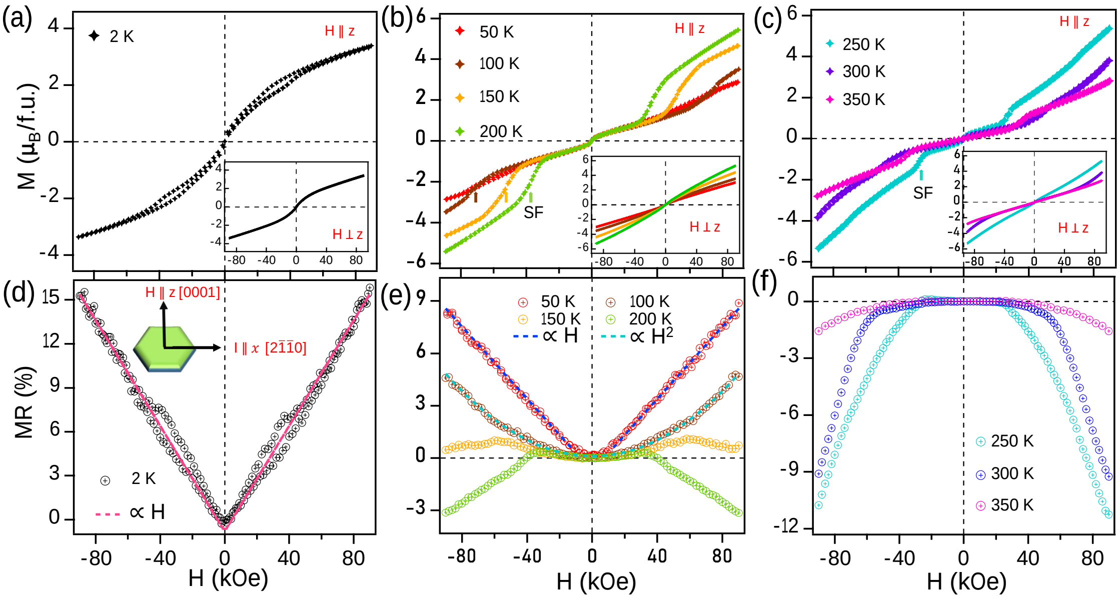

Figure 6.3: (a),(b), and (c) Isothermal magnetization $M(H)$ measured at different temperatures for the fields applied parallel to the z-axis ($H \parallel z$). Insets in (a)-(c) show same for $H \perp z$. (d),(e), and (f) Field dependent magnetoresistance [MR(%)= $\frac{\rho_{xx}(H)-\rho_{xx}(0)}{\rho_{xx}(0)} \times 100(\%)$] measured for different temperatures.

skew spiral ($\widetilde{SS}$) structure, coupled antiferromagnetically, with a plane of moments making an angle θ_S with the z-axis [see Fig. 6.6(b)], producing finite net magnetization along both the in-plane and out-of-plane directions. Between 55 and 220 K, both wave vector (q) and phase angle (ϕ_S) increase monotonically with temperature. In the 220-260 K region, the $\widetilde{SS}$ structure gets distorted, accompanied by the Mn spin-reorientation, and thus eventually leading to a weak ferromagnetism at 300 K. Beyond 300 K the skew-spiral structure becomes a cycloid. In line with previous studies [241, 244, 245] we also observe magnetic transitions in the magnetization data at $T_1 \approx 260$ K, $T_2 \approx 220$ K, and at $T_3 \approx 35$ K. Further, a weak ferromagnetic-like magnetization jump is noticed at $T_C \approx 300$ K which is in agreement with Ref. [241, 244] except for that the signal is relatively stronger in our case. As can be seen from Fig. 6.2(c), the out-of-plane magnetization ($H \parallel z$) dominates the in-plane magnetization ($H \perp z$) below 300 K, while the in-plane magnetization dominates the out-of-plane magnetization above 300 K. This observation hints at the fluctuating magnetic moments across the T_C.

Next, Figs. 6.3(a), 6.3(b), and 6.3(c) depict magnetization isotherms [$M(H)$] measured at different temperatures for $H \parallel z$ and $H \perp z$. We observe a weak ferromagnetic-like $M(H)$ data when measured at 2 K for both $H \parallel z$ and $H \perp z$ at lower field region without magnetization saturation. Further field-induced hysteresis is visible for $H \parallel z$ between 2 and 4 T, but not for $H \perp z$ possibly due to the out-of-plane spin canting within this field

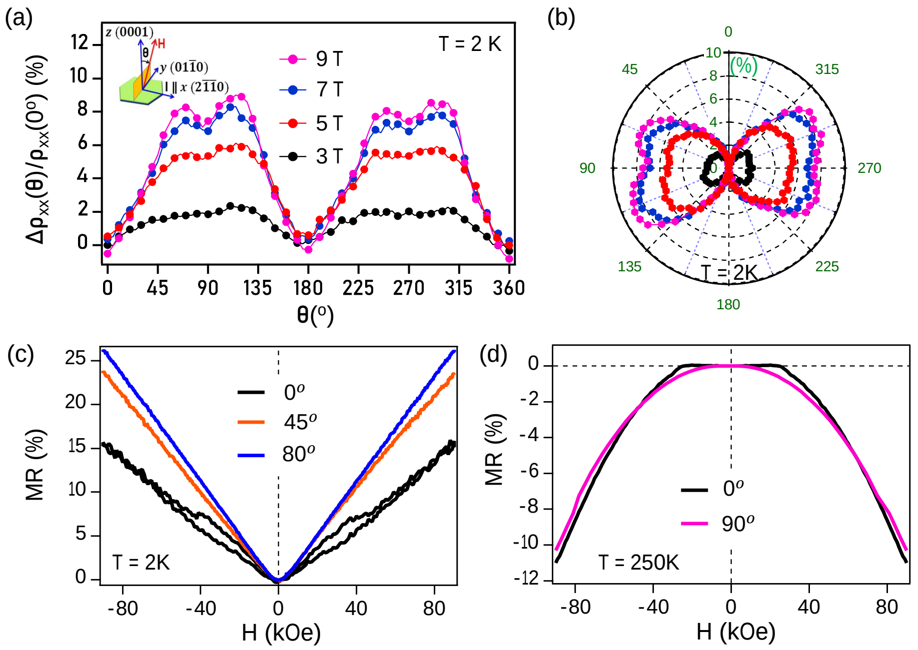

Figure 6.4: (a) Angle dependent magnetoresistance [ADMR(%) $= \frac{\rho_{xx}(\theta)-\rho_{xx}(0^o)}{\rho_{xx}(0^o)} \times 100(\%)$] measured for various applied fields at 2 K. Inset in (a) is a schematic showing the ADMR measuring geometry. Here θ is the angle between z-axis and the applied field direction. (b) is same as (a) but plotted in polar coordinates for a better visualization. In (b) radius is the amplitude of ADMR(%). (c) Field dependent magnetoresistance (MR) measured at 2 K for different θ values. (d) is same as (c) but measured at 250 K of the sample temperature.

range. This type of metamagnetic state is not observed at higher temperatures, instead, an out-of-plane spin-flop transition has been found at a critical field (H_{SF}) that is temperature dependent, due to which a sudden increase in magnetization noticed [see Figs. 6.3(b) and(c)]. That means, we noticed the spin-flop type transition at the critical field $H_{SF} \approx$ 6.5 T, 5.8 T, 3.5 T, and 2.8 T when measured at the temperatures 100 K, 150 K, 200 K, and 250 K, respectively. However, no significant spin-flop transition is noticed at 300 and 350 K. Also, spin-flop transition is absent from the in-plane magnetization ($H \perp z$) at any measured temperature.

Isothermal magnetoresistance (MR) at different sample temperatures and with the fields applied parallel to the z-axis are shown in Figs. 6.3(d), 6.3(e), and 6.3(f). Fig. 6.3(d) demonstrates the MR measured at 2 K, where the MR is linear dependent (red-dashed line) on the applied filed in addition to the hysteresis between the fields 2 and 4 T that is originated from the field-induced metamagnetic state [Fig. 6.3(a)]. From Fig. 6.3(e), we can see that the linear dependency of MR is intact up to 50 K. But at 100 K, we observe a classical parabolic magnetoresistance. Though this parabolic nature is sustained at higher temperatures (150 and 200 K) as well, but beyond the spin-flop (H_{SF}) transition the MR starts to

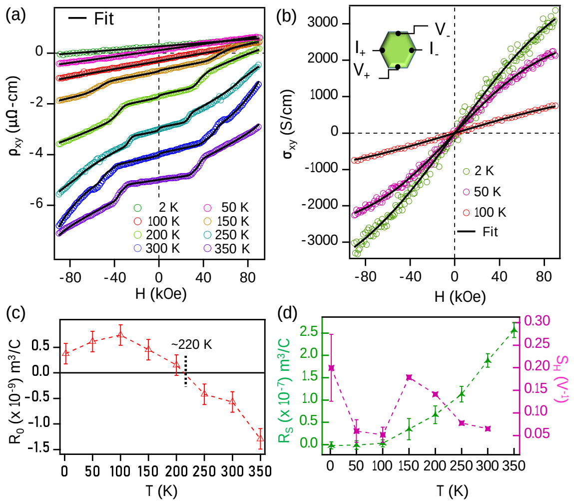

Figure 6.5: (a) Field dependent Hall resistivity ρ_{xy} measured for different sample temperatures overlapped with the fits (black curves). (b) Field dependent Hall conductivity σ_{xy} plotted for 2, 50, and 100 K of sample temperatures. Inset in (b) schematically shows the Hall effect measuring geometry. (c) Normal Hall coefficient (R_0) plotted as a function of temperature. (d) Anomalous Hall coefficient (R_S) [left axis] and anomalous Hall scaling factor (S_H) [right axis] plotted as a function of temperature.

decrease with increasing the field for a given temperature. Eventually, beyond the H_{SF} the MR becomes negative above 150 K, consistent with the MR(T) data shown in Fig. 6.2(b) in which we can notice negative MR above 150 K when measured with 9 T. However, the MR becomes nearly field independent as the temperature reaches 350 K.

Overall, $HoMn_6Ge_6$ shows a complex temperature dependent MR. Importantly, up to 50 K it shows a positive nonsaturating MR that is linearly depending on the applied field. There exist several mechanisms explaining the linear MR, such as (i) the presence of linear dispersive Dirac-like bands with very low effective mass near the Fermi level in the case of topological materials [246, 247], (ii) quasi-random resistor network model in the case of metal–semiconductor composites [248, 249], and (iii) carrier density fluctuations due to irregular current paths from the inhomogeneous or grain boundaries in the case of disordered systems [250, 251]. We can safely rule out the (ii) mechanism as our system is not a metal-semiconductor composite. Also, since our studied system is in the single crystalline form with no significant grain boundaries and with good homogeneity, we can rule out the mechanism (iii) also as the origin of linear MR. Previous reports on its sister compounds RMn_6Sn_6 suggested that the linear MR could originate from the Dirac-like linear bands [76]. In addition, previous band structure calculations on these systems showed several Dirac-like linear band dispersions crossing the Fermi level [240, 252]. To confirm that the linear MR originates from the linear Dirac-like topological band structure, we performed density functional theory (DFT) calculation as discussed later explicitly.

Further, we measured the angle-dependent magnetoresistance (ADMR) with the current and field directions kept always perpendicular to each other such that only the field direction changes with the crystal axes as shown in the schematic of Fig. 6.4(a). The angle-dependent magnetoresistance is calculated as $\frac{\rho_{xx}(\theta)-\rho_{xx}(0^o)}{\rho_{xx}(0^o)}$(%) while the applied magnetic field is kept constant. As can be seen from Fig. 6.4(a), at 2 K the MR is positive for all the applied magnetic fields but very sensitive to the field angle, suggesting a strong anisotropic MR in this system. Specifically, MR is minimum at the angles of 0°, 180°, and 360° and it is maximum at the angles 60°, 120°, 240°, and 300°. Also, the saddle points in the ADMR are observed at 90° and 270° for all the applied fields. For a better visualization, we plotted the ADMR in polar coordinates as shown in Fig. 6.4(b), from which we can clearly observe a butterfly pattern for the out-of-plane MR at 2 K. Worth to mention here that the ADMR measured at 250 K is negligibly small (not shown) compared to the ADMR taken at 2 K. Next, Fig. 6.4(c) depicts the field-dependent MR plotted for different field angles (0°, 45°, and 80°) measured at 2 K, from which we observe linear MR at all field angles. Moreover, we see that the MR reaches almost 25% for θ =80^0 and the hysteresis which was present for $\theta = 0$ has vanished at the other two angles. Fig. 6.4(d) depicts filed dependent MR taken at 0° and 90° filed angles, from which we observe the absence of spin-flop transition effect on the MR when measured at 90°, consistent with $M(H)$ for $H \perp z$.

Next, Fig. 6.5(a) demonstrate field-dependent Hall resistivity [$\rho_{xy}(H)$] measured at different sample temperatures. We see deviation in the Hall resistivity, leading to anomalous Hall effect, at the spin-flop transition temperature. Usually, in ferromagnets, the Hall resistivity can be expressed by $\rho_H = R_0\mu_0 H + R_S\mu_0 M$ [34], where R_0 is the ordinary Hall coefficient and R_S is the anomalous Hall coefficient. Although the anomalous Hall effect (AHE) mainly appears in ferromagnets, recently it has been widely observed in non-collinear antiferromagnets as well [32, 253–255]. From our Hall resistivity data, we can see that the anomalous Hall effect is induced from spin-flop transition that is resembling the $M(H)$ data shown in Figs. 6.3(a)-(c). Moreover, the above formula can be rewritten as $\frac{\rho_H}{\mu_0 H} = R_0 + R_S\frac{M}{H}$ which imitates a linear equation and intercept on the y-axis gives R_0 and slope gives the anomalous Hall coefficient R_S. Using this formalism, we have reasonably fitted the Hall resistivity as depicted in Fig. 6.5(a). The anomalous scaling factor (S_H) is calculated using the formula $S_H = \mu_0 R_S/\rho_{xx}^2$, where ρ_{xx} is the longitudinal resistivity. Fig. 6.5(c) depicts the normal Hall coefficient (R_0) plotted as a function of temperature. From Fig. 6.5(c), we further notice R_0 changing from positive to negative at around 220 K which indicates hole-type (electron-type) carrier dominance below (above) 220 K.

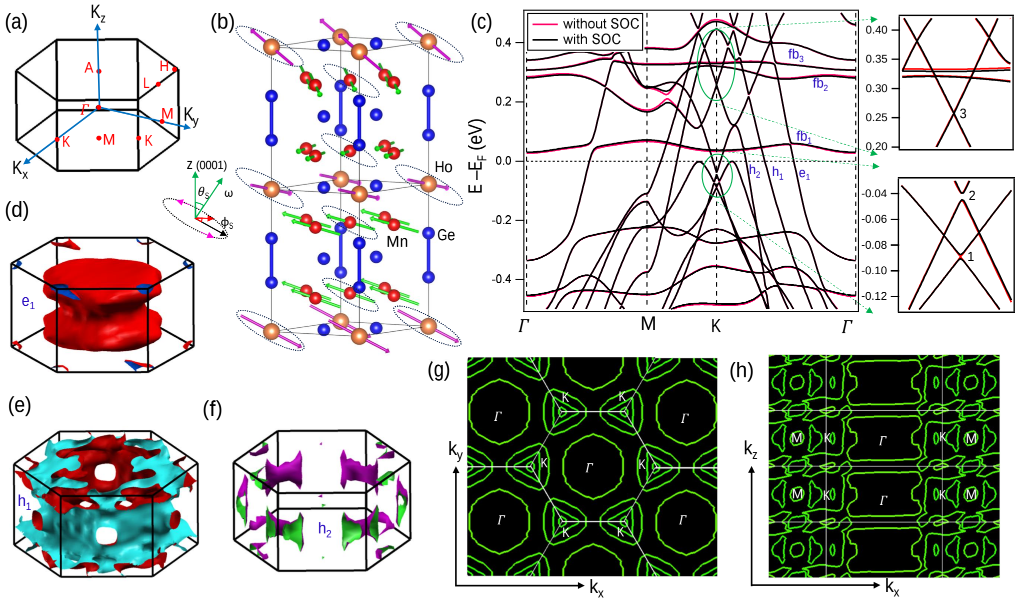

Figure 6.6: (a) Hexagonal Brillouin zone showing the positions of various high symmetry points. (b) Low temperature skew-spiral ($\widetilde{SS}$) magnetic structure of HoMn$_6$Ge$_6$ [241]. Here, $\theta_s = 60^o$ and $\phi_s = 71.2^o$. (c) Electronic band structure of HoMn$_6$Ge$_6$ calculated for the magnetic configuration shown in (b) with (black-colored) and without (red-colored) including the spin-orbit coupling (SOC). The right-side panels of (c) show the zoomed-in band structure to clearly see various Dirac points. (d), (e), and (f) show the calculated Fermi surface maps in three-dimensional. (g) and (h) show the constant energy contours taken at the Fermi level in the $k_x - k_y$ and $k_x - k_z$ momentum planes, respectively.

As discussed above, a magnetic transition exists at around 220 K (T_2). It is possible that the change in magnetic structure influences the electronic structure near the Fermi level and thus the switching of charge carrier type at 220 K. This observation suggests a strong correlation between the magnetic and electronic structures in these systems. Moreover, the value of R_S decreases rapidly with decreasing temperature and becomes negligibly small below 100 K. Whereas the S_H varies between 0.05 and 0.2 like in a typical ferromagnetic metal [34,214]. Further from the relation $\mu_0 R_S = S_H \rho_{xx}^2$, it is clear that for very low resistivity ρ_{xx} values the contribution from AHE (R_S) is negligible so that only the ordinary Hall effect dominates at low temperatures. In Fig. 6.5(b) we have plotted the Hall conductivity as a function of temperature calculated using the formula, $\sigma_{xy} = -\frac{\rho_{xy}}{\rho_{xy}^2 + \rho_{xx}^2}$. In Fig. 6.5(b), we have fitted the Hall conductivity curves using the single band model, $\sigma_{xy} = [\frac{n_h \mu_h{}^2}{1+(\mu_h B)^2}]eB$ as at low temperatures the hole carriers dominate the total Hall transport. Here, n_h is hole carrier density and μ_h is hole mobility. From the fits, we derived the hole carrier concentration of n_h is 1.06×10^{20} cm^{-3} and hole mobility of $\mu = 0.049$ m^2/Vs at 2 K. These values are consistent with a previous report on these systems [76].

To uncover the mechanism of unsaturated linear MR, we performed density functional theory calculations as illustrated in Fig. 6.6. For the DFT calculations, we considered the magnetic structure as shown in Fig. 6.6(b), depicted by the neutron diffraction study on this system [241]. Fig. 6.6(c) displays the electronic band dispersion along the high-symmetry k-path of $\Gamma - \mathrm{M} - \mathrm{K} - \Gamma$ calculated without and with considering the spin-orbit coupling (SOC). From the electronic band structure, we notice several linear band crossings (Dirac-like) at the K point in the vicinity of the Fermi level. One Dirac point (DP1) is observed at a binding energy of 90 meV below the Fermi level (E_F) that is gapless without SOC, but under SOC the Dirac point is gapped by lifting the degeneracy. DP2 is found at a binding energy of 40 meV below the E_F which is always gaped. DP3 is found at a biding energy of 250 meV above E_F which is gapless for both with SOC and without SOC. Our calculations on $\mathrm{HoMn_6Ge_6}$ are inline with previous calculations performed on $\mathrm{HoMn_6Sn_6}$ [237, 240]. Particularly, the calculations on $\mathrm{HoMn_6Sn_6}$ demonstrated that gap size at the Dirac points depends explicitly on the magnetic spin orientation with respect to the crystal axis [237,240]. Means, larger (smaller) gaps were predicted for the fields applied along the out-of-plane (in-plane) direction. Since our calculations were performed with an angle of $\theta_S = 60^{\deg}$ between the z-axis and plane of magnetic moments, which is neither out-of-plane nor in-plane, we observe both gapped and gapless Dirac points. This observation hints for the possibility of a critical angle of magnetic moments at which the Dirac states are gapless and robust under SOC.

Apart from the linear band dispersions at the K point we also observe two hole-like band dispersions (h_1 and h_2) crossing the Fermi level around K point and an electron-like (e_1) band dispersion crossing the Fermi level around the Γ point. No bands are found at the M-point crossing the Fermi level. In addition, we found several flat bands (fb_1, fb_2, and fb_3) which are dispersionless throughout the Brillouin zone. Figs. 6.6(d)-(f) show the three-dimensional view of the Fermi surface maps which are mainly contributed by three types of Fermi pockets; one of them is the electron-like (e_1) pocket with an almost cylindrical-shape as shown in Fig. 6.6(d), the second one is the hole-like (h_1) pocket which is close to one-third of a cylinder shared by each corner of the hexagon as shown in Fig. 6.6(e), and the last one is the hip-roof shaped hole-like (h_2) pocket at the K point. With the help of these three types of Fermi pockets, we estimated the hole carrier density n_h=5.3 $\times$ 10^{20}/cm^3 and electron carrier density n_e=3.6 $\times$ 10^{20}/cm^3 to find the net hole carrier density of 1.7 $\times$ 10^{20}/cm^3 using Luttinger's theorem [256]. Interestingly, this value is close to the experimentally calculated hole carrier density (1.06 $\times$ 10^{20} cm^{-3}) from the Hall data at 2 K. Nevertheless, the estimated hole and electron carrier densities are nearly equal, suggesting $\mathrm{HoMn_6Ge_6}$ to be a semimetal. Figs. 6.6(g) and 6.6(h) illustrate the of the Fermi surfaces projected onto the $k_x - k_y$ and $k_x - k_z$ plane, clearly showing the electron-like Fermi pocket at the Γ and hole-like Fermi pockets at the K point.

As for the angle-dependent magnetoresistance (ADMR) measurements, the magnetic field is always perpendicular to the current direction which does not change the Lorentz force acting on the charge carriers. Further, the spin-electron scattering can be neglected at low temperatures as the mean free path of charge carrier is much higher. This brings us to conclude that the anisotropic ADMR has the electronic band structure origin than the magnetism origin. The Fermi velocity can be calculated as $v_k = \frac{1}{\hbar}\nabla_k \epsilon_k$, which depends on the local curvature of the Fermi surface cross-section. The smaller the orbit of the Fermi surface cross-section the greater the local curvature, which in turn leads to a higher Fermi velocity. Hence, high microscopic Lorentz force would act on the charge carriers [257–259]. Our calculations indicate that the electron pocket e_1 and hole pocket h_1 exhibit nearly cylindrical shapes with their diameters and heights being quite similar in value, making them nearly isotropic. Only the h_2 hole pocket has an anisotropic shape (hip-roof shaped) which could be the possible origin of this high anisotropic ADMR. Because when the field is applied along the z-axis, the charge carriers are subjected to orbit on the $k_x - k_y$ plane. Similarly, for the fields applied along the y-axis the carriers would orbit on the $k_x - k_z$ plane. As observed in Fig. 6.6(g), the Fermi sheets at K point are nearly circular for $H \parallel z$ [see Fig. 6.4(a) for $\theta = 0^o$]. Only the out-of-plane Fermi sheets ($k_x - k_z$) have substantial curvature [see Fig. 6.6(h)] which are detected experimentally for $H \parallel y$ [see Fig. 6.4(a) for $\theta = 90^o$]. Therefore, we think that the asymmetric MR is originated from the asymmetric out-of-plane Fermi pockets. Further, as evidenced from our DFT band structure calculations, the linear nonsaturating MR is mainly contributed by the linear Dirac-like bands present near the Fermi level.

6.4 Summary

In summary, we have grown high-quality single crystals of $HoMn_6Ge_6$ using the Sn flux. Electrical resistivity demonstrate an overall metallic nature throughout the measured temperature range with a few magnetic transition-driven anomalies. A crossover from negative to positive magnetoresistance (MR) is observed at a critical temperature of 150 K. While the linear nonsaturating positive MR exits in the low-temperature region mainly driven by the Dirac-like linear band dispersions, the negative MR observed in the higher temperature region is due to the spin-flop type magnetic transition. We found anomalous Hall effect in addition to a dominant charge carrier switching across 220 K. We performed electronic band structure calculations on $HoMn_6Ge_6$ by considering the skew-spiral magnetic structure of the system to realize large anisotropy in the out-of-plane Fermi sheets. We suggest that the large anisotropic out-of-plane magnetoresistance observed in $HoMn_6Ge_6$ is originated from the anisotropic out-of-plane Fermi surfaces. The band structure calculations predict several Dirac-type band crossings at the K point in the vicinity of the Fermi level. The derived nearly equal electron and hole carrier densities with the help of the calculated Fermi surfaces, suggest $HoMn_6Ge_6$ to be a kagome Dirac semimetal.

Chapter 7

Conclusions

We can summarize our work as followings based on the four projects I have completed during my Ph.D.

In the first project, we have focused on Mn_3Sn. We have found topological Hall effect in pure form at room temperature which decays with Fe doping. We see how a small concentration of Fe atoms doping in this system change its magnetic properties specially at low temperature. The out-of-plane anomalous Hall effect is originated from k-space Berry curvature in this system while the in-plane pure topological part can be possibly due to the non-coplanar structure generated due to Mn deficiency in our system.

In the second project, we systematically studied the electrical resistivity, Hall, and magnetization of $Mn_{3x}Fe_xSn$ single crystals. From resistivity, we see the introduction of metal to insulator-type transition with 0.25 Fe doping. With higher $x = 0.35$ doping, we see a low-temperature resistivity upturn at low temperatures along with MI transition at higher temperatures. The magnetization study reveals ferromagnetic-like magnetization arising from Fe doping at lower temperatures where the magnetization changes its easy axis towards the z direction, although there is no such huge change in room temperature magnetization properties. Though Mn_3Sn only has ordinary Hall contribution below spin reorientation temperature for ρ_{zx}, we see AHE at a lower temperature due to Fe doping, which helps to hold the inverse triangular magnetic structure. As for ρ_{xy}, Mn_3Sn does not have AHE at any temperature. In contrast, due to induced ferromagnetism with Fe doping, a large AHR and a significant topological Hall effect are present in the system. Ultimately, the sizeable topological Hall effect shown by this system at low temperatures could be due to the formation of skyrmions. The uniaxial magnetic anisotropy with Fe doping, along with inplane magnetization, can make the possible environment for skyrmions.

Next, we have successfully grown rod shaped single crystal of Fe_3Sn using solid state crystal growth technique. It has a hexagonal crystal structure and the Fe atoms form Kagome network. From our results it is confirmed that Fe_3Sn is a soft type ferromagnet with very high Curie temperature and the easy axis of the magnetization lies on the ab plane of the hexagonal lattice. The longitudinal resistivity shows the presence of Fermi-liquid behaviour at low temperature region and electron-phonon contribution at higher temperature region. Along with intrinsic Hall originated from Berry curvature, we have also observed the presence of extrinsic skew scattering Hall effect. This extrinsic Hall conductivity decays quadratically with temperature due to the electron-phonon interaction.

In the last project, in $HoMn_6Ge_6$, the electrical resistivity demonstrate an overall metallic nature throughout the measured temperature range with a few magnetic transition-driven anomalies. A crossover from negative to positive magnetoresistance (MR) is observed at a critical temperature of 220 K. While the linear nonsaturating positive MR exits in the low-temperature region mainly driven by the Dirac-like linear band dispersion, the negative MR observed in the higher temperature region is due to the spin-flop type magnetic transition. We found anomalous Hall effect in this antiferromagnetic system. We performed electronic band structure calculations on HoMn6Ge6 by considering the skew-spiral magnetic structure of the system to realize large anisotropy in the Fermi surfaces. The band structure calculations predict several Dirac-type band crossings at the K point in the vicinity of the Fermi level.

List of Publications

Publications relevent to the thesis

1. **Achintya Low**, Susanta Ghosh, Soumya Ghorai, and S. Thirupathaiah, ”Effect of Electron-Phonon Scattering on the Anomalous Hall Conductivity of Fe3Sn, a Kagome Ferromagnetic Metal ” Phys. Rev. B **108**, 094404 (2023)

2. **Achintya Low**, Susanta Ghosh, Susmita Changdar, Sayan Routh, Shubham Purwar, and S. Thirupathaiah. ”Tuning of topological properties in the strongly correlated antiferromagnet Mn_3Sn via Fe doping.” Phys. Rev. B **106**, 144429 (2022).

3. **Achintya Low**, Susanta Ghosh, and S. Thirupathaiah, ”Anisotropic Nonsaturating Magnetoresistance Observed in $HoMn_6Ge_6$: A Kagome Dirac Semimetal.” (accepted in Phys. Rev. B, in press)

4. **Achintya Low**, Susanta Ghosh, Sayan Routh,Setti Thirupathaiah, ”Topological Hall Effect Instigated in Kagome Antiferromagnet $Mn_{3-x}Sn$ due to Mn-deficient Induced Noncoplanar Spin Structure” (submitted)

Other works

1. Susmita Changdar, Susanta Ghosh, Anumita Bose, Indrani Kar, **Achintya Low**, Patrick Le Fèvre, François Bertran, Awadhesh Narayan and Setti Thirupathaiah, ”Weak electronic correlations observed in magnetic Weyl Semimetal Mn_3Ge” J. Phys.: Condens. Matter 36 (2024) 125502.

2. Susanta Ghosh, **Achintya Low**, Soumya Ghorai, Kalyan Mandaland Setti Thirupathaiah, ”Tuning of electrical, magnetic, andtopological properties of magnetic Weylsemimetal $Mn_{3+x}Ge$ by Fe doping”, J. Phys.: Condens. Matter 35 (2023): 485701

3. Shubham Purwar, **Achintya Low**, Anumita Bose, Awadhesh Narayan, and Setti Thirupathaiah. “Investigation of the anomalous and topological Hall effects in layered monoclinic ferromagnet $Cr_{2.76}Te_4$” Phys. Rev. Materials 7, 094204 (2023)

4. Shubham Purwar, Anumita Bose, **Achintya Low**, Susanta Ghosh,Sayan Routh, Awadhesh Narayan, and Setti Thirupathaiah. “Discovery of Superconductivity in Van der Waals Ferromagnetic $Sn_{0.06}Cr_3Te_4$” arXiv:2302.05145

Bibliography

[1] Yôichirô Nambu. Nobel Lecture: Spontaneous symmetry breaking in particle physics: A case of cross fertilization. *Reviews of Modern Physics*, 81(3):1015–1018, 7 2009.

[2] Andreas Trenkwalder, G. Spagnolli, Giulia Semeghini, Simon Coop, Manuele Landini, P. C. M. Castilho, Luca Pezzè, Giovanni Carlo Modugno, M. Inguscio, Augusto Smerzi, and Marco Fattori. Quantum phase transitions with parity-symmetry breaking and hysteresis. *Nature Physics*, 12(9):826–829, 5 2016.

[3] K. Von Klitzing, G. Dorda, and M. Pepper. New Method for High-Accuracy Determination of the Fine-Structure Constant based on quantized Hall resistance. *Physical Review Letters*, 45(6):494–497, 8 1980.

[4] D. C. Tsui, H. L. Störmer, and A. C. Gossard. Two-Dimensional magnetotransport in the extreme quantum limit. *Physical Review Letters*, 48(22):1559–1562, 5 1982.

[5] C. L. Kane and Eugene J. Mele. Quantum Spin Hall effect in graphene. *Physical Review Letters*, 95(22), 11 2005.

[6] Liang Fu, C. L. Kane, and Eugene J. Mele. Topological insulators in three dimensions. *Physical Review Letters*, 98(10), 3 2007.

[7] Joel E. Moore and Leon Balents. Topological invariants of time-reversal-invariant band structures. *Physical Review B*, 75(12), 3 2007.

[8] Steve M. Young, Saad Zaheer, Jeffrey C. Y. Teo, C. L. Kane, Eugene J. Mele, and Andrew M. Rappe. Dirac Semimetal in three dimensions. *Physical Review Letters*, 108(14), 4 2012.

[9] Madhab Neupane, Su Xu, Raman Sankar, Nasser Alidoust, Guang Bian, Chang Liu, Ilya Belopolski, Tay Rong Chang, Horng Tay Jeng, Hsin Lin, Arun Bansil, F. C. Chou, and M. Zahid Hasan. Observation of a three-dimensional topological Dirac semimetal phase in high-mobility Cd3As2. *Nature Communications*, 5(1), 5 2014.

[10] Ling Lü, Zhiyu Wang, Dexin Ye, Lixin Ran, Liang Fu, John D. Joannopoulos, and Marin Soljačić. Experimental observation of Weyl points. *Science*, 349(6248):622–624, 8 2015.

[11] Su-Yang Xu, Ilya Belopolski, Nasser Alidoust, Madhab Neupane, Chenglong Zhang, Raman Sankar, Shin-Ming Huang, Chi-Cheng Lee, Guoqing Chang, Baokai Wang, Guang Bian, Hao Zheng, Daniel S. Sanchez, F. C. Chou, Hsin Lin, Shuang Jia, and M. Zahid Hasan. Discovery of a Weyl fermion semimetal and topological Fermi arcs. *Science*, 349(6248):613–617, 8 2015.

[12] M. Zahid Hasan and C. L. Kane. Colloquium: Topological insulators. *Reviews of Modern Physics*, 82(4):3045–3067, 11 2010.

[13] Arun Bansil, Hsin Lin, and Tanmoy Das. Colloquium: Topological band theory. *Reviews of Modern Physics*, 88(2), 6 2016.

[14] Chetan Nayak, Steven H. Simon, Ady Stern, Michael Freedman, and Sankar Das Sarma. Non-Abelian anyons and topological quantum computation. *Rev. Mod. Phys.*, 80:1083–1159, Sep 2008.

[15] Jiaxin Yin, Biao Lian, and M. Zahid Hasan. Topological kagome magnets and superconductors. *Nature*, 612(7941):647–657, 12 2022.

[16] Michail Ilych Monastyrsky. *Topology in condensed matter*. 1 2006.

[17] Michael Berry. Quantal phase factors accompanying adiabatic changes. *Proceedings of the Royal Society of London*, 392(1802):45–57, 3 1984.

[18] Barry Bradlyn and Mikel Iraola. Lecture notes on Berry phases and topology. *SciPost physics lecture notes*, 5 2022.

[19] Mobarak Hossain Polash, Shahram Yalameha, Haihan Zhou, Kaveh Ahadi, Zahra Nourbakhsh, and Daryoosh Vashaee. Topological quantum matter to topological phase conversion: Fundamentals, materials, physical systems for phase conversions, and device applications. *Materials Science and Engineering: R: Reports*, 145:100620, 7 2021.

[20] Efthimios Kaxiras and John D. Joannopoulos. *Quantum Theory of Materials*. 4 2019.

[21] Michael El-Batanouny. *Advanced Quantum Condensed Matter Physics*. Cambridge University Press, 3 2020.

[22] Shun-Qing Shen. *Topological insulators*. 1 2012.

[23] Roland Winkler. *Spin—Orbit coupling effects in Two-Dimensional electron and hole systems*. 1 2003.

[24] Feng Wang, Di Xiao, Jun Ding, and Yugui Yao. Three-Dimensional topological insulators inI−III−VI2andII−IV. *Physical Review Letters*, 106(1), 1 2011.

[25] Kaustuv Manna, Yan Sun, Lukas Muechler, J. Kübler, and Claudia Felser. Heusler, Weyl and Berry. *Nature Reviews Materials*, 3(8):244–256, 7 2018.

[26] Edwin H Hall. On a new action of the magnet on electric currents. *American Journal of Mathematics*, 2(3):287–292, 1879.

[27] *The Quantum Hall effect*. 1 1987.

[28] B. Andrei Bernevig, Taylor L. Hughes, and Shou Cheng Zhang. Quantum Spin Hall Effect and Topological phase transition in HGTE Quantum Wells. *Science*, 314(5806):1757–1761, 12 2006.

[29] Markus König, Steffen Wiedmann, C. Brüne, Albrecht Roth, H. Buhmann, L. W. Molenkamp, Xiang Qi, and Shou Cheng Zhang. Quantum Spin Hall Insulator State in HGTE Quantum Wells. *Science*, 318(5851):766–770, 11 2007.

[30] E.H. Hall. On the new action of magnetism on a permanent electric current. *The London, Edinburgh, and Dublin Philosophical Magazine and Journal of Science*, 10(63):301–328, 1880.

[31] Alpheus W. Smith. The Variation of the Hall Effect in Metals with Change of Temperature. *Physical Review*, 30(1):1–34, 1 1910.

[32] Satoru Nakatsuji, Naoki Kiyohara, and Tomoya Higo. Large anomalous Hall effect in a non-collinear antiferromagnet at room temperature. *Nature*, 527(7577):212–215, 10 2015.

[33] Ajaya K Nayak, Julia Erika Fischer, Yan Sun, Binghai Yan, Julie Karel, Alexander C Komarek, Chandra Shekhar, Nitesh Kumar, Walter Schnelle, Jürgen Kübler, et al. Large anomalous Hall effect driven by a nonvanishing Berry curvature in the noncolinear antiferromagnet Mn_3Ge. *Sci. Adv.*, 2(4):e1501870, 2016.

[34] Naoto Nagaosa, Jairo Sinova, Shigeki Onoda, A. H. MacDonald, and N. P. Ong. Anomalous Hall effect. *Rev. Mod. Phys.*, 82:1539–1592, May 2010.

[35] Robert Karplus and J. M. Luttinger. Hall Effect in Ferromagnetics. *Phys. Rev.*, 95:1154–1160, Sep 1954.

[36] J. Smit. The spontaneous hall effect in ferromagnetics I. *Physica*, 21(6-10):877–887, 1 1955.

[37] J. Smit. The spontaneous hall effect in ferromagnetics II. *Physica*, 24(1):39–51, 1958.

[38] L. Berger. Side-Jump Mechanism for the Hall Effect of Ferromagnets. *Phys. Rev. B*, 2:4559–4566, Dec 1970.

[39] A. Neubauer, C. Pfleiderer, B. Binz, A. Rosch, R. Ritz, P. G. Niklowitz, and P. Böni. Topological Hall Effect in the A Phase of MnSi. *Phys. Rev. Lett.*, 102:186602, May 2009.

[40] Muhlbauer, S. and Binz, B. and Jonietz, F. and Pfleiderer, C. and Rosch, A. and Neubauer, A. and Georgii, R. and Boni, P. Skyrmion Lattice in a Chiral Magnet. *Science*, 323(5916):915–919, 2009.

[41] J. Yan, X. Luo, H. Y. Lv, Y. Sun, P. Tong, W. J. Lu, X. B. Zhu, W. H. Song, and Y. P. Sun. Room-temperature angular-dependent topological Hall effect in chiral antiferromagnetic Weyl semimetal Mn_3Sn. *Appl. Phys. Lett.*, 115(10):102404, 2019.

[42] Subhajit Roychowdhury, Sukriti Singh, Satya N. Guin, Nitesh Kumar, Tirthankar Chakraborty, Walter Schnelle, Horst Borrmann, Chandra Shekhar, and Claudia Felser. Giant Topological Hall Effect in the Noncollinear Phase of Two-Dimensional Antiferromagnetic Topological Insulator MnBi4Te7. *Chemistry of Materials*, 33(21):8343–8350, 2021.

[43] Bin Pang, Lunyong Zhang, YB Chen, Jian Zhou, Shuhua Yao, Shantao Zhang, and Yanfeng Chen. Spin-glass-like behavior and topological Hall effect in $SrRuO_3$/$SrIrO_3$ superlattices for oxide spintronics applications. *ACS Appl. Mater. Interfaces*, 9(3):3201–3207, 2017.

[44] Albert Fert, Nicolas Reyren, and Vincent Cros. Magnetic skyrmions: advances in physics and potential applications. *Nature Reviews Materials*, 2(7):1–15, 2017.

[45] U. K. Rößler, A. N. Bogdanov, and C. Pfleiderer. Spontaneous skyrmion ground states in magnetic metals. *Nature*, 442(7104):797–801, 2006.

[46] XZ Yu, Y Tokunaga, Y Kaneko, WZ Zhang, K Kimoto, Y Matsui, Y Taguchi, and Y Tokura. Biskyrmion states and their current-driven motion in a layered manganite. *Nature Communications*, 5(1):1–7, 2014.

[47] Zhipeng Hou, Weijun Ren, Bei Ding, Guizhou Xu, Yue Wang, Bing Yang, Qiang Zhang, Ying Zhang, Enke Liu, Feng Xu, Wenhong Wang, Guangheng Wu, Xixiang Zhang, Baogen Shen, and Zhidong Zhang. Observation of Various and Spontaneous

Magnetic Skyrmionic Bubbles at Room Temperature in a Frustrated Kagome Magnet with Uniaxial Magnetic Anisotropy. *Adv. Mater.*, 30(7):1706306, 2018.

[48] Takashi Kurumaji, Taro Nakajima, Max Hirschberger, Akiko Kikkawa, Yuichi Yamasaki, Hajime Sagayama, Hironori Nakao, Yasujiro Taguchi, Taka-hisa Arima, and Yoshinori Tokura. Skyrmion lattice with a giant topological Hall effect in a frustrated triangular-lattice magnet. *Science*, 365(6456):914–918, 2019.

[49] Shijiang Luo and Long You. Skyrmion devices for memory and logic applications. *APL Materials*, 9(5):050901, 2021.

[50] I. Dzyaloshinsky. A thermodynamic theory of “weak” ferromagnetism of antiferromagnetics. *Journal of Physics and Chemistry of Solids*, 4(4):241–255, 1958.

[51] Y. Shiomi, S. Iguchi, and Y. Tokura. Emergence of topological Hall effect from fanlike spin structure as modified by Dzyaloshinsky-Moriya interaction in MnP. *Phys. Rev. B*, 86:180404, Nov 2012.

[52] Max Hirschberger, Taro Nakajima, Shang Gao, Licong Peng, Akiko Kikkawa, Takashi Kurumaji, Markus Kriener, Yuichi Yamasaki, Hajime Sagayama, Hironori Nakao, et al. Skyrmion phase and competing magnetic orders on a breathing kagomé lattice. *Nature communications*, 10(1):1–9, 12 2019.

[53] Zhipeng Hou, Weijun Ren, Bei Ding, Guizhou Xu, Yue Wang, Bing Yang, Qiang Zhang, Ying Zhang, Enke Liu, Feng Xu, Wenhong Wang, Guangheng Wu, Xixiang Zhang, Baogen Shen, and Zhidong Zhang. Observation of Various and Spontaneous Magnetic Skyrmionic Bubbles at Room Temperature in a Frustrated Kagome Magnet with Uniaxial Magnetic Anisotropy. *Advanced Materials*, 29(29):1701144, 6 2017.

[54] N. Kanazawa, Y. Onose, T. Arima, D. Okuyama, K. Ohoyama, S. Wakimoto, K. Kakurai, S. Ishiwata, and Y. Tokura. Large Topological Hall Effect in a Short-Period Helimagnet MnGe. *Phys. Rev. Lett.*, 106:156603, Apr 2011.

[55] Katharina Zeissler, Simone Finizio, Kowsar Shahbazi, Jamie Massey, Fatma Al Ma’Mari, David M Bracher, Armin Kleibert, Mark C Rosamond, Edmund H Linfield, Thomas A Moore, et al. Discrete Hall resistivity contribution from Néel skyrmions in multilayer nanodiscs. *Nature Nanotechnology*, 13(12):1161–1166, 2018.

[56] K. S. Denisov, I. V. Rozhansky, N. S. Averkiev, and E. Lähderanta. General theory of the topological Hall effect in systems with chiral spin textures. *Phys. Rev. B*, 98:195439, Nov 2018.

[57] Hongwen Song, Sheng-Jie Huang, Liang Fu, and Michael Hermele. Topological phases protected by point group symmetry. *Physical Review X*, 7(1), 2 2017.

[58] P. A. M. Dirac. The quantum theory of the electron. *Proceedings of the Royal Society of London*, 117(778):610–624, 2 1928.

[59] Paul Adrien Maurice Dirac. *The principles of quantum mechanics*. Oxford University Press, 1 1981.

[60] Hermann Weyl. Elektron und Gravitation. I. *The European Physical Journal A*, 56(5-6):330–352, 5 1929.

[61] Palash B. Pal. Dirac, Majorana, and Weyl fermions. *American Journal of Physics*, 79(5):485–498, 4 2011.

[62] Shengyuan A. Yang. Dirac and Weyl Materials: Fundamental aspects and some Spintronics applications. *Spin*, 06(02):1640003, 6 2016.

[63] Philip R. Wallace. The Band Theory of Graphite. *Physical Review*, 71(9):622–634, 5 1947.

[64] N. P. Armitage, E. J. Mele, and Ashvin Vishwanath. Weyl and Dirac semimetals in three-dimensional solids. *Reviews of Modern Physics*, 90(1), 1 2018.

[65] Kostya S Novoselov, Andre K Geim, Sergei Vladimirovich Morozov, Dingde Jiang, Michail I Katsnelson, Irina V Grigorieva, SVb Dubonos, and andAA Firsov. Two-dimensional gas of massless Dirac fermions in graphene. *Nature*, 438(7065):197–200, 2005.

[66] Lucile Savary and Leon Balents. Quantum spin liquids: a review. *Rep. Prog. Phys.*, 80(1):016502, nov 2016.

[67] Yi Zhou, Kazushi Kanoda, and Tai-Kai Ng. Quantum spin liquid states. *Reviews of Modern Physics*, 89(2):025003, 2017.

[68] C. Broholm, R. J. Cava, S. A. Kivelson, D. G. Nocera, M. R. Norman, and T. Senthil. Quantum spin liquids. *Science*, 367(6475):eaay0668, 2020.

[69] Masayoshi Fujihala, Katsuhiro Morita, Richard A. Mole, Setsuo Mitsuda, Takami Tohyama, Shin Ichiro Yano, Dehong Yu, Shigetoshi Sota, Tomohiko Kuwai, A. Koda, Hirotaka Okabe, Hua Lee, Shinichi Itoh, Takafumi Hawai, Takatsugu Masuda, Hajime Sagayama, Akira Matsuo, Koichi Kindo, Seiko Ohira-Kawamura, and Kenji Nakajima. Gapless spin liquid in a square-kagome lattice antiferromagnet. *Nature Communications*, 11(1), 7 2020.

[70] Zhenyuan Zeng, Xiaoyan Ma, Si Wu, Haifeng Li, Zhen Tao, Xingye Lu, Xiaohui Chen, Jin-Xiao Mi, Shijie Song, Guang-Han Cao, Guangwei Che, Kuo Li, Gang Li, Huiqian Luo, Zi Yang Meng, and Shiliang Li. Possible Dirac quantum spin liquid in the kagome quantum antiferromagnet YCu3(OH)6Br2[Brx(. *Physical review*, 105(12), 3 2022.

[71] Yaojia Wang, Heng Wu, Gregory T. McCandless, Julia Y. Chan, and Mazhar N. Ali. Quantum states and intertwining phases in kagome materials. *Nature Reviews Physics*, 5(11):635–658, 9 2023.

[72] Jia-Xin Yin, Wenlong Ma, Tyler A. Cochran, Xitong Xu, Songtian S. Zhang, Hung-Ju Tien, Nana Shumiya, Guangming Cheng, Kun Jiang, Biao Lian, Zhida Song, Guoqing Chang, Ilya Belopolski, Daniel Multer, Maksim Litskevich, Zi Jia Cheng, Xian Yang, Bianca Swidler, Huibin Zhou, Hsin Lin, Titus Neupert, Ziqiang Wang, Nan Yao, Tay Rong Chang, Shuang Jia, and M. Zahid Hasan. Quantum-limit Chern topological magnetism in $\mathrm{TbMn_6Sn_6}$. *Nature*, 583(7817):533–536, 7 2020.

[73] Enke Liu, Yan Sun, Nitesh Kumar, Lukas Muechler, Aili Sun, Lin Jiao, Shuo-Ying Yang, Defa Liu, Aiji Liang, Qiunan Xu, et al. Giant anomalous Hall effect in a ferromagnetic kagome-lattice semimetal. *Nature physics*, 14(11):1125–1131, 7 2018.

[74] Mingu Kang, Linda Ye, Shiang Fang, Jhih-Shih You, Abe Levitan, Minyong Han, Jorge I. Facio, Chris Jozwiak, Aaron Bostwick, Eli Rotenberg, Mun Chan, Ross McDonald, David Graf, Konstantine Kaznatcheev, E. Vescovo, David C. Bell, Efthimios Kaxiras, Jeroen Van Den Brink, Manuel Richter, Madhav Prasad Ghimire, Joseph Checkelsky, and Riccardo Comin. Dirac fermions and flat bands in the ideal kagome metal FeSn. *Nature Materials*, 19(2):163–169, 12 2019.

[75] Linpeng Nie, Kuanglv Sun, Wanru Ma, D. W. Song, Lilin Zheng, Zuowei Liang, Ping Wu, Fangwei Yu, Jian Li, Mengtian Shan, Dan Zhao, Shunjiao Li, Bei-Sheng Kang, Zhimian Wu, Yu Zhou, Kai Li, Ziji Xiang, Jianjun Ying, Z. F. Wang, Tao Wu, and Xian Hui Chen. Charge-density-wave-driven electronic nematicity in a kagome superconductor. *Nature*, 604(7904):59–64, 2 2022.

[76] Wenlong Ma, Xitong Xu, Jia-Xin Yin, Hui Yang, Huibin Zhou, Zi-Jia Cheng, Yuqing Huang, Zhe Qu, Fa Wang, M. Zahid Hasan, and Shuang Jia. Rare Earth Engineering in $R\mathrm{Mn_6Sn_6}$ ($R = \mathrm{Gd}-\mathrm{Tm}$, Lu) Topological Kagome Magnets. *Phys. Rev. Lett.*, 126:246602, Jun 2021.

[77] Noam Morali, Rajib Batabyal, Pranab Kumar Nag, Enke Liu, Qiunan Xu, Yan Sun, Binghai Yan, Claudia Felser, Nurit Avraham, and Haim Beidenkopf. Fermi-Arc di-

versity on surface terminations of the magnetic Weyl semimetal $Co_3Sn_2S_2$. *Science*, 365(6459):1286–1291, 2019.

[78] Hao Yang, Yan Sun, Yang Zhang, Wu-Jun Shi, Stuart S P Parkin, and Binghai Yan. Topological Weyl semimetals in the chiral antiferromagnetic materials Mn_3Ge and Mn_3Sn. *New Journal of Physics*, 19(1):015008, jan 2017.

[79] K. Kuroda, T. Tomita, M.-T. Suzuki, C. Bareille, A. A. Nugroho, P. Goswami, M. Ochi, M. Ikhlas, M. Nakayama, S. Akebi, R. Noguchi, R. Ishii, N. Inami, K. Ono, H. Kumigashira, A. Varykhalov, T. Muro, T. Koretsune, R. Arita, S. Shin, Takeshi Kondo, and S. Nakatsuji. Evidence for magnetic Weyl fermions in a correlated metal. *Nat. Mater.*, 16(11):1090–1095, 9 2017.

[80] Taishi Chen, Takahiro Tomita, Susumu Minami, Mingxuan Fu, Takashi Koretsune, Motoharu Kitatani, Ikhlas Muhammad, Daisuke Nishio-Hamane, Rieko Ishii, Fumiyuki Ishii, Ryotaro Arita, and Satoru Nakatsuji. Anomalous transport due to Weyl fermions in the chiral antiferromagnets Mn_3X (X=Sn, Ge). *Nat. Commun.*, 12:572, 2021.

[81] Mingu Kang, Shiang Fang, Linda Ye, Hoi Chun Po, Jonathan D. Denlinger, Chris Jozwiak, Aaron Bostwick, Eli Rotenberg, Efthimios Kaxiras, Joseph Checkelsky, and Riccardo Comin. Topological flat bands in frustrated kagome lattice CoSn. *Nature Communications*, 11(1), 8 2020.

[82] Minyong Han, Hisashi Inoue, Shiang Fang, Caolan John, Linda Ye, Mun K Chan, David Graf, Takehito Suzuki, Madhav Prasad Ghimire, and Won Joon Cho. Evidence of two-dimensional flat band at the surface of antiferromagnetic kagome metal FeSn. *Nat. Commun.*, 12(1):5345, 2021.

[83] Kun Jiang, Tao Wu, Jiaxin Yin, Zhenyu Wang, M. Zahid Hasan, Stephen D. Wilson, Xianhui Chen, and Jiangping Hu. Kagome superconductors AV3Sb5 (A = K, Rb, Cs). *National Science Review*, 10(2), 9 2022.

[84] Zuowei Liang, Xiaochen Hou, Fan Zhang, Wanru Ma, Ping Wu, Zongyuan Zhang, Fangwei Yu, Jianjun Ying, Kun Jiang, Lei Shan, Zhenyu Wang, and X.-h. Chen. Three-Dimensional charge density wave and Surface-Dependent Vortex-Core states in a Kagome superconductor CSV3SB5. *Physical Review X*, 11(3), 8 2021.

[85] H.L. Bhat. *Introduction to crystal growth.* CRC Press, 10 2014.

[86] Hubertus Giefers and Malcolm Nicol. High pressure X-ray diffraction study of all Fe–Sn intermetallic compounds and one Fe–Sn solid solution. *Journal of Alloys and Compounds*, 422(1-2):132–144, 9 2006.

[87] H. M. Rietveld. A profile refinement method for nuclear and magnetic structures. *Journal of Applied Crystallography*, 2(2):65–71, 6 1969.

[88] J. C. Garland and R. Bowers. Evidence for Electron-Electron scattering in the Low-Temperature resistivity of simple metals. *Physical Review Letters*, 21(14):1007–1009, 9 1968.

[89] Bar Levy, Moshe Sinvani, and A. J. Greenfield. Sample Dependence of the Electron-Electron contribution to the electrical resistivity of sodium and potassium. *Physical Review Letters*, 43(24):1822–1825, 12 1979.

[90] Djurdje Cvijović. The Bloch-Gruneisen function of arbitrary order and its series representations. *Theoretical and Mathematical Physics*, 166(1):37–42, 1 2011.

[91] F. Bloch. Zum elektrischen Widerstandsgesetz bei tiefen Temperaturen. *The European Physical Journal A*, 59(3-4):208–214, 3 1930.

[92] Tineke Van Peski-Tinbergen and A. J. Dekker. Spin-dependent scattering and resistivity of magnetic metals and alloys. *Physica*, 29(9):917–937, 9 1963.

[93] Carl A. Kukkonen and Pierre F. Maldague. Electron-Hole scattering and the electrical resistivity of the SemimetalTIS2. *Physical Review Letters*, 37(12):782–785, 9 1976.

[94] Dipak Patel, Su Hun Kim, Wenbin Qiu, Masafumi Maeda, Akiyoshi Matsumoto, Gen Nishijima, Hiroaki Kumakura, Seyong Choi, and Jung Ho Kim. Niobium-titanium (Nb-Ti) superconducting joints for persistent-mode operation. *Scientific Reports*, 9(1), 10 2019.

[95] E. H. Hall. On a New Action of the Magnet on Electric Currents. In *Semiconductor Devices: Pioneering Papers*, pages 153–158. WORLD SCIENTIFIC, mar 1991.

[96] R. S. Popović. In *Hall Effect Devices*. CRC Press, 2004.

[97] E. Ramsden. In *Hall-Effect Sensors: Theory and Application*. Elsevier, dec 2006.

[98] M. I. Dyakonov and I. V. Perel. Possibility of orientating electron spins with current. *Sov. Phys. JETP Lett.*, 13:467, 1971.

[99] R. B. Laughlin. Quantized Hall conductivity in two dimensions. *Phys. Rev. B*, 23:5632–5633, May 1981.

[100] F. D. M. Haldane. Model for a Quantum Hall Effect without Landau Levels: Condensed-Matter Realization of the ”Parity Anomaly”. *Phys. Rev. Lett.*, 61(18):2015–2018, Oct 1988.

[101] Libor Šmejkal, Rafael González-Hernández, T. Jungwirth, and J. Sinova. Crystal time-reversal symmetry breaking and spontaneous Hall effect in collinear antiferromagnets. *Sci. Adv.*, 6:aaz8809, 2020.

[102] P. Bruno, V. K. Dugaev, and M. Taillefumier. Topological Hall Effect and Berry Phase in Magnetic Nanostructures. *Phys. Rev. Lett.*, 93:096806, Aug 2004.

[103] Minhyea Lee, W. Kang, Y. Onose, Y. Tokura, and N. P. Ong. Unusual Hall Effect Anomaly in MnSi under Pressure. *Phys. Rev. Lett.*, 102:186601, May 2009.

[104] Tôru Moriya. Anisotropic Superexchange Interaction and Weak Ferromagnetism. *Phys. Rev.*, 120:91–98, Oct 1960.

[105] G. Shirane, R. Cowley, C. Majkrzak, J. B. Sokoloff, B. Pagonis, C. H. Perry, and Y. Ishikawa. Spiral magnetic correlation in cubic mnsi. *Phys. Rev. B*, 28:6251–6255, Dec 1983.

[106] Shōichi Tomiyoshi and Yasuo Yamaguchi. Magnetic Structure and Weak Ferromagnetism of Mn3Sn Studied by Polarized Neutron Diffraction. *J. Phys. Soc. Japan*, 51(8):2478–2486, 1982.

[107] J Sticht, K-H Höck, and J Kübler. Non-collinear itinerant magnetism: the case of Mn_3Sn. *Journal of Physics: Condensed Matter*, 1(43):8155–8176, 1989.

[108] Pyeongjae Park, Joosung Oh, Klára Uhlířová, Jerome Jackson, András Deák, László Szunyogh, Ki Hoon Lee, Hwanbeom Cho, Ha-Leem Kim, Helen C Walker, et al. Magnetic excitations in non-collinear antiferromagnetic Weyl semimetal Mn_3Sn. *npj Quantum Materials*, 3:63, 2018.

[109] Y. Okamura, S. Minami, Y. Kato, Y. Fujishiro, Y. Kaneko, J. Ikeda, J. Muramoto, R. Kaneko, K. Ueda, V. Kocsis, N. Kanazawa, Y. Taguchi, T. Koretsune, K. Fujiwara, A. Tsukazaki, R. Arita, Y. Tokura, and Y. Takahashi. Giant magneto-optical responses in magnetic Weyl semimetal $Co_3Sn_2S_2$. *Nat. Commun.*, 11(1):4619, 2020.

[110] Santu Baidya, Aabhaas Vineet Mallik, Subhro Bhattacharjee, and Tanusri Saha-Dasgupta. Interplay of Magnetism and Topological Superconductivity in Bilayer Kagome Metals. *Phys. Rev. Lett.*, 125:026401, Jul 2020.

[111] L. D. Sanjeewa, J. Xing, K. M. Taddei, D. Parker, R. Custelcean, C. dela Cruz, and A. S. Sefat. Evidence of Ba-substitution induced spin-canting in the magnetic Weyl semimetal $EuCd_2As_2$. *Phys. Rev. B*, 102:104404, Sep 2020.

[112] X. Z. Yu, N. Kanazawa, Y. Onose, K. Kimoto, W. Z. Zhang, S. Ishiwata, Y. Matsui, and Y. Tokura. Near room-temperature formation of a skyrmion crystal in thin-films of the helimagnet FeGe. *Nature Materials*, 10(2):106–109, 2010.

[113] Toshiaki Tanigaki, Kiyou Shibata, Naoya Kanazawa, Xiuzhen Yu, Yoshinori Onose, Hyun Soon Park, Daisuke Shindo, and Yoshinori Tokura. Real-Space Observation of Short-Period Cubic Lattice of Skyrmions in MnGe. *Nano Letters*, 15(8):5438–5442, 2015.

[114] Oleg Janson, Ioannis Rousochatzakis, Alexander A. Tsirlin, Marilena Belesi, Andrei A. Leonov, Ulrich K. Rößler, Jeroen van den Brink, and Helge Rosner. The quantum nature of skyrmions and half-skyrmions in Cu2OSeO3. *Nature Communications*, 5(1), 2014.

[115] K. G. Rana and O. Meshcheriakova and J. Kübler and B. Ernst and J. Karel and R. Hillebrand and E. Pippel and P Werner and A K Nayak and C Felser and S S P Parkin. Observation of topological Hall effect in Mn_2RhSn films. *New Journal of Physics*, 18(8):085007, aug 2016.

[116] Qiming Shao, Yawen Liu, Guoqiang Yu, Se Kwon Kim, Xiaoyu Che, Chi Tang, Qing Lin He, Yaroslav Tserkovnyak, Jing Shi, and Kang L. Wang. Topological Hall effect at above room temperature in heterostructures composed of a magnetic insulator and a heavy metal. *Nature Electronics*, 2(5):182–186, 2019.

[117] Matthew J. Gilbert. Topological electronics. *Communications Physics*, 4(1), 2021.

[118] N. H. Sung, Filip Ronning, Joe David Thompson, and E. D. Bauer. Magnetic phase dependence of the anomalous Hall effect in Mn_3Sn single crystals. *Appl. Phys. Lett.*, 112(13):132406, 2018.

[119] T. F. Duan, W. J. Ren, W. L. Liu, S. J. Li, W. Liu, and Z. D. Zhang. Magnetic anisotropy of single-crystalline Mn_3Sn in triangular and helix-phase states. *Appl. Phys. Lett.*, 107(8):082403, 2015.

[120] Liangcai Xu, Xiaokang Li, Xiufang Lu, Clément Collignon, Huixia Fu, Jahyun Koo, Benoît Fauqué, Binghai Yan, Zengwei Zhu, and Kamran Behnia. Finite-temperature violation of the anomalous transverse Wiedemann-Franz law. *Sci. Adv.*, 6(17):eaaz3522, 2020.

[121] C. Barone, F. Romeo, A. Galdi, P. Orgiani, L. Maritato, A. Guarino, A. Nigro, and S. Pagano. Universal origin of unconventional $1/f$ noise in the weak-localization regime. *Phys. Rev. B*, 87:245113, Jun 2013.

[122] S. Tomiyoshi, H. Yoshida, H. Ohmori, T. Kaneko, and H. Yamamoto. Electrical properties of the intermetallic compound Mn_3Sn. *J. Magn. Magn. Mater.*, 70(1-3):247–248, 1987.

[123] H Ohmori, S Tomiyoshi, H Yamauchi, and H Yamamoto. Spin structure and weak ferromagnetism of Mn_3Sn. *J. Magn. Magn. Mater.*, 70:249, 1987.

[124] P. J. Brown, V. Nunez, F. Tasset, J. B. Forsyth, and P. Radhakrishna. Determination of the magnetic structure of Mn_3Sn using generalized neutron polarization analysis. *J. Phys. Condens. Matter*, 2(47):9409, 1990.

[125] E. Kren, J. Paitz, G. Zimmer, and E. Zsoldos. Study of the magnetic phase transformation in the Mn_3Sn phase. *Physica B+C*, 80(1-4):226–230, 1975.

[126] John A Mydosh. *Spin glasses: an experimental introduction*. CRC Press, 1993.

[127] R. V. Chamberlin, George Mozurkewich, and R. Orbach. Time Decay of the Remanent Magnetization in Spin-Glasses. *Phys. Rev. Lett.*, 52(10):867–870, 1984.

[128] P. D. Mitchler, R. M. Roshko, and W. Ruan. Non-equilibrium relaxation dynamics in the spin glass and ferromagnetic phases of CrFe. *Philos. Mag. B*, 68(4):539, 1993.

[129] G. Sinha, R. Chatterjee, M. Uehara, and A. K. Majumdar. Relaxation of thermoremanent magnetization in different magnetic phases of Fe-rich γ-FeNiCr alloys. *J. Magn. Magn. Mater.*, 164(3):345–356, 1996.

[130] Marc Gabay and Gérard Toulouse. Coexistence of spin-glass and ferromagnetic orderings. *Phys. Rev. Lett.*, 47(3):201, 1981.

[131] Pradeep K. Rout, P. V. Prakash Madduri, Subhendu K. Manna, and Ajaya K. Nayak. Field-induced topological Hall effect in the noncoplanar triangular antiferromagnetic geometry of Mn_3Sn. *Phys. Rev. B*, 99:094430, Mar 2019.

[132] Achintya Low, Susanta Ghosh, Susmita Changdar, Sayan Routh, Shubham Purwar, and S. Thirupathaiah. Tuning of topological properties in the strongly correlated antiferromagnet Mn_3Sn via Fe doping. *Phys. Rev. B*, 106:144429, Oct 2022.

[133] Yueqing Li, Bei Ding, Xiaotian Wang, Hongwei Zhang, Wenhong Wang, and Zhongyuan Liu. Large topological hall effect observed in tetragonal Mn2PtSn Heusler thin film. *Appl. Phys. Lett.*, 113(6):062406, 2018.

[134] Hang Li, Bei Ding, Jie Chen, Zefang Li, Zhipeng Hou, Enke Liu, Hongwei Zhang, Xuekui Xi, Guangheng Wu, and Wenhong Wang. Large topological Hall effect in a geometrically frustrated kagome magnet Fe_3Sn_2. *Appl. Phys. Lett.*, 114(19):192408, 2019.

[135] Gaoshang Gong, Longmeng Xu, Yuming Bai, Yongqiang Wang, Songliu Yuan, Yong Liu, and Zhaoming Tian. Large topological Hall effect near room temperature in noncollinear ferromagnet $LaMn_2Ge_2$ single crystal. *Phys. Rev. Materials*, 5:034405, Mar 2021.

[136] Qi Wang, Qiangwei Yin, and Hechang Lei. Giant topological Hall effect of ferromagnetic kagome metal Fe_3Sn_2. *Chin. Phys. B*, 29(1):017101, 2020.

[137] Meng Huang, Lei Gao, Ying Zhang, Xunyong Lei, Guojing Hu, Junxiang Xiang, Hualing Zeng, Xuewen Fu, Zengming Zhang, Guozhi Chai, Yong Peng, Yalin Lu, Haifeng Du, Gong Chen, Jiadong Zang, and Bin Xiang. Possible Topological Hall Effect above Room Temperature in Layered Cr1.2Te2 Ferromagnet. *Nano Letters*, 21(10):4280, 2021.

[138] Wenyong Zhang, Balamurugan Balasubramanian, Ahsan Ullah, Rabindra Pahari, Xingzhong Li, Lanping Yue, Shah R. Valloppilly, Andrei Sokolov, Ralph Skomski, and David J. Sellmyer. Comparative study of topological Hall effect and skyrmions in NiMnIn and NiMnGa. *Applied Physics Letters*, 115(17):172404, 2019.

[139] Zhi Li, Jincheng Zhuang, Li Wang, Haifeng Feng, Qian Gao, Xun Xu, Weichang Hao, Xiaolin Wang, Chao Zhang, Kehui Wu, et al. Realization of flat band with possible nontrivial topology in electronic kagome lattice. *Science advances*, 4(11):eaau4511, 2018.

[140] Nirmal J. Ghimire, Rebecca L. Dally, L. Poudel, D. C. Jones, D. Michel, N. Thapa Magar, M. Bleuel, Michael A. McGuire, J. S. Jiang, J. F. Mitchell, Jeffrey W. Lynn, and I. I. Mazin. Competing magnetic phases and fluctuation-driven scalar spin chirality in the kagome metal YMn_6Sn_6. *Sci. Adv.*, 6(51):eabe2680, 2020.

[141] N. Kanazawa, M. Kubota, A. Tsukazaki, Y. Kozuka, K. S. Takahashi, M. Kawasaki, M. Ichikawa, F. Kagawa, and Y. Tokura. Discretized topological Hall effect emerging from skyrmions in constricted geometry. *Phys. Rev. B*, 91:041122, Jan 2015.

[142] Jianpeng Liu and Leon Balents. Anomalous Hall Effect and Topological Defects in Antiferromagnetic Weyl Semimetals: $\mathrm{Mn_3Sn/Ge}$. *Phys. Rev. Lett.*, 119:087202, Aug 2017.

[143] Xiuzhen Yu, Maxim Mostovoy, Yusuke Tokunaga, Weizhu Zhang, Koji Kimoto, Yoshio Matsui, Yoshio Kaneko, Naoto Nagaosa, and Yoshinori Tokura. Magnetic stripes and skyrmions with helicity reversals. *Proc. Natl. Acad. Sci.*, 109(23):8856–8860, 2012.

[144] M. Preißinger, K. Karube, D. Ehlers, B. Szigeti, H.-A. Krug von Nidda, J. S. White, V. Ukleev, H. M. Rønnow, Y. Tokunaga, A. Kikkawa, Y. Tokura, Y. Taguchi, and I. Kézsmárki. Vital role of magnetocrystalline anisotropy in cubic chiral skyrmion hosts. *npj Quantum Materials*, 6(1), 2021.

[145] Sven Bjarke Gudnason and Muneto Nitta. Domain Wall Skyrmions. *Phys. Rev. D*, 89:085022, Apr 2014.

[146] Ran Cheng, Maxwell Li, Arjun Sapkota, Anish Rai, Ashok Pokhrel, Tim Mewes, Claudia Mewes, Di Xiao, Marc De Graef, and Vincent Sokalski. Magnetic domain wall skyrmions. *Phys. Rev. B*, 99:184412, May 2019.

[147] Tomoki Nagase, Yeong-Gi So, Hayata Yasui, Takafumi Ishida, Hiroyuki K. Yoshida, Yukio Tanaka, Koh Saitoh, Nobuyuki Ikarashi, Yuki Kawaguchi, Makoto Kuwahara, and Masahiro Nagao. Observation of domain wall bimerons in chiral magnets. *Nat. Commun.*, 12(1), 2021.

[148] Kaifeng Yang, Katsumi Nagase, Yoshiro Hirayama, Tetsuya D. Mishima, Michael B. Santos, and Hongwu Liu. Wigner solids of domain wall skyrmions. *Nat. Commun.*, 12(1), 2021.

[149] Xiaokang Li, Liangcai Xu, Huakun Zuo, Alaska Subedi, Zengwei Zhu, and Kamran Behnia. Momentum-space and real-space Berry curvatures in Mn_3Sn. *SciPost Physics*, 5(6):063, 2018.

[150] Xiaokang Li, Clément Collignon, Liangcai Xu, Huakun Zuo, Antonella Cavanna, Ulf Gennser, Dominique Mailly, Benoît Fauqué, Leon Balents, Zengwei Zhu, and Kamran Behnia. Chiral domain walls of Mn3Sn and their memory. *Nat. Commun.*, 10(1):3021, 2019.

[151] Satoru Hayami, Shi-Zeng Lin, and Cristian D. Batista. Bubble and skyrmion crystals in frustrated magnets with easy-axis anisotropy. *Phys. Rev. B*, 93:184413, May 2016.

[152] N A Sinitsyn. Semiclassical theories of the anomalous Hall effect. *Journal of Physics: Condensed Matter*, 20(2):023201, dec 2007.

[153] F. Wolff Fabris, P. Pureur, J. Schaf, V. N. Vieira, and I. A. Campbell. Chiral anomalous Hall effect in reentrant AuFe alloys. *Phys. Rev. B*, 74:214201, Dec 2006.

[154] J. C. Gallagher, K. Y. Meng, J. T. Brangham, H. L. Wang, B. D. Esser, D. W. McComb, and F. Y. Yang. Robust Zero-Field Skyrmion Formation in FeGe Epitaxial Thin Films. *Phys. Rev. Lett.*, 118:027201, Jan 2017.

[155] XZ Yu, Yoshinori Onose, Naoya Kanazawa, Joung Hwan Park, JH Han, Yoshio Matsui, Naoto Nagaosa, and Yoshinori Tokura. Real-space observation of a two-dimensional skyrmion crystal. *Nature*, 465(7300):901–904, 2010.

[156] Tokura Y. Nagaosa N. Topological properties and dynamics of magnetic skyrmions. *Nature nanotechnology*, 8(12):899–911, 2013.

[157] Roderich Moessner and Arthur P. Ramirez. Geometrical frustration. *Physics Today*, 59(2):24–29, 2006.

[158] Micha Nixon, Eitan Ronen, Asher A. Friesem, and Nir Davidson. Observing Geometric Frustration with Thousands of Coupled Lasers. *Phys. Rev. Lett.*, 110:184102, May 2013.

[159] N. Qureshi, B. Ouladdiaf, A. Senyshyn, V. Caignaert, and M. Valldor. Non-collinear magnetic structures in the magnetoelectric Swedenborgite $CaBaFe_4O_7$ derived by powder and single-crystal neutron diffraction. *SciPost Phys. Core*, 5:7, 2022.

[160] T. Asaba, Ying Su, M. Janoschek, J. D. Thompson, S. M. Thomas, E. D. Bauer, Shi-Zeng Lin, and F. Ronning. Large tunable anomalous Hall effect in the kagome antiferromagnet $U_3Ru_4Al_{12}$. *Phys. Rev. B*, 102:035127, Jul 2020.

[161] T. Nagamiya, S. Tomiyoshi, and Y. Yamaguchi. Triangular spin configuration and weak ferromagnetism of Mn_3Sn and Mn_3Ge. *Solid State Communications*, 42(5):385–388, 1982.

[162] Qi Wang, Shanshan Sun, Xiao Zhang, Fei Pang, and Hechang Lei. Anomalous Hall effect in a ferromagnetic Fe_3Sn_2 single crystal with a geometrically frustrated Fe bilayer kagome lattice. *Phys. Rev. B*, 94:075135, Aug 2016.

[163] Y Nii, T Nakajima, A Kikkawa, Y Yamasaki, K Ohishi, J Suzuki, Y Taguchi, T Arima, Y Tokura, and Y. Iwasa. Uniaxial stress control of skyrmion phase. *Nature communications*, 6(1):1–7, 2015.

[164] Giovanni Finocchio, Felix Büttner, Riccardo Tomasello, Mario Carpentieri, and Mathias Kläui. Magnetic skyrmions: from fundamental to applications. *Journal of Physics D: Applied Physics*, 49(42):423001, sep 2016.

[165] Shijiang Luo, Min Song, Xin Li, Yue Zhang, Jeongmin Hong, Xiaofei Yang, Xuecheng Zou, Nuo Xu, and Long You. Reconfigurable Skyrmion Logic Gates. *Nano Lett.*, 18(2):1180–1184, 2018.

[166] Oleg I. Utesov. Thermodynamically stable skyrmion lattice in a tetragonal frustrated antiferromagnet with dipolar interaction. *Phys. Rev. B*, 103:064414, Feb 2021.

[167] J .W. Cable, N. Wakabayashi, and P. Radhakrishna. A neutron study of the magnetic structure of Mn_3Sn. *Solid State Commun.*, 88(2):161–166, 1993.

[168] W. J. Feng, D. Li, W. J. Ren, Y. B. Li, W. F. Li, J. Li, Y. Q. Zhang, and Z. D. Zhang. Glassy ferromagnetism in Ni_3Sn-type $Mn_{3.1}Sn_{0.9}$. *Phys. Rev. B*, 73:205105, May 2006.

[169] Naoki Kiyohara, Takahiro Tomita, and Satoru Nakatsuji. Giant Anomalous Hall Effect in the Chiral Antiferromagnet Mn_3Ge. *Phys. Rev. Applied*, 5:064009, Jun 2016.

[170] Brian C Sales, Bayrammurad Saparov, Michael A McGuire, David J Singh, and David S Parker. Ferromagnetism of fe 3 sn and alloys. *Scientific reports*, 4(1):1–6, 2014.

[171] Olga Yu. Vekilova, Bahar Fayyazi, Konstantin P. Skokov, Oliver Gutfleisch, Cristina Echevarria-Bonet, José Manuel Barandiarán, Alexander Kovacs, Johann Fischbacher, Thomas Schrefl, Olle Eriksson, and Heike C. Herper. Tuning the magnetocrystalline anisotropy of Fe_3Sn by alloying. *Phys. Rev. B*, 99:024421, Jan 2019.

[172] P. C. Canfield and Z. Fisk. Growth of single crystals from metallic fluxes. *Philosophical Magazine B*, 65(6):1117–1123, 1992.

[173] Achintya Low, Susanta Ghosh, and Setti Thirupathaiah. Large Room-Temperature Pure Topological Hall Effect (THE) in Kagome Antiferromagnet Mn_3Sn, and Induced Giant Low-Temperature THE with Fe Doping. arXiv:2112.15409, 2021.

[174] B. L. Altshuler, D. Khmel'nitzkii, A. I. Larkin, and P. A. Lee. Magnetoresistance and Hall effect in a disordered two-dimensional electron gas. *Phys. Rev. B*, 22:5142–5153, Dec 1980.

[175] S. Dhara, R. Roy Chowdhury, and B. Bandyopadhyay. Observation of resistivity minimum at low temperature in $\mathrm{Co}_x\mathrm{Cu}_{1-x}$ ($x \sim 0.17$–0.76) nanostructured granular alloys. *Phys. Rev. B*, 93:214413, Jun 2016.

[176] A. S. Sukhanov, A. Heinemann, L. Kautzsch, J. D. Bocarsly, S. D. Wilson, C. Felser, and D. S. Inosov. Robust metastable skyrmions with tunable size in the chiral magnet $\mathrm{FePtMo_3N}$. *Phys. Rev. B*, 102:140409, Oct 2020.

[177] Jun Kondo. Resistance Minimum in Dilute Magnetic Alloys. *Progress of Theoretical Physics*, 32(1):37–49, 07 1964.

[178] Patrick A. Lee and T. V. Ramakrishnan. Disordered electronic systems. *Rev. Mod. Phys.*, 57:287–337, Apr 1985.

[179] Hai-Zhou Lu and Shun-Qing Shen. Weak localization and weak anti-localization in topological insulators. In Henri-Jean Drouhin, Jean-Eric Wegrowe, and Manijeh Razeghi, editors, *SPIE Proceedings*. SPIE, aug 2014.

[180] Yan Xu, Jincang Zhang, Guixin Cao, Chao Jing, and Shixun Cao. Low-temperature resistivity minimum and weak spin disorder of polycrystalline $\mathrm{LaCaMnO_3}$ in a magnetic field. *Phys. Rev. B*, 73:224410, June 2006.

[181] Marissol R. Felez, Adelino A. Coelho, and Sergio Gama. Magnetic properties of $\mathrm{Mn}_{3-x}\mathrm{Fe}_x\mathrm{Sn}$ compounds with tuneable Curie temperature by Fe content for thermomagnetic motors. *J. Magn. Magn. Mater.*, 444:280–283, dec 2017.

[182] Tapas Samanta, Ahmad Us Saleheen, Daniel L. Lepkowski, Alok Shankar, Igor Dubenko, Abdiel Quetz, Mahmud Khan, Naushad Ali, and Shane Stadler. Asymmetric switchinglike behavior in the magnetoresistance at low fields in bulk metamagnetic Heusler alloys. *Phys. Rev. B*, 90:064412, Aug 2014.

[183] Edmund Clifton Stoner and E. P. Wohlfarth. A mechanism of magnetic hysteresis in heterogeneous alloys. *Philosophical Transactions of the Royal Society of London. Series A, Mathematical and Physical Sciences*, 240(826):599–642, 1948.

[184] J. M. D. Coey. *Magnetism and Magnetic Materials*. Cambridge University Press, 2010.

[185] Bertrand Dupé, Markus Hoffmann, Charles Paillard, and Stefan. Heinze. Tailoring magnetic skyrmions in ultra-thin transition metal films. *Nature communications*, 5(1):1–6, 2014.

[186] Stefan Heinze, Kirsten Von Bergmann, Matthias Menzel, Jens Brede, André Kubetzka, Roland Wiesendanger, Gustav Bihlmayer, and Stefan. Blügel. Spontaneous atomic-scale magnetic skyrmion lattice in two dimensions. *Nature Physics*, 7(9):713–718, 2011.

[187] Q Recour, T Mazet, and B Malaman. Magnetic and magnetocaloric properties of $Mn_{3-x}Fe_xSn_2$ ($0.1 \leq x \leq 0.9$). *J. Phys. Appl. Phys.*, 41(18):185002, aug 2008.

[188] Y. Ishikawa, K. Tajima, D. Bloch, and M. Roth. Helical spin structure in manganese silicide MnSi. *Solid State Commun.*, 19(6):525–528, 1976.

[189] B Lebech, J Bernhard, and T Freltoft. Magnetic structures of cubic FeGe studied by small-angle neutron scattering. *J. Phys. Condens. Matter*, 1(35):6105–6122, 1989.

[190] T. Adams, A. Chacon, M. Wagner, A. Bauer, G. Brandl, B. Pedersen, H. Berger, P. Lemmens, and C. Pfleiderer. Long-Wavelength Helimagnetic Order and Skyrmion Lattice Phase in Cu_2OSeO_3. *Phys. Rev. Lett.*, 108:237204, Jun 2012.

[191] Ryan A. Beck, Lixin Lu, Peter V. Sushko, Xiaodong Xu, and Xiaosong Li. Defect-Induced Magnetic Skyrmion in a Two-Dimensional Chromium Triiodide Monolayer. *JACS Au*, 1(9):1362–1367, 2021.

[192] Kosuke Karube, Licong Peng, Jan Masell, Mamoun Hemmida, Hans-Albrecht Krug von Nidda, István Kézsmárki, Xiuzhen Yu, Yoshinori Tokura, and Yasujiro Taguchi. Doping Control of Magnetic Anisotropy for Stable Antiskyrmion Formation in Schreibersite $(Fe,Ni)_3P$ with S_4 symmetry. *Advanced Materials*, 34(11):2108770, 2022.

[193] I. Raičević, Dragana Popović, C. Panagopoulos, Lara Benfatto, M. B. Silva Neto, E. S. Choi, and T. Sasagawa. Skyrmions in a doped antiferromagnet. *Physical Review Letters*, 106(22), 6 2011.

[194] Radivoje S Popovic. *Hall effect devices*. CRC Press, 2003.

[195] Edward Ramsden. *Hall-effect sensors: theory and application*. Elsevier, 2011.

[196] Kaustuv Manna, Lukas Muechler, Ting-Hui Kao, Rolf Stinshoff, Yang Zhang, Johannes Gooth, Nitesh Kumar, Guido Kreiner, Klaus Koepernik, Roberto Car, Jürgen Kübler, Gerhard H. Fecher, Chandra Shekhar, Yan Sun, and Claudia Felser. From Colossal to Zero: Controlling the Anomalous Hall Effect in Magnetic Heusler Compounds via Berry Curvature Design. *Phys. Rev. X*, 8:041045, Dec 2018.

[197] S. K. Lyo and T. Holstein. Side-Jump Mechanism for Ferromagnetic Hall Effect. *Phys. Rev. Lett.*, 29:423–425, Aug 1972.

[198] Bill Sutherland. Localization of electronic wave functions due to local topology. *Phys. Rev. B*, 34:5208–5211, Oct 1986.

[199] Elliott H. Lieb. Two theorems on the Hubbard model. *Phys. Rev. Lett.*, 62:1201–1204, Mar 1989.

[200] Daniel Leykam, Alexei Andreanov, and Sergej Flach. Artificial flat band systems: from lattice models to experiments. *Advances in Physics: X*, 3(1):1473052, 1 2018.

[201] Congjun Wu, Doron Bergman, Leon Balents, and S. Das Sarma. Flat Bands and Wigner Crystallization in the Honeycomb Optical Lattice. *Phys. Rev. Lett.*, 99:070401, Aug 2007.

[202] Huaqing Huang, Zhirong Liu, Hongbin Zhang, Wenhui Duan, and David Vanderbilt. Emergence of a Chern-insulating state from a semi-Dirac dispersion. *Phys. Rev. B*, 92:161115, Oct 2015.

[203] Gang Xu, Hongming Weng, Zhijun Wang, Xi Dai, and Zhong Fang. Chern Semimetal and the Quantized Anomalous Hall Effect in $HgCr_2Se_4$. *Phys. Rev. Lett.*, 107:186806, Oct 2011.

[204] Karl Landsteiner. Anomalous transport of Weyl fermions in Weyl semimetals. *Phys. Rev. B*, 89:075124, Feb 2014.

[205] Kentaro Nomura and A. H. MacDonald. Quantum Transport of Massless Dirac Fermions. *Phys. Rev. Lett.*, 98:076602, Feb 2007.

[206] Linda Ye, Mingu Kang, Junwei Liu, Felix Von Cube, Christina R Wicker, Takehito Suzuki, Chris Jozwiak, Aaron Bostwick, Eli Rotenberg, David C Bell, et al. Massive dirac fermions in a ferromagnetic kagome metal. *Nature*, 555(7698):638–642, 3 2018.

[207] Taishi Chen, Susumu Minami, Akito Sakai, Yangming Wang, Zili Feng, Takuya Nomoto, Motoaki Hirayama, Rieko Ishii, Takashi Koretsune, Ryotaro Arita, and Satoru Nakatsuji. Large anomalous Nernst effect and nodal plane in an iron-based kagome ferromagnet. *Sci. Adv.*, 8(2):eabk1480, 2022.

[208] Juan Rodríguez-Carvajal. FullProf. *CEA/Saclay, France*, 1045:132–146, 2001.

[209] R. Prozorov and V. G. Kogan. Effective Demagnetizing Factors of Diamagnetic Samples of Various Shapes. *Phys. Rev. Appl.*, 10:014030, Jul 2018.

[210] Sam Mugiraneza and Alannah M Hallas. Tutorial: a beginner's guide to interpreting magnetic susceptibility data with the Curie-Weiss law. *Communications Physics*, 5(1):95, 2022.

[211] Kamran Behnia. On the Origin and the Amplitude of T-Square Resistivity in Fermi Liquids. *Ann. Phys.*, 534(5):2100588, 2022.

[212] G. Varelogiannis and E. N. Economou. Small-q electron-phonon scattering and linear dc resistivity in High-T_c oxides. *Europhys. Lett.*, 42(3):313, may 1998.

[213] Changgan Zeng, Yugui Yao, Qian Niu, and Hanno H. Weitering. Linear Magnetization Dependence of the Intrinsic Anomalous Hall Effect. *Phys. Rev. Lett.*, 96:037204, Jan 2006.

[214] Zhijun Wang, M. G. Vergniory, S. Kushwaha, Max Hirschberger, E. V. Chulkov, A. Ernst, N. P. Ong, Robert J. Cava, and B. Andrei Bernevig. Time-Reversal-Breaking Weyl Fermions in Magnetic Heusler Alloys. *Phys. Rev. Lett.*, 117:236401, Nov 2016.

[215] Jerome M. Lavine. Extraordinary Hall-Effect Measurements on Ni, Some Ni Alloys, and Ferrites. *Phys. Rev.*, 123:1273–1277, Aug 1961.

[216] Atsuo Shitade and Naoto Nagaosa. Anomalous Hall Effect in Ferromagnetic Metals: Role of Phonons at Finite Temperature. *J. Phys. Soc. Jpn.*, 81(8):083704, aug 2012.

[217] Yuan Tian, Li Ye, and Xiaofeng Jin. Proper Scaling of the Anomalous Hall Effect. *Phys. Rev. Lett.*, 103:087206, Aug 2009.

[218] Dazhi Hou, Gang Su, Yuan Tian, Xiaofeng Jin, Shengyuan A. Yang, and Qian Niu. Multivariable Scaling for the Anomalous Hall Effect. *Phys. Rev. Lett.*, 114:217203, May 2015.

[219] Chen Shen, Ilias Samathrakis, Kun Hu, Harish K Singh, Nuno Fortunato, Huashan Liu, Oliver Gutfleisch, and Hongbin Zhang. Thermodynamical and topological properties of metastable Fe_3Sn. *npj Comput. Mater.*, 8(1):248, 2022.

[220] Shigeki Onoda, Naoyuki Sugimoto, and Naoto Nagaosa. Intrinsic Versus Extrinsic Anomalous Hall Effect in Ferromagnets. *Phys. Rev. Lett.*, 97:126602, Sep 2006.

[221] Lilian Prodan, Donald M. Evans, Sinéad M. Griffin, Andreas Östlin, Markus Altthaler, Erik Lysne, Irina G. Filippova, Serghei Shova, Liviu Chioncel, Vladimir Tsurkan, and István Kézsmárki. Large ordered moment with strong easy-plane anisotropy and vortex-domain pattern in the kagome ferromagnet Fe_3Sn, 2023.

[222] M. S. S. Brooks, Lars Nordström, and Börje Johansson. Rare-earth transition-metal intermetallics. *Physica B*, 172(1-2):95–100, 6 1991.

[223] Cui Zu Chang, Jinsong Zhang, Xiao Feng, Jie Shen, Zuocheng Zhang, Minghua Guo, Kang Li, Yunbo Ou, Pianpian Wei, Li Li Wang, Zhong Qing Ji, Yang Feng, Shuai-Hua Ji, Xi Chen, Jin-Feng Jia, Xi Dai, Zhong Fang, Shou Cheng Zhang, Ke He, Yayu Wang, Li Lu, Xu Cun, and Qi Kun Xue. Experimental observation of the quantum anomalous Hall effect in a magnetic topological insulator. *Science*, 340(6129):167–170, 4 2013.

[224] B. Keimer and J. E. Moore. The physics of quantum materials. *Nature Physics*, 13(11):1045–1055, oct 2017.

[225] Subir Sachdev. Topological order, emergent gauge fields, and Fermi surface reconstruction. *Reports on Progress in Physics*, 82(1):014001, 11 2018.

[226] Yoshinori Tokura, Kenji Yasuda, and Atsushi Tsukazaki. Magnetic topological insulators. *Nature Reviews Physics*, 1(2):126–143, jan 2019.

[227] Paul C. Canfield. New materials physics. *Reports on Progress in Physics*, 83(1):016501, 11 2019.

[228] Atsufumi Hirohata, Keisuke Yamada, Yoshinobu Nakatani, Ioan-Lucian Prejbeanu, Bernard Diény, Philipp Pirro, and Burkard Hillebrands. Review on spintronics: Principles and device applications. *Journal of Magnetism and Magnetic Materials*, 509:166711, 9 2020.

[229] Alexei Kitaev. Anyons in an exactly solved model and beyond. *Annals of Physics*, 321(1):2–111, 1 2006.

[230] Joel S. Helton, K. Matan, Matthew P. Shores, Emily A. Nytko, Bart M. Bartlett, Yasuo Yoshida, Y. Takano, A. V. Suslov, Yiming Qiu, Jaiho Chung, Daniel G. Nocera, and Y. S. Lee. Spin Dynamics of the Spin-$1/2$ Kagome Lattice Antiferromagnet $ZnCu_3(OH)_6Cl_2$ Spin Dynamics of the Spin-$1/2$ Kagome Lattice Antiferromagnet $ZnCu_3(OH)_6Cl_2$. *Phys. Rev. Lett.*, 98(10), 3 2007.

[231] Tianheng Han, Joel S. Helton, Shaoyan Chu, Daniel G. Nocera, J. A. Rodriguez-Rivera, C. Broholm, and Young Soo Lee. Fractionalized excitations in the spin-liquid state of a kagome-lattice antiferromagnet. *Nature*, 492(7429):406–410, 12 2012.

[232] Y. Kasahara, Takeshi Ohnishi, Yuta Mizukami, O. Tanaka, Sixiao Ma, Kaori Sugii, Nobuyuki Kurita, Hidekazu Tanaka, Joji Nasu, Yukitoshi Motome, T. Shibauchi, and Yuji Matsuda. Majorana quantization and half-integer thermal quantum Hall effect in a Kitaev spin liquid. *Nature*, 559(7713):227–231, 7 2018.

[233] D. F. Liu, Aiji Liang, E. K. Liu, Qiunan Xu, Y. W. Li, C. Chen, Ding Pei, Wujun Shi, S.-k. Mo, Pavel Dudin, T. K. Kim, Cephise Cacho, Gang Li, Yan Sun, Lexian Yang, Z. K. Liu, Stuart S. P. Parkin, Claudia Felser, and Y. L. Chen. Magnetic Weyl semimetal phase in a Kagomé crystal. *Science*, 365(6459):1282–1285, 9 2019.

[234] Gang Xu, Biao Lian, and Shou-Cheng Zhang. Intrinsic Quantum Anomalous Hall Effect in the Kagome Lattice $Cs_2LiMn_3F_{12}$. *Phys. Rev. Lett.*, 115:186802, Oct 2015.

[235] Dola Chakrabartty, Sk Jamaluddin, Subhendu Kumar Manna, and Ajaya K. Nayak. Tunable room temperature magnetic skyrmions in centrosymmetric kagome magnet Mn_4Ga_2Sn. *Communications physics*, 5(1), 7 2022.

[236] Lingling Gao, Shiwei Shen, Qi Wang, Wujun Shi, Yi Zhao, Changhua Li, Weizheng Cao, Cuiying Pei, Jun-Yi Ge, Gang Li, Jun Li, Yulin Chen, Shichao Yan, and Yue Qi. Anomalous Hall effect in ferrimagnetic metal RMn_6Sn_6 (R = Tb, Dy, Ho) with clean Mn kagome lattice. *Applied Physics Letters*, 119(9), 8 2021.

[237] Firoza Kabir, Randall Filippone, Gyanendra Dhakal, Y. Lee, Narayan Poudel, Jacob Casey, Anup Pradhan Sakhya, Sabin Regmi, Robert Smith, Pietro Manfrinetti, Liqin Ke, Krzysztof Gofryk, Madhab Neupane, and Arjun K. Pathak. Unusual magnetic and transport properties in $HoMn_6Sn_6$ kagome magnet. *Phys. Rev. Mater.*, 6:064404, Jun 2022.

[238] Daniel Campbell, John Collini, Jagoda Sławińska, Carmine Autieri, L. Wang, K. Wang, Brandon Wilfong, Yun Suk Eo, Paul M. Neves, David Graf, Efrain E. Rodriguez, Nicholas P. Butch, Marco Buongiorno Nardelli, and Johnpierre Paglione. Topologically driven linear magnetoresistance in helimagnetic FeP. *npj quantum materials*, 6(1), 4 2021.

[239] G. Venturini, Richard Welter, and B. Malaman. Crystallographic data and magnetic properties of RT_6Ge_6 compounds (R Sc, Y, Nd, Sm, Gd Lu; T Mn, Fe). *Journal of Alloys and Compounds*, 185(1):99–107, 7 1992.

[240] Y. Lee, R. Skomski, X. Wang, P. P. Orth, Y. Ren, Byungkyun Kang, A. K. Pathak, A. Kutepov, B. N. Harmon, R. J. McQueeney, I. I. Mazin, and Liqin Ke. Interplay between magnetism and band topology in the kagome magnets $R\mathrm{Mn}_6\mathrm{Sn}_6$. *Phys. Rev. B*, 108:045132, Jul 2023.

[241] P Schobinger-Papamanteilos. A neutron diffraction study of the magnetic ordering of $\mathrm{HoMn}_6\mathrm{Ge}_6$. *Journal of Magnetism and Magnetic Materials*, 139(1-2):119–130, jan 1995.

[242] John P. Perdew, Kieron Burke, and Matthias Ernzerhof. Generalized Gradient Approximation Made Simple. *Phys. Rev. Lett.*, 77:3865–3868, Oct 1996.

[243] Paolo Giannozzi, Stefano Baroni, Nicola Bonini, Matteo Calandra, Roberto Car, Carlo Cavazzoni, Davide Ceresoli, Guido L Chiarotti, Matteo Cococcioni, Ismaila Dabo, et al. QUANTUM ESPRESSO: a modular and open-source software project for quantum simulations of materials. *J. Phys.: Condens. Matter*, 21(39):395502, 2009.

[244] G. Venturini, A. Vernière, and B. Malaman. Multi spin-reorientation process in $\mathrm{HfFe}_6\mathrm{Ge}_6$-type $\mathrm{HoMn}_6\mathrm{Ge}_{6x}\mathrm{Ga}_x$ compounds (x=0.2, 0.4, 1.0). *Journal of Alloys and Compounds*, 320(1):46–57, 5 2001.

[245] Arthur Mar, Christophe Lefèvre, and G. Venturini. Anisotropic transport properties measured in $\mathrm{HoMn}_6\mathrm{Ge}_6$ single crystals. *Journal of Magnetism and Magnetic Materials*, 269(3):380–384, 3 2004.

[246] A. A. Abrikosov. Quantum magnetoresistance. *Phys. Rev. B*, 58:2788–2794, Aug 1998.

[247] A. A. Abrikosov. Quantum linear magnetoresistance. *EPL*, 49(6):789–793, 3 2000.

[248] Jing-Ping Xu, Zhang Duan-Ming, Zongwei Deng, Yang Fu, Zhihua Li, and Yuan Pan. Quasi-Random resistor network model for linear magnetoresistance of Metal–Semiconductor composite. *Chinese Physics Letters*, 25(11):4124–4127, 10 2008.

[249] Navneeth Ramakrishnan, Ying Tong Lai, Silvia Lara, Meera M. Parish, and Shaffique Adam. Equivalence of effective medium and random resistor network models for disorder-induced unsaturating linear magnetoresistance. *Phys. Rev. B*, 96:224203, Dec 2017.

[250] Ruidong Xu, Anke Husmann, T. F. Rosenbaum, Marie-Louise Saboungi, J. E. Enderby, and P. B. Littlewood. Large magnetoresistance in non-magnetic silver chalcogenides. *Nature*, 390(6655):57–60, 11 1997.

[251] Meera M. Parish and P. B. Littlewood. Non-saturating magnetoresistance in heavily disordered semiconductors. *Nature*, 426(6963):162–165, 11 2003.

[252] Gyanendra Dhakal, Fairoja Cheenicode Kabeer, Arjun K. Pathak, Firoza Kabir, Narayan Poudel, Randall Filippone, Jacob Casey, Anup Pradhan Sakhya, Sabin Regmi, Christopher Sims, Klauss Dimitri, Pietro Manfrinetti, Krzysztof Gofryk, Peter M. Oppeneer, and Madhab Neupane. Anisotropically large anomalous and topological Hall effect in a kagome magnet. *Phys. Rev. B*, 104:L161115, Oct 2021.

[253] Yongkang Luo, F. Ronning, N. Wakeham, Xin Lu, Tuson Park, Zhu-An Xu, and J. D. Thompson. Pressure-tuned quantum criticality in the antiferromagnetic Kondo semimetal CeNi$_{2\delta}$As$_2$. *Proceedings of the National Academy of Sciences of the United States of America*, 112(44):13520–13524, 10 2015.

[254] Takehito Suzuki, Robin Chisnell, Aravind Devarakonda, Y.-t. Liu, Feng Wang, Di Xiao, J. W. Lynn, and Joseph Checkelsky. Large anomalous Hall effect in a half-Heusler antiferromagnet. *Nature Physics*, 12(12):1119–1123, 7 2016.

[255] Jingjing Niu, Baoming Yan, Qingqing Ji, Zhongfan Liu, Mingqiang Li, Peng Gao, Yanfeng Zhang, Dapeng Yu, and Xiaosong Wu. Anomalous Hall effect and magnetic orderings in nanothick V$_5$S$_8$. *Phys. Rev. B*, 96:075402, Aug 2017.

[256] J. M. Luttinger. Fermi Surface and Some Simple Equilibrium Properties of a System of Interacting Fermions. *Phys. Rev.*, 119:1153–1163, Aug 1960.

[257] Aurélie Collaudin, Benoît Fauqué, Yuki Fuseya, Woun Kang, and Kamran Behnia. Angle Dependence of the Orbital Magnetoresistance in Bismuth. *Phys. Rev. X*, 5:021022, Jun 2015.

[258] Jialu Wang, Haiyang Yang, Linchao Ding, Wei You, Chuanying Xi, Jie Cheng, Zhixiang Shi, Chao Cao, Yongkang Luo, Zengwei Zhu, Jianhui Dai, Mingliang Tian, and Yuke Li. Angle-dependent magnetoresistance and its implications for Lifshitz transition in W$_2$As$_3$. *npj quantum materials*, 4(1), 11 2019.

[259] ShengNan Zhang, QuanSheng Wu, Yi Liu, and Oleg V. Yazyev. Magnetoresistance from Fermi surface topology. *Phys. Rev. B*, 99:035142, Jan 2019.